UNIVERSITÁ DEGLI STUDI DI PARMA
Dipartimento di Fisica e Scienze della Terra

Dynamical bar-mode instability in magnetized relativistic stars

Luca Franci

Supervisor:
Dr. Roberto De Pietri

Coordinator:
Prof. Pier Paolo Lottici

Tesi sottomessa per il titolo di
DOTTORATO DI RICERCA IN FISICA

Thesis submitted for the award of the degree of
PHD IN PHYSICS

XXVI ciclo

Contents

Introduction

Main-sequence stars with masses greater than about $8\,M_\odot$ follow two evolutionary paths; either they form a degenerate core of O/Ne/Mg, or a degenerate Fe core, which, after undergoing a Type II supernova core collapse, forms a proto-neutron star [1, 2]. Neutron stars (NSs) are also expected to form through the accretion-induced collapse of a white dwarf [3, 4]. At birth, NSs are rapidly and differentially rotating, which makes them subject to various types of instabilities. Among these, the dynamical bar-mode instability and the shear-instability are particularly interesting because of their potential role as sources of gravitational waves (GWs).

Indeed, a newly born NS may develop a dynamical bar-mode instability when the rotation parameter $\beta := T/|W|$, with T the rotational kinetic energy and W the gravitational binding energy, exceeds a critical value β_c (see, for instance, [5, 6] for some reviews). Under these conditions, the rapidly rotating NS can become severely deformed, leading to a strong emission of GWs in the kHz range. Analytic investigations of the conditions under which these dynamical instabilities develop in self-gravitating rotating stars can be found in [7, 8], but these are inevitably restricted to Newtonian gravity or to simple shell models. To improve our understanding of these instabilities also in the nonlinear regimes, and to be able to extract useful physical information from the potential GW emission, it is clear that a general-relativistic numerical modeling is necessary. This has been the focus of a number of recent works, e.g., [9, 10, 11, 12], which have provided important clues about the threshold for the instability and its survival under realistic conditions. As an example, for a polytropic relativistic star with polytropic index $\Gamma = 2$, the calculations reported in [10] revealed that the critical value is $\beta_c \sim 0.254$, and that a simple dependence on the stellar compactness can be used to track this threshold from the Newtonian limit over to the fully relativistic one [11]. Furthermore, numerical simulations have also revealed that the instability is in general short-lived and that the bar-deformation is suppressed over a timescale of a few revolutions (this was first

pointed out in Ref. [10] and later confirmed in Ref. [13], where it was interpreted as due to a Faraday resonance).

One aspect of the bar-mode instability that so far has not received sufficient attention is about the occurrence of the instability in magnetized stars. This is not an academic question since NSs at birth are expected to be quite generically magnetized, with magnetic fields that have strengths up to $\simeq 10^{12}$ G in ordinary NSs and reaching strengths in excess of 10^{15} G in magnetars, if instabilities or dynamos have taken place in the proto-neutron star phase [14, 15].

Such magnetic fields can affect both the structure and the evolution of NSs [16, 17, 18, 19], and it is natural to expect that they will influence also the development of the instability when compared to the purely hydrodynamical case. A first dynamical study in this direction has been carried out recently in Ref. [20], where the development of the dynamical bar-mode instability has been studied for differentially rotating magnetized stars in Newtonian gravity and in the ideal-magnetohydrodynamics (MHD) limit (i.e., with a plasma having infinite conductivity). Not surprisingly, this study found that magnetic fields do have an effect on the development of the instability, but this is the case only for very strong magnetic fields. We here consider the same problem, but extend the analysis to a fully general-relativistic framework, assessing the impact that the results have on high-energy astrophysics and GW astronomy.

Our investigation of the dynamics of highly-magnetized and rapidly rotating NSs is also part of a wider study of this type of objects to explain the phenomenology associated with short gamma-ray bursts. These catastrophic phenomena, in fact, are normally thought to be related to the merger of a binary system of NSs [21, 22, 23, 24], which could then lead to the formation of a long-lived hypermassive NS (HMNS) [25, 26, 27, 28]. If highly magnetized, the HMNS could then also lead to an intense electromagnetic emission [29, 30]. This scenario has recently been considered in Refs. [31, 32], where numerical simulations of an axisymmetric differentially rotating HMNS were carried out. The HMNS had initially a purely poloidal magnetic field, which eventually led to a magnetically driven outflow along the rotation axis.

A similar setup has also been considered in a number of works, either in two-dimensional (2D) [33] or in three-dimensional (3D) simulations [34], with the goal of determining whether or not the conditions typical of a HMNS can lead to the development of the magnetorotational (MRI) instability [35, 36]. Although this type of simulations in 3D still stretches the computational resources presently available, the very high resolutions employed in Ref. [34], and the careful analysis of the results, provided the first convincing evidence that the MRI can develop from 3D configurations. This has of course important consequences on much of

the phenomenology associated with HMNSs, as it shows that very strong magnetic fields, up to equipartition, will be produced in the HMNS if this survives long enough for the MRI to develop.

In this Thesis, we extend the previous work on the dynamical bar-mode instability [10, 11, 37] also to the case of magnetized stars. Our main goal is to accurately analyze when and how magnetic fields can affect, or even suppress, the development of the dynamical bar-mode instability in differentially rotating relativistic stars. We have already studied this topic in [38, 39], but here we provide a more accurate and detailed description of the dynamics of both bar-stable and bar-unstable models. The initial stellar models we evolve here correspond to stationary equilibrium configurations of axisymmetric and rapidly rotating relativistic stars, described by a polytropic EOS with adiabatic index $\Gamma = 2$ and members of a sequence with a constant rest-mass of $M \simeq 1.5\ M_{\odot}$ and a constant amount of differential rotation.

Our main result is that very strong initial magnetic fields, i.e., $\gtrsim 10^{16}$ G, are able to completely inhibit the emergence of a bar deformation and the onset of a dynamical bar-mode instability, even in those models which have been proved to be bar-mode unstable in the unmagnetized case. On the other hand, we find that initial poloidal magnetic fields with strengths $\lesssim 10^{15}$ G have a negligible effect on the development of the dynamical bar-mode instability, whose dynamics is the same as in the purely hydrodynamical case. The precise threshold marking the stability region depends not only on the strength of the magnetic field, but also on the amount of rotation. We trace this threshold by performing many simulations of a number of sequences of many different models having the same value of the instability parameter β but different magnetizations.

All the simulations reported here have been performed in the ideal-MHD limit, so the magnetic field lines are "frozen" in the fluid and follow its dynamics (see [40] for a recent extension of the code to resistive regime). As a consequence, differential rotation drives the initial purely poloidal magnetic field into rotation, winding it up and generating a toroidal component. At early times, the toroidal magnetic field grows linearly with time, tapping the NS's rotational energy, and suddenly overcomes the original poloidal one becoming the dominant component. At later times, this growth starts deviating from the linear behavior and the magnetic tension produced by the very large magnetic-field winding alters the angular velocity profile of the star. Moreover, we observe a rapid and exponential growth in the toroidal component of the magnetic energy occurring during the matter-unstable phase of the evolution of bar-unstable models, which was already observed in our previous studies [38, 39] and resembles the one

described in Ref. [34]. We have then extended our previous work, in order to investigate the possible development of the MRI in bar-unstable models by performing a number of additional simulations with a finer resolution than the ones reported in [38, 39], in order to look for the features one would expect in the case of an MRI acting on the evolved stellar models. Actually, we will be able to recognize some of the typical features of this kind of instability in many of our simulations, mainly in the ones of bar-unstable models, and to provide a possible explanation for these observations. Nevertheless, the resolution of these more accurate simulations is still much coarser than in Ref. [34], and then a deeper and more extended analysis of this topic has not been feasible by the time of the present Thesis, mainly due to computational limitations. Hence we will not be able to give as firm evidences about the development of the MRI as the ones provided in Ref. [34].

An important consequence of our results is that because the instability is suppressed in strongly magnetized NSs, these can no longer be considered as potential sources of GWs, at least via the dynamical bar-mode instability. Besides, if later confirmed, our observations on an exponential growth of the magnetic field during the matter-unstable phase of the evolution would provide the first evidence of the deveolpment of an non-axisymmetric MRI in 3D global simulations of bar-model unstable relativistic stars.

The plan of this Thesis is as follows. In Chap. 1 a review of the main ingredients necessary for the present work is presented: a general introduction to Neutron Stars (NSs), i.e., their main properties, formation and internal structure and a detailed description of the dynamical bar-mode instability which can develop in NSs, both in the relativistic unmagnetized case and in the Newtonian magnetized case. Chap. 2 introduces a brief description of the 3+1 formalism of Numerical Relativity and the full set of equations we need to solve. The code and numerical methods we used are briefly described in Chap. 3, together with the settings we chose, the main properties of the stellar models adopted as initial data and the methodology we employed in our accurate analysis. In Chap. 4 we describe the effects of magnetic fields on the dynamics of bar-mode stable models, while in Chap. 5 such analysis is extended to the case of models which are bar-mode unstable at zero magnetization. Chap. 6 deals in detail with the evolution of the magnetic field in both stable and unstable models. The main results of our work are summarized in the Conclusions. Lastly, in the Appendix we discuss the influence of symmetries on the development of the instability and the convergence of our results, and we report an extensive view of the dynamics of many of the magnetized models we evolved.

Unless stated differently, we adopt geometrized units in which $c = 1$, $G = 1$, $M_\odot = 1$.

Publication list

The main results presented in the present thesis have been published in the following journal articles:

- L. Franci, R. De Pietri, K. Dionysopoulou and L. Rezzolla
  Bar-mode instability suppression in magnetized relativistic stars
  J. Phys.: Conf. Ser. 470, 012008 (2013)
  arXiV [gr-qc]: http://arxiv.org/abs/1309.6549

- L. Franci, R. De Pietri, K. Dionysopoulou and L. Rezzolla
  Dynamical bar-mode instability in rotating and magnetized relativistic stars
  Phys. Rev. D 88, 104028 (2013)
  arXiV [gr-qc]: http://arxiv.org/abs/1308.3989

Chapter 1

Neutron stars and dynamical instabilities

1.1 Neutron stars

Neutron stars (NSs) are extremely compact stars with a typical mass $M \sim 1.4\ M_\odot$ and a typical radius $R \sim 10$ km, resulting in a compactness $M/R \sim 100$ times higher than the Sun's. These properties makes them the most compact objects endowed with a structure in our Universe, such that they cannot be properly described without resorting to General Relativity. Indeed, these are not the only features that make them among the most "extreme" objects in nature. They exhibit very high densities (a typical value is of the order of the nuclear density $\rho_0 \sim 2.8 \cdot 10^{14}$ g/cm^3), very fast rotation (the fastest known spin frequency for a NSs is ~ 716 Hz, corresponding to approximately 24% of the speed of light at its equator) [41], ultra-strong magnetic fields (magnetic fields range from 10^{13} G for ordinary NSs and up to 10^{16} G in the interior of magnetars). Besides, NSs are quite peculiar since all the four fundamental forces play a crucial role in determining their structure and dynamics and therefore they arouse interest in almost all fields of modern physics, representing natural laboratories to test fundamental physics and strong-field gravity under the above-mentioned extreme conditions, not feasible on Earth. Two of the most intriguing puzzles that one day could be solved thanks to NSs are the behavior of matter at supranuclear densities and the existence of gravitational waves, predicted and yet undetected spacetime perturbations (up to now, we only have indirect evidences, like the one obtained by the Hulse and Taylor from the cumulative shift of periastron time for the binary pulsar PSR 1913+16).

1.1.1 Main observational properties

Two important properties of NSs that can be inferred from observations are their mass and radius. Recent observations have uncovered both massive and low-mass NSs and have also set constraints on NS radii. The largest mass measurements are powerfully influencing the high-density equation of state because of the existence of the NS maximum mass. The smallest mass measurements, and the distributions of masses, have implications for the progenitors and formation mechanisms of NSs. The ensemble of mass and radius observations can realistically restrict the properties of dense matter.

Accurate measurements for NSs masses come from pulsar timing. To date, approximately 33 relatively precise masses have become available. In these systems, five Keplerian parameters can be precisely measured [42], which are the binary period, the projection of the pulsar's semimajor axis on the line of sight, the eccentricity, and the time and longitude of periastron. From these observables we can compute a mass function, which is a relation between the pulsar's mass and the mass of its companion. Anyway, this is not sufficient to infer the mass, unless the mass function of the companion is also measurable, which happens in the rare case when the companion itself is a detectable pulsar or a star with an observable spectrum, as in an X-ray binary. Fortunately, binary pulsars are compact systems, and general relativistic effects can often be observed: in many cases, the detection of relativistic effects such as the Shapiro delat, the advance of periastron or orbit shrinkage due to grativational wave emission permits a constraint on the inclination angle and a measure of the two masses. Most NSs have masses close to 1.3 - 1.4 $M_{\odot}$, but lower and higher masses exist. Actually, there is now ample observational support from pulsars for NSs with masses significantly greater than 1.5 $M_{\odot}$. We can claim that, presently, the mass range 1 - 2 $M_{\odot}$ is compatible with data, even if some recent observations suggest the possibility of larger masses.

In contrast to mass determinations, there are no high-accuracy radius measurements. Moreover, there are no radius measurements for any NSs with a precise mass determination. Many astrophysical observations that could lead to the extraction of NS radii, or combined mass and radius constraints, have been proposed, which include thermal X-ray and optical fluxes from isolated and quiescent NSs [43], quasi-periodic oscillations from accreting NSs, moments of inertia measurements from spin-orbit coupling. Among them, thermal emission and X-ray bursts from NS surfaces have dominated recent attempts to infer NS radii. Present observations suggest NS radii in the range 9 - 16 km. Mass and radius measurements are of fundamental

importance, since several M-R probability distributions allow to put constraints on the overall M-R relation and then on the Equation of State (EOS) of matter at supranuclear densities.

Two other fundamental quantities for an isolated NS are the spin period P and its derivative $\dot{P}$. The observed spin periods range between 1.56 ms, for the fastest spinning NS, and $\sim$ 1 - 10 s, in the case of Soft Gamma Repeaters (SGRs) and Anomalous X-ray Pulsars (AXPs), while the spin derivatives vary in the wide range 10^{-21} - 10^{-9} (adimesional). Their simultaneous knowledge is important for estimating the age (the so-called spindown age $\tau_{SD} = P/2\dot{P}$) and the surface magnetic field strength, which is an essential NS property for the purposes of this Thesis, through the formula

$$B = \left(\frac{3c^3 I}{8\pi^2 R^6}\right)^{1/2} (P\dot{P})^{1/2} \tag{1.1}$$

This is obtained from the assumption that the external field is dipolar and the observed spin-down is entirely due to magnetic braking.

Typical dipole magnetic field strenghts for ordinary pulsars are in the range 10^{11} - 10^{13} G, even if some millisecond pulsars have values down to 10^8 G; on the other hand, magnetars (SGRs and AXPs) have dipole magnetic fields of the order of 10^{14} - 10^{15} G, even higher in their interior. It is estimated that about one in ten supernova explosions results in a magnetar rather than a more standard NS or pulsar and so they are actually quite common objects. Since their first discover in 1979, 21 of them are known, with five more candidates awaiting confirmation. They arouse wide and vivid interest in the Astrophysical community, since they show quite a varied phenomenology, e.g., they also have implications for Gamma-Ray Bursts (GRBs). Even though we are not entering into the details of the formation and structure of such strong magnetic fields, this rough estimate of their typical strength is very important, since the main topic of the present Thesis is the dynamics of highly magnetized neutron stars, and thus we find a reasonable justification for the values we choose for the magnetic field in the models we evolved, which are actually in the range 10^{14} - 10^{16} G.

1.1.2 Formation of compact stars

Stars spend most of their life in a quasi-equilibrium state in which self-gravity is balanced by the radiation pressure due to thermonuclear reactions fusing hydrogen into helium in the stellar core ("main sequence" phase). However, after a few billion years, all available hydrogen in the core is over and the central source of energy supporting equilibrium runs out: the star begins

to contract and warm until hydrogren burning in a shell around the core is ignited. The higher temperatures lead to increasing reaction rates, the star's luminosity increases as well and the outer layers greatly expand, making the star leave the main sequence and begin its "red giant" phase. The following evolutionary path depends on the mass of the star. If it is about 0.2 to $0.5\ M_\odot$, the star is massive enough to become a red giant but not enough to initiate the fusion of helium. Conversely, the core of stars with $M \gtrsim 0.5\ M_\odot$ gets hot enough to begin fusing helium to carbon via the triple-alpha process. Stars with masses up to $\sim 8\ M_\odot$ stop their internal burning before heavier elements are produced: they lose most of their mass by stellar winds forming a "planetary nebula", while their dense core becomes a "white dwarf", supported by the electron degeneracy pressure. Stars with $M \gtrsim 8\ M_\odot$ can go further with hermonuclear reactions fusing carbon to oxygen, neon and magnesium, while in slightly more massive stars ($M \lesssim 10\ M_\odot$) the carbon-burning process keeps going in a shell around the core after the carbon in the core itself is over, so the mass of the core keeps increasing. At some point, the inverse β-decay becomes energetically favorable and extremely efficient in merging together protons and electrons into neutrons, thuse reducing the number of electrons and their degeneracy pression. The inner core collapses, leaving the surrounding material suspended above it, and in supersonic free-fall. The contraction of the core suddenly stops when the density of the nuclear matter is reached and the short-range nuclear force becomes repulsive. The infalling material finally strikes strikes the incompressible core and rebounds, generating a shockwave that progresses outward through the unfused material of the outer shell and a following supernova explosion. The ejected mass will form the supernova remnant, while the superdense core is now a proto-nuetron star (PNS). Stars with $M \gtrsim 10\ M_\odot$ evolve through all phases of thermonuclear burning in the core up to iron: nuclear fusion of elements heavier than iron requires energy intead of releasing it, so when all the silicon is over nuclear burning stops. Since during silicon burning the core has reached extremely high temperatures and densities, the photodisintegration of iron nuclei by very energetic photons reverses the process of fusion and the inverse β-decay reduces the neutron degeneracy pression, thus leading to a sudden collapse. Again, the collapse and bounce of the infalling material will lead to a supernova explosion and to th formation of a PNS. If the progenitor's mass is extremely high ($M \gtrsim 20\ M_\odot$) the accretion of the infalling material onto the PNS will increase its mass above the Tolman-Oppenheimer-Volkoff limit, which is the stability treshold for NSs, and the star will collapse into a black hole.

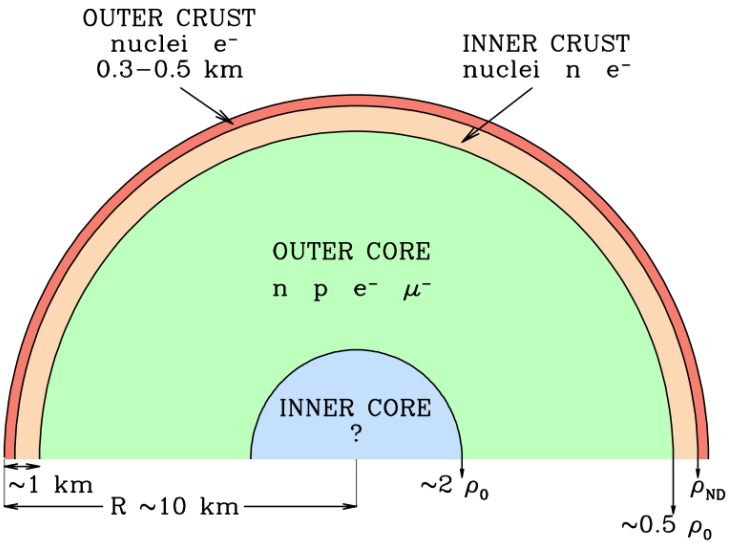

Figure 1.1: Schematic structure of a NS. Here $\rho_{ND} \simeq 4 \times 10^{11}$ g cm^{-3} is the neutron drip density, while $\rho_0 = 2.8 \times 10^{14}$ g cm^{-3} is the saturation nuclear matter density.

1.1.3 Internal structure

According to current theories, a NS can be subdivided into four main layers with density increasing inwards: the outer crust, the inner crust, the outer core and the inner core. The general NS structure is shown schematically in Fig. 1.1. The outer crust extends for some hundred meters, from the atmosphere bottom with density $\rho \sim 10^7$ g cm^{-3} to the layer corresponding to the neutron drip density $\rho = \rho_{ND} \simeq 4 \times 10^{11}$ g cm^{-3}. Its matter consists of ions and electrons: heavy nucleons are organized in a Coulomb lattice and embedded in a strongly degenerate, almost ideal, electron gas. As the electron Fermi energy grows with increasing ρ, electron capture occurs in atomic nuclei: the fractions of neutrons to protons in nuclei increases until neutrons start to drip out producing a free neutron gas. The neutron drip point marks the beginning of the inner crust, whose extent is about 1 km and whose density increases from ρ_{ND} to $\sim 0.5\ \rho_0$, where $\rho_0 = 2.8 \times 10^{14}$ g cm^{-3} is the saturation nuclear matter density, i.e. the mass density of nucleon matter in heavy atomic nuclei. The matter of the inner crust consists of electrons, free neutrons, and neutron-rich atomic nuclei. The fraction of free neutrons increases with growing density. The neutronization at $\rho \sim \rho_{ND}$ greatly softens the EOS, but at the crust bottom the repulsive short-range component of the neutron-neutron interaction comes into play and introduces a considerable stiffness. The nuclei disappear at the crust-core interface. Free neutrons in the inner crust and nucleons confined in the atomic nuclei can be

in superfluid state. The next layer, the outer core, is several kilometers thick and has a density in the range $0.5\ \rho_0 \lesssim \rho \lesssim 2.0\rho_0$. It is mainly composed by neutrons with several per cent admixture of protons, electrons, and possibly muons. The state of this matter is determined by the conditions of electric neutrality and beta equilibrium. All these components are strongly degenerate. The inner core occupies the central region, whose radius can reach several kilometers and whose density can be as high as 10 - 15 ρ_0. Its composition it the biggest unkwown about NSs, and the EOS is very model dependent. We may expect a composition which is similar to the one of the outer core, but even more exotic states are possible. While the EOS for the inner and outer crust receive a wide consensus, because the models can be tested against data produced in Nuclear Physics experiments, for supranuclear densities we only have theoretical models, without many chances of experimental confirmation, at least not unitl GW emission signals coming from the coalescence of binary NSs would be detected.

We are not entering here into the details of the different models proposed for the structure of the inner core, since this goes far beyond the purpose of this Thesis. Actually, as we will point out in Sect. 3, all the NS models we have evolved assume a simple polytropic EOS with adiabatic index $\Gamma = 2$.

1.2 The dynamical bar-mode instability

Newly born NSs may develop dynamical instabilities. In particular, the dynamical bar-mode instability arises when the rotation parameter $\beta := T/|W|$, with T being the rotational kinetic energy and W the gravitational binding energy, exceeds a critical value.

The accurate study of the dynamical barmode instability, of its nonlinear evolution and of the determination of the threshold for its onset, as well as the extraction of physical information from the potential gravitational wave emission, impose the use of a general-relativistic numerical modeling to solve the Einstein's field equations coupled to the hydrodynamics equations in 3+1 dimensions (or the coupled Einstein-Maxwell-MHD equations if magnetic fields are involved, as in the cases discussed in the present thesis).

In this Section, we will review the most significant results about dynamical instabilities in NSs, and in particular the general features of the dynamical bar-mode instability obtained by means of numerical simulations in recent years, focusing our attention on the unmagnetized relativistic case and on the Newtonian case in the presence of magnetic fields.

1.2.1 A brief literature review on dynamical instabilities

Non-axisymmetric deformations of rapidly rotating bodies are rather generic phenomena in Nature and can appear in a wide class of systems. Particularly interesting within an astrophysical context are those deformations taking place in fluids that are self-gravitating. The literature has a long history on this topic, dating back to the work of [44] on incompressible Newtonian uniformly rotating bodies. Since then, the study of these instabilities has continued over the years both in Newtonian gravity and in full General Relativity.

Special attention has traditionally been paid to the study of $m = 2$ instabilities, which are characterized by the exponential growth of $m = 2$ deformations, where m denotes the azimuthal dependence $\mathrm{e}^{\mathrm{i}m\phi}$ in a standard mode decomposition in cylindrical harmonics. Most of the interest in this type of deformation in compact stars arises from the fact that it has the shortest growth time and possibly leads to the emission of a strong gravitational-wave signal. The development of non-axisymmetric instabilities is commonly analyzed in terms of the above-mentioned quantity β, that provides a dimensionless measure of the amount of angular momentum that can be tapped to feed the development of the instabilities. The dynamical bar-mode instability is not the only $m = 2$ instability which may develop in neutron stars.

In the past few years, another kind of $m = 2$ instability has been numerically discovered in differentially rotating Newtonian stars [45] for values of $\beta \sim 0.01$, therefore well below the expected values for the onset of a dynamical bar-mode instability. This appears in stars with a large degree of differential rotation and grows on a timescale which is longer but comparable with the dynamical one. This instability has been referred to as the "low-$T/|W|$ instability" and its dependence on the polytropic index and on the degree of differential rotation has been studied in [46]. Since then, the instability has been observed or discussed in a number of related studies [47, 48, 49, 50, 51, 52, 53], all of which have highlighted the possible occurrence of this type of instability during the collapse of a massive stellar core. In particular, this instability has been studied in great detail by Watts and collaborators [8, 54], which recognize the low-$T/|W|$ instabilities as the manifestation of a more generic class of instabilities, the *shear instabilities* [8] , that is unstable oscillations that do not exist in uniformly rotating systems associated to the existence of a corotation band [55, 56]. In fact, a condition that is often associated to the instability is "corotation", that is the presence of a point at which the star rotates at the same pattern speed of the unstable mode [8]. An alternative suggestion for an associated condition has been made also by Ou and Tohline [48], who instead associate the development of the instability to the presence of a minimum in the vortensity profile of the star which can then drive unstable not only the corotating $m = 2$-modes but also the odd modes such as the $m = 1$ and $m = 3$-modes [57]. This instability has also been studied in [12], where simulations of differentially rotating neutron-star models described by a realistic SLy EOS [58] were performed. They find the development of a bar-mode instability growing on a dynamical timescale, even when the initial axisymmetric model is well below the critical limit for the dynamical bar-mode instability. These results, which match well the phenomenological scenario portrayed in [8], suggest therefore that the idea of a low-$T/|W|$ instability is indeed misleading and should be replaced by the more general one of "shear instability". Depending then on the degree of rotation and of differential rotation, the instability will develop on timescales that are comparable to the dynamical one (as reported here) or on much longer ones (as reported in the first low-$T/|W|$ instability studies).

Besides dynamical instabilities, which are purely hydrodynamical, *secular* instabilities are also possible in rotating compact stars and these are instead triggered by dissipative processes, such as viscosity or radiation emission. If, in particular, the dissipative mechanism is the emission of gravitational radiation, then the secular instability is also known as Chandrasekhar-Friedman-Schutz or CFS instability [59, 60]. Contrary to what their name may suggest, secular

instabilities do not necessarily develop on secular timescales (although they normally do) and are characterized by having a much smaller threshold for the instability. Once again, in the case of a Newtonian polytrope, the critical secular instability parameter is as small as $\beta_c \sim 0.14$ and thus much more easy to attain in astrophysical circumstances.

1.2.2 The bar-mode instability in unmagnetized relativistic stars

Much of the literature on the dynamical bar-mode instability before 2000 has been limited to a Newtonian or post-Newtonian (PN) description. While this represents an approximation, these studies have provided important information on several aspects of the instability that could not have been investigated with perturbative techniques. In particular, these numerical studies have shown that in the case of a Newtonian incompressible self-gravitating polytrope the dynamical bar-mode instability develops for $\beta \geq 0.2738$ [44], this critical threshold depending weakly on the stiffness of the equation of state (EOS) and that, once a bar has developed, the formation of spiral arms is important for the redistribution of the angular momentum (see Refs. [61, 62, 63, 64, 65, 66, 67, 68, 69]). Afterward, it was shown that the threshold can be smaller for stars with a high degree of differential rotation and a weak dependence on the EOS was confirmed in Refs. [70, 71, 72, 73, 74].

Only in the last fifteen years it has become possible to perform simulations of the dynamical bar instability in full General Relativity [10, 75]. These studies have shown that within a fully general-relativistic framework the critical value for the onset of the instability is smaller than the Newtonian one (*i.e.,* $\beta_c \simeq 0.24 - 0.25$) and this behavior was confirmed by PN calculations [76, 77] which also showed that β_c varies with the compactness M/R of the star.

The numerical simulations presented in [10] revealed that the critical threshold for the onset of the dynamical bar-mode instability in neutron star models with a polytropic EOS with polytropic index $\Gamma = 2$ is $\beta_c \sim 0.255$ and that the instability is in general short-lived, the bar-deformation being suppressed over a timescale of a few revolutions (this was later confirmed in Ref. [13]).

The qualitative behavior of the evolution of bar-mode unstable stellar models is shown in Fig. 1.2 and 1.3. In particular, in Fig. 1.2 we show the power P_m in the first four non axi-symmetric m-modes (cf., Eq. (3.18)). It's important to note that at the beginning of the simulation, as a result of the Cartesian discretization, the m=4 mode has the largest power. While this can be reduced by increasing the resolution, the m=4 deformation plays no major role in the development of the instability, which is soon dominated by the lower-order modes.

This figure allows us to easily divide the dynamics of the bar in four representative stages, which are shown in Fig. 1.3 with representative snapshots of the rest-mass density, one for each phase. In particular, here we report the evolution of model `U11-1.0e14`, one of the models we evolved for this work (cf., Chap. 3), which is actually magnetized with an initial magnetic field $B \sim 10^{14}$ G. Anyway, as we will show in Chap. 5, a magnetic field with this strength have negligible effects on the onset and development of the bar-mode instability, so these snapshots can be used here with confidence to describe the qualitative evolution in the case of unmagnetized models. In the initial phase of the instability [stage *(a)*] we observe an exponential growth of the m=2 mode and m=3 mode, the latter one having a smaller growth rate. A first interesting mode coupling takes place when the exponentially growing m=3 mode reaches the same power amplitude of the m=4 mode, at which point the two modes exchange their dynamics, with the m=4 mode growing exponentially and the m=3 mode reaching saturation. At approximately the same time, the m=1 mode also starts to grow exponentially but with a growth rate which is smaller than that of the other modes. Note that this "mode-amplitude crossing" between the m=3 and m=4 modes also signals the time when collective phenomena start to be fully visible. For a qualitative picture of a typical unstable model in this phase see the upper-left panel of Fig. 1.3. This stage continues until the m=2 mode reaches its maximum power and the bar has reached its largest extension. In the second phase [stage *(b)*] the instability reaches saturation and we observe the formation of spiral arms which are responsible for ejecting a small amount of matter and for a progressive attenuation of the bar extension. Furthermore, when the exponentially growing m=1 mode reaches the same power amplitude of the m=3 mode, the latter, whose growth had slowed down for a while, returns to grow exponentially (see the upper-right panel of Fig. 1.3). In the following phase of the instability [stage *(c)*] the m=1, 3 and 4 modes reach comparable powers and this marks the time when the bar deformation has a sudden decrease. As a result of this crossing among the three modes, only the m=1 mode will continue to grow, while the m=3 and the m=4 modes are progressively damped (see the lower-left panel of Fig. 1.3 Finally, the last phase [stage *(d)*] starts when the growing m=1 mode reaches power amplitudes comparable with those of the m=4 mode and the final mode-amplitude crossing takes place. This marks the suppression of the bar deformation and the emergence of an almost axisymmetric configuration (see the upper-left panel of Fig. 1.3). Note that, since the coordinate times at which the four different stages occur is different for different unstable models (and for different resolutions), in Fig. 1.2 no labels have

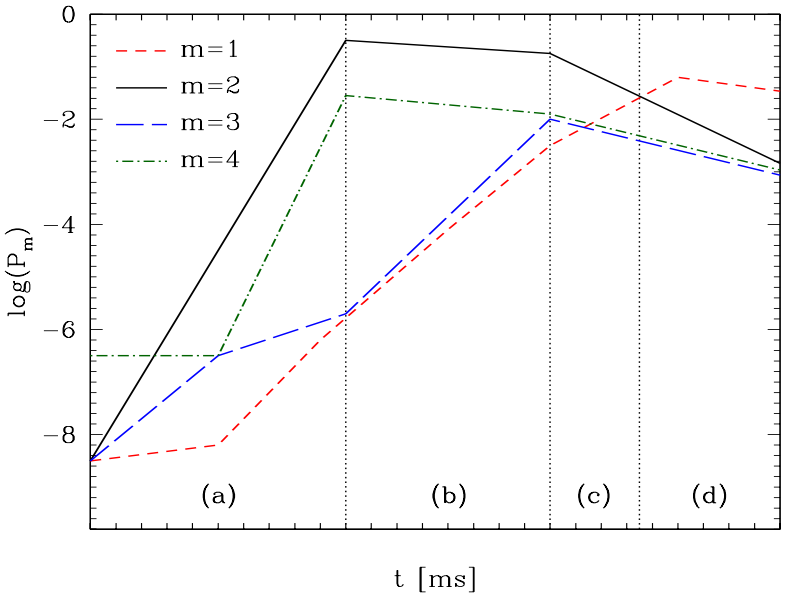

Figure 1.2: Schematic evolution of the collective modes [Eq. 3.18] of the rest-mass density ρ. The dynamics of the instability can be distinguished in four representative stages: *(a)* onset and exponential growth of the instability; *(b)* saturation and development of spiral arms; *(c)* attenuation of the bar deformation; *(d)* suppression and emergence of an almost axisymmetric configuration.

been indicated in the x-axis, but ticks every ms are still present just as an indication for an approximate duration of the different phases.

We can summarize the general and common features on the dynamical bar-mode instability in the unmagnetized case we obtained at the very beginning of our work by evolving stellar models with zero magnetic fields, which confirm the results presented in [10], as follows:

- the bar-deformation is not a persistent phenomenon but is suppressed rather rapidly over a timescale which is of the order of the dynamical one and strongly depends on the degree of overcriticality;

- nonlinear mode-coupling effects (especially between the m=1 and the m=2-mode) take place during the evolution and allow for the growth of other modes besides the fastest growing m=2-mode: this has the overall impact of depriving the m=2-mode of energy with a progressive attenuation of the bar deformation after the instability has saturated, limiting its persistence;

- for slightly overcritical models (*e.g.,* U3, for which $\beta = 0.2596$), when the power-amplitude of the m=1-mode has become comparable with the one in the m=2-mode, the

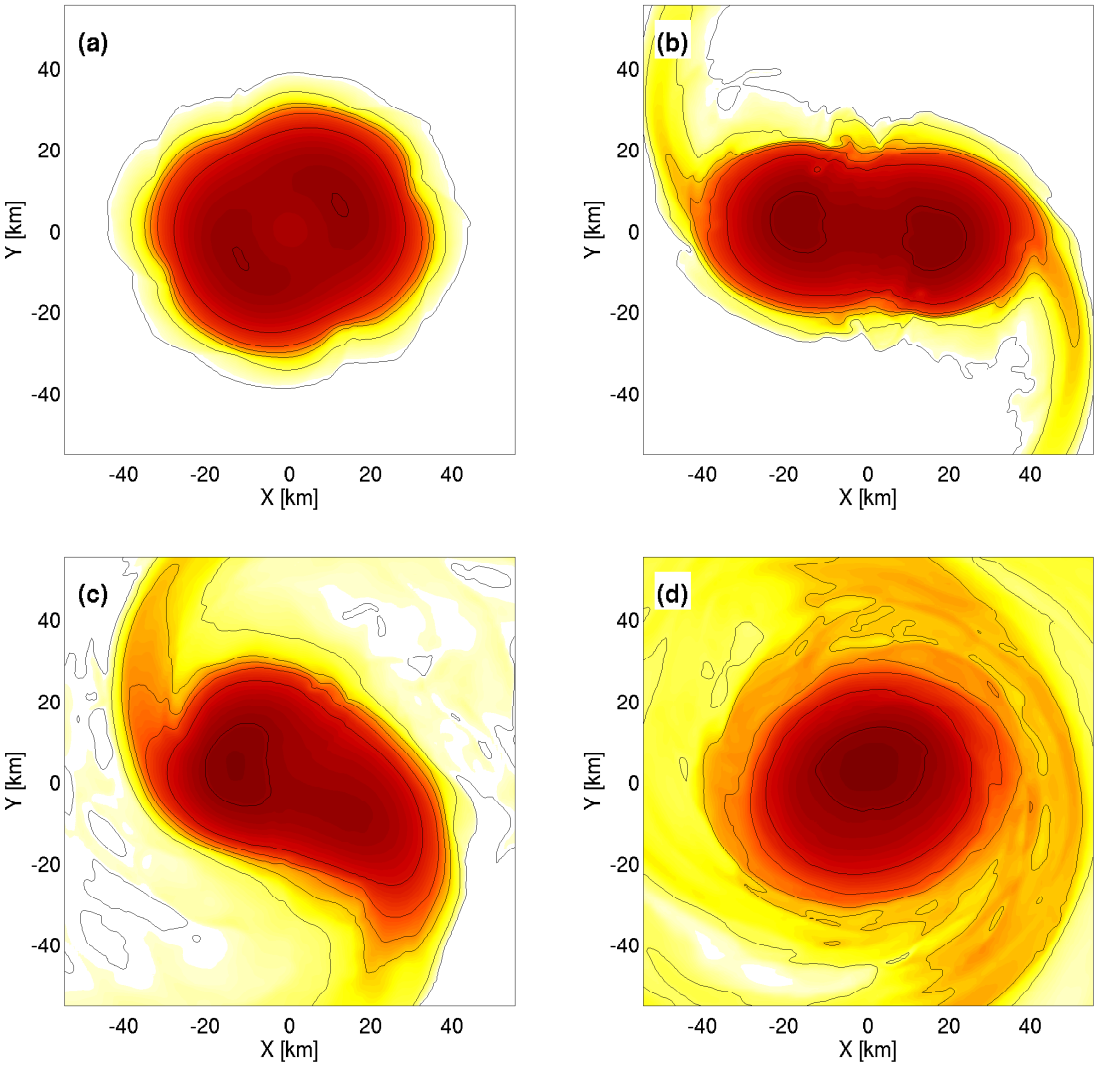

Figure 1.3: Snapshots of the rest-mass density for model `U11-1.0e14`, which is only weakly magnetized and whose evolution is the same as for unmagnetized models (cf., Chap. 5). Each panel represents on the four main phases of the evolution. In the initial phase [stage *(a)*] an exponential growth of the m=2 mode occurs and collective phenomena start to be fully visible. In the second phase [stage *(b)*] the instability reaches saturation and we observe the formation of spiral arms. In the third phase [stage *(c)*] the bar deformation has a sudden decrease. Finally, in the last phase [stage *(d)*] we observe the suppression of the bar deformation and the emergence of an almost axisymmetric configuration.

instability is suppressed, the bar deformation significantly reduced and the star evolves towards an almost axisymmetric configuration;

- for largely overcritical models (*e.g.,* U13, for which $\beta = 0.2812$), the dynamics of the instability are so violent and the stellar model so far from equilibrium that the strong bar-deformation is lost even in the absence of mode-coupling effects, through the conversion of kinetic energy into internal one.

1.2.3 The bar-mode instability in magnetized Newtonian stars

The dynamical bar-mode instability has already been studied by means of numerical simulations of stellar models in the presence of magnetic fields, both initially toroidal and poloidal, but only in the Newtonian case [20].

The main results of this work is that purely toroidal seed magnetic fields are not able to affect the dynamical evolution of the stars, regardless of initial field amplitude. On the contrary, models with initially poloidal magnetic fields evolve differently than unmagnetized cases if the initial field amplitude is large, showing a growing impact on the bar formation with increasing field strength.

In cases with a low magnetization, the magnetic pressure being always less than a few percent of the fluid pressure, the magnetic field has little effects on the growth of the $m = 2$ mode and so on the bar dynamics. In the presence of intermediate magnetic fields, a bar forms with a shape and a growth similar to the zero magnetization case, but with a temporal delay and all the non-axisymmetric modes exhibits slightly smaller amplitudes. Lastly, when strong magnetic field are present, the magnetic pressure reaching about 80% of the fluid pressure within a few dynamical times, there is no indication that a structure with the shape of a bar is going to form at at all.

The overall conclusion is that the effect of magnetic fields on the emergence of the bar-mode instability in the Newtonian case is not likely to be very significant, except in special cases where NSs are born very highly magnetized.

Moreover, in all cases where the initial field is purely poloidal, an increase in the overall magnetic pressure is observed, mainly due to an increase in the azimuthal contribution since the field lines show an immediate and dramatic stretching in the azimuthal direction. This behavior is characteristic of the Ω-dynamo, which one would expect to be active when a poloidal magnetic field is present. Another interesting result is that the late time saturation level of

the inverse "plasma beta" $1/\beta_B$, where β_B is the ratio of the fluid pressure over the magnetic pressure, is approximately the same for all models with initial purely poloidal magnetic field, as well as in the toroidal cases. This independence from the initial field strength and orientation indicates that a common and robust physical mechanism is at play, determining the final saturation level. Moreover, the final magnitude of the azimuthal component is approximately the same in all poloidal cases, and the second most significant component - the radial one - always ends up within an order of magnitude below the azimuthal component. This suggests that these two components have either achieved a static final configuration common to all the simulations, or they are feeding off of one another and exchanging energy with the gas through some equilibrium process. The latter is consistent with expectations of the MRI, which gradually takes over as the Ω-dynamo saturates, and which is expected to be active in all those stellar models.

Keeping all these results in mind, we have decided to perform many 3D numerical simulation of similar stellar models, all with initial purely poloidal magnetic fields (since the effects of purely toroidal fields has proved to be negligible), in order to study the onset and development of the dynamical bar-mode instability, as well as the evolution of the magnetic field itself, in a full general-relativistic framework.

Chapter 2

Mathematical setup

A relativistic description of fluid-dynamics is needed when studying many astrophysical systems like compact stars, flows around compact objects, jets emerging from galactic nuclei and gamma-ray burst engines. A treatment within a Special Relativistic framework is appropriate for astrophysical jets, but General Relativity becomes mandatory when the gravitational field is strong enough, as in the vicinity of a compact object. Besides, in several astrophysical scenarios both magnetic and gravitational fields play an important role in determining the structure and the evolution of the matter, like in the case of highly magnetized NSs. The equations of General Relativistic Magnetohydrodynamics (GRMHD) consist of the local conservation laws for the stress-energy tensor, which must be solved coupled to the Einstein field equations for the metric tensor, and the Maxwell equations for the evolution of the magnetic field. This system of equations is a nonlinear system of PDE, wich must be closed by an algebraic equation, the Equation of State (EOS), and, as mathematical problem, it is usually posed as an Initial Value Problem. This can be solved numerically, within the 3+1 ADM formalism [78], where the matter equations are re-written in a conservative form that allows for a consistent treatment of discontinuities like the ones that are present at the surfaces of stars.

2.1 3+1 formalism

In the so-called "3+1" formulation, e.g., [79], the spacetime $\mathcal{M}$ is assumed to be globally hyperbolic (i.e., admits a Cauchy surface Σ) and, as such, it can be foliated by a family of spacelike hypersurfaces $(\Sigma_t)_{t\in\mathbb{R}}$. This means that there exists a smooth and regular scalar field t on $\mathcal{M}$ such that each hypersurface is a level surface of t and these Σ_t's do not intersect each

other, so that the foliation covers the whole spacetime, i.e., $\mathcal{M} = \bigcup_{t\in\mathbb{R}} \Sigma_t$. The timelike unit 4-vector, normal to Σ_t, is $n_\mu := -\alpha\nabla t$, where the positive function α is called the *lapse* function. The induced 3-metric on Σ_t is given by $\gamma_{\mu\nu} \equiv g_{\mu\nu} + n_\mu n_\nu$ and the (spacelike) *shift vector* is $\beta \equiv \partial_t - \alpha\mathbf{n}$ ($\beta^\mu n_\mu = 0$). Using coordinates adapted to the foliation, the line element of the spacetime in the 3+1 formalism can be written as

$$ds^2 = -(\alpha^2 - \beta_i\beta^i)dt^2 + 2\beta_i dx^i dt + \gamma_{ij}dx^i dx^j, \tag{2.1}$$

where α, β^i and γ_{ij} are functions of the coordinates t, x^i. A key observer associated with the 3+1 splitting is the one with four velocity $\mathbf{n}$ perpendicular to the hypersurfaces of constant t at each event in the spacetime, i.e., the so-called *Eulerian observer*, which reduces to the locally non-rotating or zero angular momentum (ZAMO) observer in the case of axisymmetric and stationary spacetimes. The contravariant and covariant components of $\mathbf{n}$ are given by $n^\mu = (1/\alpha, -\beta^i/\alpha)$ and $n_\mu = (-\alpha, 0, 0, 0)$, respectively. In spacetimes containing matter, an additional natural observer is the one that follows the fluid during its motion, also called the *comoving observer*, with four-velocity $\mathbf{u}$. With the standard definition, the three-velocity of the fluid as measured by the Eulerian observer can be expressed as

$$v^i = \frac{u^i}{\alpha u^t} + \frac{\beta^i}{\alpha}, \tag{2.2}$$

while $v_i = u_i/W$, where $W \equiv 1/\sqrt{1-v^2} = \alpha u^t$ is the Lorentz factor ($v^2 = \gamma_{ij}v^i v^j$). At this point, the 3+1 formalism allows to consider the four dimensional PDEs as "time"-evolution equations on the foliation coordinate t for variables defined on the three-dimensional spacelike foliation Σ.

2.2 Equations for the evolution of fields and matter

Einstein equations

The original ADM formulation casts the Einstein equations into a first-order (in time) quasi-linear [80] system of equations. The dependent variables are the three-metric γ_{ij} and the ex-

trinsic curvature K_{ij}, with first-order evolution equations given by

$$\partial_t \gamma_{ij} = -2\alpha K_{ij} + \nabla_i \beta_j + \nabla_j \beta_i, \tag{2.3}$$

$$\begin{aligned} \partial_t K_{ij} = & -\nabla_i \nabla_j \alpha + \alpha \Bigg[R_{ij} + K\, K_{ij} - 2K_{im} K^m_j \\ & -8\pi \left(S_{ij} - \frac{1}{2}\gamma_{ij} S \right) - 4\pi \rho_{\mathrm{ADM}} \gamma_{ij} \Bigg] \\ & +\beta^m \nabla_m K_{ij} + K_{im} \nabla_j \beta^m + K_{mj} \nabla_i \beta^m. \end{aligned} \tag{2.4}$$

Here, α is the lapse function, β_i is the shift vector, ∇_i denotes the covariant derivative with respect to the three-metric γ_{ij}, R_{ij} is the Ricci curvature of the three-metric, $K \equiv \gamma^{ij} K_{ij}$ is the trace of the extrinsic curvature, S_{ij} is the projection of the stress-energy tensor onto the space-like hypersurfaces and $S \equiv \gamma^{ij} S_{ij}$ (for a more detailed discussion, see [81]). In addition to the evolution equations, the Einstein equations also provide four constraint equations to be satisfied on each space-like hypersurface. These are the Hamiltonian constraint equation

$$\mathcal{H} = {}^{(3)}R + K^2 - K_{ij} K^{ij} - 16\pi \rho_{\mathrm{ADM}} = 0\,, \tag{2.5}$$

and the momentum constraint equations

$$\nabla_j K^{ij} - \gamma^{ij} \nabla_j K - 8\pi j^i = 0\,. \tag{2.6}$$

In equations (2.3)–(2.6), ρ_{ADM} and j^i are the energy density and the momentum density as measured by an observer moving orthogonally to the space-like hypersurfaces.

In particular, we use a conformal traceless reformulation of the above system of evolution equations, as first suggested by Nakamura, Oohara and Kojima [82] (NOK formulation), in which the evolved variables are the conformal factor (ϕ), the trace of the extrinsic curvature (K), the conformal 3-metric ($\tilde{\gamma}_{ij}$), the conformal traceless extrinsic curvature ($\tilde{A}_{ij}$) and the *conformal connection functions* ($\tilde{\Gamma}^i$), defined as

$$\phi = \frac{1}{4} \log(\sqrt[3]{\gamma}) \quad , \tag{2.7}$$

$$K = \gamma^{ij} K_{ij} \quad , \tag{2.8}$$

$$\tilde{\gamma}_{ij} = e^{-4\phi} \gamma_{ij} \quad , \tag{2.9}$$

$$\tilde{A}_{ij} = e^{-4\phi} (K_{ij} - \gamma_{ij} K) \quad , \tag{2.10}$$

$$\tilde{\Gamma}^i = \tilde{\gamma}^{ij}_{,j} \quad . \tag{2.11}$$

The code used for evolving these quantities is the one developed within the `Cactus` computational toolkit [83] and is designed to handle arbitrary shift and lapse conditions. In particular, we have used hyperbolic K-driver slicing conditions of the form

$$\partial_t \alpha = -f(\alpha)\, \alpha^2 (K - K_0), \tag{2.12}$$

with $f(\alpha) > 0$ and $K_0 \equiv K(t = 0)$. This is a generalization of many well known slicing conditions. For example, setting $f = 1$ we recover the "harmonic" slicing condition, while, by setting $f = q/\alpha$, with q an integer, we recover the generalized "1+log" slicing condition [84]. In particular, all the simulations discussed in this Thesis are done using condition (2.12) with $f = 2/\alpha$. This choice has been made mostly because of its computational efficiency, but we are aware that "gauge pathologies" could develop with the "1+log" slicings [85, 86].

As for the spatial gauge, we use one of the "Gamma-driver" shift conditions proposed in [87], that essentially acts so as to drive the $\tilde{\Gamma}^i$ to be constant. In this respect, the "Gamma-driver" shift conditions are similar to the "Gamma-freezing" condition $\partial_t \tilde{\Gamma}^k = 0$, which, in turn, is closely related to the well-known minimal distortion shift condition [88].

In particular, all the results reported here have been obtained using the hyperbolic Gamma-driver condition,

$$\partial_t^2 \beta^i = F\, \partial_t \tilde{\Gamma}^i - \eta\, \partial_t \beta^i, \tag{2.13}$$

where F and η are, in general, positive functions of space and time. For the hyperbolic Gamma-driver conditions it is crucial to add a dissipation term with coefficient η to avoid strong oscillations in the shift. Experience has shown that by tuning the value of this dissipation coefficient it is possible to almost freeze the evolution of the system at late times. We typically choose $F = \frac{3}{4}\alpha$ and $\eta = 2$ and do not vary them in time.

Maxwell equations

The electromagnetic field is completely described by the Faraday electromagnetic tensor field $F^{\mu\nu}$ obeying Maxwell equations

$$\nabla_\mu {}^*F^{\mu\nu} = 0, \tag{2.14}$$

$$\nabla_\mu F^{\mu\nu} = 4\pi \mathcal{J}, \tag{2.15}$$

where ∇ is the covariant derivative with respect to the four-metric g, $\mathcal{J}$ is the charge current four-vector and ${}^*F$ is the dual of the electromagnetic tensor defined as

$${}^*F^{\mu\nu} = \frac{1}{2}\eta^{\mu\nu\lambda\delta} F_{\lambda\delta}, \tag{2.16}$$

$\eta^{\mu\nu\lambda\delta}$ being the Levi-Civita pseudo-tensor. A generic observer with four-velocity U will measure a magnetic field B and an electric field E given by

$$E^\alpha \equiv F^{\alpha\beta}U_\beta, \tag{2.17}$$

$$B^\alpha \equiv {}^*F^{\alpha\beta}U_\beta, \tag{2.18}$$

and the charge current four-vector $\mathcal{J}$ can be in general expressed as

$$\mathcal{J}^\mu = qu^\mu + \sigma F^{\mu\nu}u_\nu, \tag{2.19}$$

where q is the proper charge density and σ is the electric conductivity.

Hereafter we will assume our fluid to be a perfect conductor ($\sigma \to \infty$, ideal MHD limit) and so, in order to keep the current finite, that $F^{\mu\nu}u_\nu = 0$, i.e. the electromagnetic tensor and its dual can be written exclusively in terms of the magnetic field $\boldsymbol{b}$ measured in the comoving frame in the form

$$F^{\mu\nu} = \epsilon^{\mu\nu\alpha\beta}u_\alpha b_\beta, \tag{2.20}$$

$${}^*F^{\mu\nu} = b_\mu u_\nu - b_\nu u_\mu, \tag{2.21}$$

with the Maxwell equations taking the simple form

$$\nabla_\nu {}^*F^{\mu\nu} = \frac{1}{\sqrt{-g}}\,\partial_\nu\left(\sqrt{-g}(b^\mu b^\nu - b^\nu b^\mu)\right) = 0. \tag{2.22}$$

In order to express these equations in terms of quantities measured by an Eulerian observer, we need to compute the relation between the magnetic field measured by the comoving and by the Eulerian observers, respectively $\boldsymbol{b}$ and $\boldsymbol{B}$. To do that, we introduce the projection operator $P_{\mu\nu} \equiv g_{\mu\nu} + u_\mu u_\nu$ orthogonal to $\boldsymbol{u}$. If we apply this operator to the definition of the magnetic field $\boldsymbol{B}$ measured by an Eulerian observer, we can easily derive the following relations

$$b^0 = \frac{WB^i v_i}{\alpha},\ b^i = \frac{B^i + \alpha b^0 u^i}{W},\ b^2 \equiv b^\mu b_\nu = \frac{B^2 + \alpha^2 (b^0)^2}{W^2}, \tag{2.23}$$

where $B^2 \equiv B^i B_i$. The time component of equations 2.22 provides the divergence-free condition

$$\partial_i \mathcal{B}^i = 0, \tag{2.24}$$

where $\mathcal{B}^i \equiv \sqrt{\gamma}B^i$ and γ is the determinant of γ_{ij}. The spatial components of equations 2.22, on the other hand, yield the induction equations for the evolution of the magnetic field

$$\partial_t \mathcal{B}^i = \partial_j(\tilde{v}^i \mathcal{B}^j - \tilde{v}^j \mathcal{B}^i), \tag{2.25}$$

where $\tilde{v}^i \equiv \alpha v^i - \beta^i$.

Conservation equations

The stellar models are here treated in terms of a perfect fluid in hydrodynamical equilibrium, with a super-imposed purely poloidal magnetic field.

The fluid part is thus described by a stress-energy tensor in the form

$$T^{\mu\nu}_{\text{fluid}} = \rho h u^\mu u^\nu + p g^{\mu\nu}, \tag{2.26}$$

where $h = 1+\epsilon+p/\rho$ is the specific enthalpy, ϵ the specific internal energy and ρ the rest-mass density, so that $e = \rho(1+\epsilon)$ is the energy density in the rest-frame of the fluid.

The contribution from the magnetic field is described in terms of a stress-energy tensor in the form

$$\begin{aligned} T^{\mu\nu}_{\text{EM}} &= F^{\mu\sigma}F^{\nu}{}_{\sigma} - \frac{1}{4} g^{\mu\nu} F_{\alpha\beta}F^{\alpha\beta} = \\ &= \left(u^\mu u^\nu + \frac{1}{2} g^{\mu\nu}\right) b^2 - b^\mu b^\nu, \end{aligned} \tag{2.27}$$

The equations of relativistic magneto-hydrodynamics are then given by the conservation laws for the total energy-momentum

$$T^{\mu\nu} = (\rho h + b^2) u^\mu u^\nu + \left(p + \frac{b^2}{2}\right) g^{\mu\nu} - b^\mu b^\nu \tag{2.28}$$

and for the baryon number in the form

$$\begin{aligned} &\nabla_\mu T^{\mu\nu} = 0 \,, \\ &\nabla_\mu (\rho u^\mu) = 0 \,, \end{aligned} \tag{2.29}$$

once supplemented with an EOS of type $p = p(\rho, \epsilon)$. While the code has been written to use any EOS, all the simulations presented here have been performed using either an isentropic "polytropic" EOS

$$p = K\rho^\Gamma \,, \tag{2.30}$$

where K is the polytropic constant and Γ the adiabatic exponent.

An important feature of the `Whisky` code is the implementation of a *conservative formulation* of the hydrodynamics equations in which the set of equations (2.29) is written in a hyperbolic, first-order and flux-conservative form of the type

$$\partial_t \mathbf{q} + \partial_i \mathbf{f}^{(i)}(\mathbf{q}) = \mathbf{s}(\mathbf{q}) \,, \tag{2.31}$$

where $\mathbf{f}^{(i)}(\mathbf{q})$ and $\mathbf{s}(\mathbf{q})$ are the flux-vectors and source terms, respectively (see ref. [89] for an explicit form of the equations). Note that the right-hand side (the source terms) depends only on the metric, and its first derivatives, and on the stress-energy tensor. In order to write system (2.29) in the form of system (2.31), the *primitive* hydrodynamical variables ***i.e.*** the rest-mass density ρ and the pressure p (measured in the rest-frame of the fluid), the fluid three-velocity v^i and the magnetic field B^i (measured by a local zero–angular-momentum observer), the specific internal energy ϵ and the Lorentz factor $W = \alpha u^0$) are mapped to the so called *conserved* variables $\mathbf{q} \equiv (D, S^i, \tau, \mathcal{B}^k)^T$ via the relations

$$\begin{aligned} D &\equiv \sqrt{\gamma} W \rho \,, \\ S^i &\equiv \sqrt{\gamma}(\rho h + b^2) W^2 v^i - \alpha \sqrt{\gamma} b^0 b^i \,, \\ \tau &\equiv \sqrt{\gamma}\left[(\rho h + b^2) W^2 - \left(p + \frac{b^2}{2}\right) - \alpha^2 (b^0)^2\right] - D \,, \\ \mathcal{B}^i &\equiv \sqrt{\gamma} B^i . \end{aligned} \tag{2.32}$$

As previously noted, in the case of the polytropic EOS (2.30), one of the evolution equations (namely the one for τ) does not need to be solved as the internal energy density can be readily computed by inverting the relation $p = (\Gamma - 1)\,\rho\,\epsilon$. Additional details of the formulation we use for the MHD equations can be found in [89].

Chapter 3

Numerical setup and methodology

3.1 Numerical code and settings

The code and the evolution method are the same as the ones used in Baiotti et al. [90, 91] and therein described. For convenience we report here the main properties and characteristics of the employed simulation method. The simulations have been carried out using the general-relativistic ideal-MHD (GRMHD) code `WhiskyMHD` [24, 92, 93]. The code provides a 3D numerical solution of the full set of the GRMHD equations in flux-conservative form on a dynamical background in Cartesian coordinates. It is based on the same high-resolution shock-capturing (HRSC) techniques on domains with adaptive mesh refinements (AMR) [94, 95]) as discussed in [91] within the Cactus framework [96, 97]. The reconstruction method adopted is the one discussed in the piecewise parabolic method (PPM) [98], while the Harten-Lax-van Leer-Einfeldt (HLLE) approximate Riemann solver [99] has been employed in order to compute the fluxes. The divergence of the magnetic field is enforced to stay within machine precision by employing the flux-CD approach as implemented in [93], but with the difference that we adopt as evolution variable the vector potential instead of the magnetic field. This method ensures the divergence-free character of the magnetic field since the field is computed as the curl of the evolved vector potential using the same finite-differencing operators as the ones for computing the divergence of the magnetic field. Because of the gauge invariance of Maxwell equations, a choice needs to be made and we have opted for the simplest one, namely, the algebraic Maxwell gauge. This choice can introduce some spurious oscillations close to the AMR boundaries in highly dynamical simulations, but this has not been the case for the simulations reported here. On the other hand, it has allowed us to keep the divergence of the

magnetic field essentially nearly at machine precision. A more advanced prescription has been also introduced recently in Ref. [100]; this approach requires a certain amount of tuning for optimal performance and will be considered in future works. Additional information on the code can also be found in Refs. [92, 93].

Furthermore, to remove spurious post-shock oscillations in the magnetic field, a fifth-order Kreiss-Oliger type of dissipation [101] to the vector potential evolution equation with a dissipation parameter of 0.1 has been added. Finally, the evolution of the gravitational fields is obtained through the `CCATIE` code, which provides the solution of the conformal traceless formulation of the Einstein equations [102, 103], which was first introduced by Nakamura, Oohara and Kojima [82].The time integration of the evolution equations is achieved through a third-order accurate Runge-Kutta scheme.

Essentially all of the simulations presented in this Thesis use a 3D Cartesian grid with four refinement levels and with outer boundaries located at a distance ~ 150 km from the center of the grid, which is approximately five times the stellar radius[1]. The finest resolution is $\Delta x \simeq 0.375\, M_\odot \simeq 550$ m (between 40 and 60 points across the stellar radius, depending on the model) for all the simulations we performed with the main aim of studying the dynamics of the bar-mode instability (this resolution is high enough for this purpose, cf., [10] where $\Delta x \simeq 0.500\, M_\odot \simeq 740$ m). The further runs we used to search for the magnetorotational instability have instead a finer grid such that $\Delta x \simeq 0.256\, M_\odot \simeq 380$ m (i.e., 60 - 90 points across the stellar radius). Unless stated differently, all the simulations discussed hereafter have been performed imposing a bitant symmetry, i.e., a reflection symmetry across the $z = 0$ plane.

3.2 Initial data

The initial data of our simulations are computed as stationary equilibrium solutions of axisymmetric and rapidly rotating relativistic stars in polar coordinates and without magnetic fields [104]. In generating these equilibrium models we adopt a "polytropic" EOS [105], $p = K\rho^\Gamma$, with $K = 100$ and $\Gamma = 2$, and assume the line element for an axisymmetric and stationary relativistic spacetime to have the form

$$\begin{aligned} ds^2 = &-e^{\mu+\nu}dt^2 + e^{\mu-\nu}r^2\sin^2\theta(d\phi - \omega dt)^2 \\ &+e^{2\xi}(dr^2 + r^2 d\theta^2)\,, \end{aligned} \tag{3.1}$$

[1]Our outer boundaries are too close for an accurate extraction of gravitational radiation, which we expect to be of the order of $10^{-5}\, M_\odot$ [10]. This is also the precision with which we conserve the energy in the system.

Model	ρ_c (10^{-4})	r_p/r_e	A_b
`U13`	0.599	0.200	1.85×10^6
`U11`	1.092	0.250	1.46×10^6
`U3`	1.672	0.294	8.74×10^5
`S1`	1.860	0.307	6.94×10^5
`S6`	2.261	0.336	4.50×10^5
`S7`	2.754	0.370	2.01×10^5
`S8`	3.815	0.443	5.96×10^4

Table 3.1: Parameters we used to generate the initial models for our simulations. In the first column we report the model name, while in the next three we report the central rest-mass density ρ_c, the ratio between the polar and the equatorial coordinate radii r_p/r_e and the parameter A_b of Eq. (3.10) that would generate a magnetic field whose initial maximum value in the (x, y) plane is 1.0×10^{15} G, which represents an intermediate value for the present work. Unless explicitly stated, all these quantities are expressed in geometrized units in which $G = c = M_\odot = 1$.

where μ, ν, ω and ξ are space-dependent metric functions. To reach the large angular momentum needed to trigger the dynamical bar-mode instability, a considerable amount of differential rotation needs to be introduced and we do so following the traditional constant specific angular momentum law ("j-constant") of differential rotation, in which the angular velocity distribution takes the form [106, 107]

$$\Omega_c - \Omega = \frac{1}{\hat{A}^2 R_e^2} \left[\frac{(\Omega - \omega) r^2 \sin^2\theta e^{-2\nu}}{1 - (\Omega - \omega)^2 r^2 \sin^2\theta e^{-2\nu}} \right] , \tag{3.2}$$

where R_e is the coordinate equatorial stellar radius and the coefficient $\hat{A}$ is a measure of the degree of differential rotation, which we set to $\hat{A} = 1$ in analogy with other works in the literature. Once imported onto the Cartesian grid and throughout the evolution, we compute the angular velocity Ω (and the period P) on the (x, y) plane as

$$\Omega := \frac{u^\phi}{u^0} = \frac{u^y \cos\phi - u^x \sin\phi}{u^0 \sqrt{x^2 + y^2}} , \qquad P = \frac{2\pi}{\Omega} . \tag{3.3}$$

Other fundamental quantities of the system, which allow us to describe the main properties of the stellar models we used as initial data for our simulations, are the baryon mass M_0, the gravitational mass M, the angular momentum J, the rotational kinetic energy T, the gravita-

Mod.	R_e [km]	M [$M_\odot$]	M/R_e	J/M^2	Ω_c [rad/s]	Ω_e [rad/s]	T (10^{-2})	W (10^{-2})	β	$\beta_{\rm mag}$ (10^{-6})
U13	35.9	1.462	0.0601	1.753	3647	1607	2.183	7.764	0.2812	5.3
U11	34.4	1.460	0.0627	1.661	3997	1747	2.284	8.327	0.2743	4.7
U3	32.4	1.456	0.0664	1.538	4434	1916	2.352	9.061	0.2596	3.5
S1	31.6	1.460	0.0682	1.497	4593	1976	2.384	9.388	0.2540	3.0
S6	30.0	1.449	0.0713	1.412	4901	2093	2.369	9.859	0.2403	2.3
S7	28.1	1.447	0.0760	1.309	5284	2234	2.360	10.56	0.2234	1.0
S8	26.7	1.439	0.0862	1.121	5995	2482	2.255	11.96	0.1886	0.4

Table 3.2: Main properties of the stellar models evolved in the simulations. In the first column we report the model name, while in the remaining columns we report, from left to right, the proper equatorial radius R_e, the gravitational mass M, the compactness M/R_e, the ratio of the total angular momentum J to M^2 (angular momentum parameter), the angular velocities at the axis $\Omega_c = \Omega(r = 0)$ and at the equator $\Omega_e = \Omega(r = R_e)$, the rotational kinetic energy T and the gravitational binding energy W, their ratio β (*instability parameter*) and finally $\beta_{\rm mag} = E_{\rm mag}/(T+|W|)$ (*magnetization parameter*), corresponding to models with $B^z_{\rm max}|_{t,z=0} = 1.0\times10^{15}$ G. Unless explicitly stated, all these quantities are expressed in geometrized units in which $G = c = M_\odot = 1$.

tional binding energy W and the instability parameter β, calculated as in [108]

$$M_0 := \int d^3x\, \sqrt{\gamma} D\,, \tag{3.4}$$

$$M := \int d^3x\, \alpha\sqrt{\gamma}\left[-2(T_{\rm fl})^0_{\ 0} + (T_{\rm fl})^\mu_{\ \mu}\right]\,, \tag{3.5}$$

$$J := \int d^3x\, \alpha\sqrt{\gamma}(T_{\rm fl})^0_{\ \phi}\,, \tag{3.6}$$

$$T := \frac{1}{2}\int d^3x\, \alpha\sqrt{\gamma}\Omega(T_{\rm fl})^0_{\ \phi}\,, \tag{3.7}$$

$$W := T + E_{\rm int} + M_0 - M\,, \tag{3.8}$$

$$\beta := T/|W|\,, \tag{3.9}$$

where D is the conserved rest-mass density, γ is the determinant of the three-metric and $(T_{\rm fl})^\mu_{\ \nu}$ corresponds to the fluid contributions to the stress-energy tensor. We note that we have defined the gravitational mass and angular momentum taking into account only the fluid part of the energy-momentum tensor and thus neglecting the electromagnetic contributions. This is strictly speaking incorrect, but tolerable given that the relative electromagnetic contributions to the mass and angular momentum are $\lesssim 10^{-5}$. Besides, the definitions above for J, T, W and β are

meaningful only in the case of stationary axisymmetric configurations and should therefore be treated with care once the rotational symmetry is lost. All the equilibrium models are members of a sequence having a constant rest-mass $M_0 \simeq 1.5\, M_\odot$ and are stable to gravitational collapse on the basis of the results of [109].

An initial poloidal magnetic field is added as a perturbation to the initial equilibrium models by introducing a purely toroidal vector potential A_ϕ given by

$$A_\phi = A_b \left(\max(p - p_{\rm cut}, 0)\right)^2 , \tag{3.10}$$

where $p_{\rm cut}$ is 4 % of the maximum pressure, while A_b is chosen in a way to have the chosen value for the maximum of the initial magnetic field B. The Hamiltonian and momentum constraint equations are not solved after superimposing the magnetic field, but we have verified that for the magnetic-field strength considered here, this perturbation introduces only negligible additional violations of the constraints.

In Tab. 3.1 we report the three parameter we used to generate each initial model, namely the central rest-mass density ρ_c and the axis ratio r_p/r_e for the matter configuration, where r_p and r_e are the polar and equatorial coordinate radii respectively, and the coefficient A_b which corresponds to an initial poloidal magnetic field strength equal to 10^{15} G.

The main properties of all the stellar models we have used as initial data are reported in Table 3.2, where we have introduced part of our notation to distinguish the different models. In particular models indicated as `U`$\star$ and as `S`$\star$ refer to NSs that are unstable and stable to the purely dynamical bar-mode instability, respectively. In the left panel of Fig. 3.1, all the initial configurations are reported in a diagram with the instability parameter β versus the compactness M/R. This result was determined in Refs. [10, 11] and confirmed in the initial phase of this work, performing new simulations of these models with zero magnetization and with better resolution than the one employed in the cited papers. The right panel of Fig. 3.1 and the two panels of Fig. 3.2 show the initial profiles of the rest-mass density ρ, of the rotational angular velocity Ω, and of the z-component of the magnetic field for all the models we have evolved. The profiles for the models that are unstable in the unmagnetized case are drawn with blue solid lines, while we use red dot-dashed lines for stable models. Note that the position of the maximum of the rest-mass density coincides with the center of the star only for models with low β; for those with a larger β, the maximum of the rest-mass density resides, instead, on a circle on the equatorial plane.

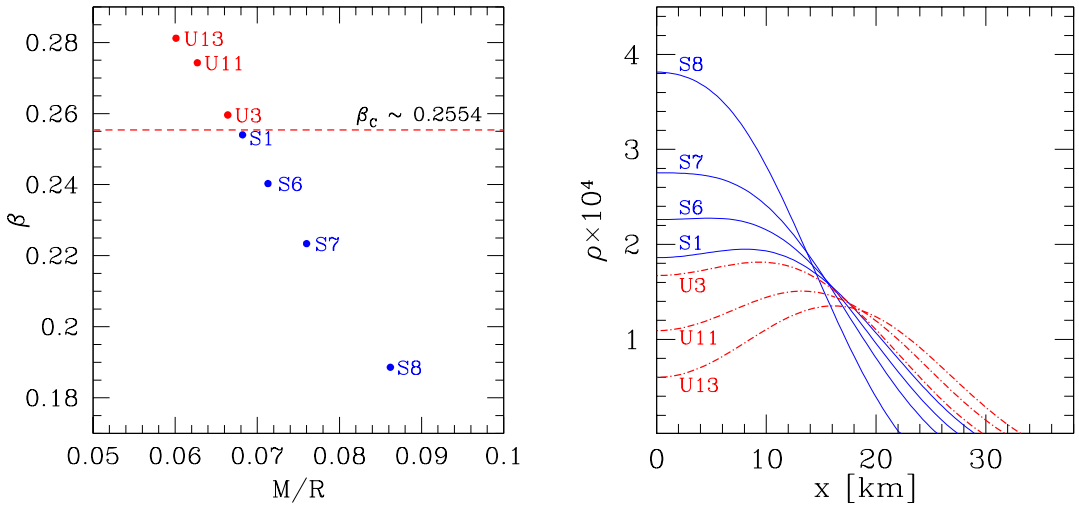

Figure 3.1: *Left panel*: Position on the $(M/R,\ \beta)$ plane of the considered equilibrium stellar models, belonging to a sequence of constant rest-mass $M_0 = 1.5\ M_\odot$. Blue and red circles indicate the models which are stable (`S8`, `S7`, `S6`, `S1`) or unstable (`U3`, `U11`, `U13`) against a bar deformation when no initial magnetic field is present, respectively. The horizontal red dashed line marks the stability threshold. *Right panel*: Initial profiles of the rest-mass density ρ for all the above-mentioned initial models. The profiles of the stable models are here drawn with blue solid lines, while those for the unstable models with red dot-dashed lines.

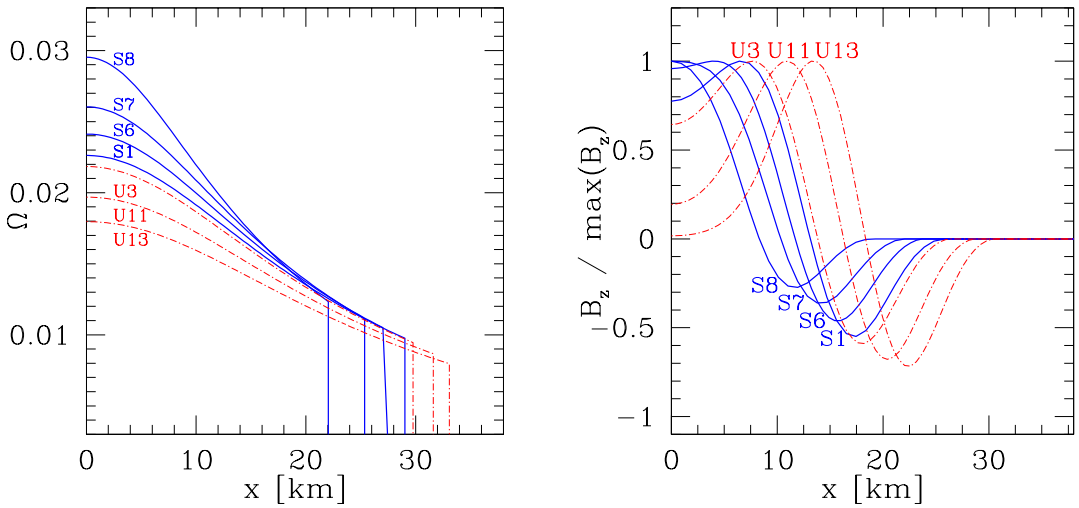

Figure 3.2: Initial profiles of the angular velocity Ω (left panel) and the z-component of the magnetic field (right panel) for the same models as in Fig. 3.1.

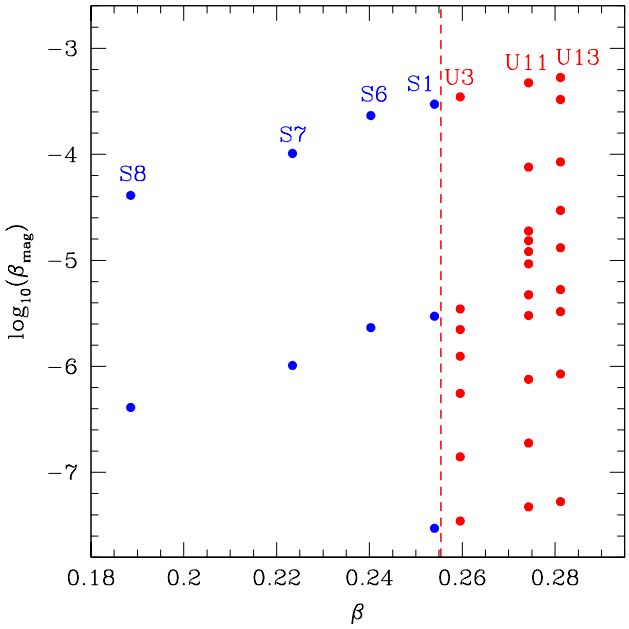

Figure 3.3: Representation of the initial models in a $(\beta, \beta_{\rm mag})$ plane. Blue and red symbols mark models that are respectively bar-mode stable and bar-mode unstable at zero magnetizations, while the vertical red dashed line marks the stability threshold for zero magnetic fields.

The strength of the initial magnetic field can be characterized by the value of the *magnetization parameter* $\beta_{\rm mag}$ which, in analogy with the instability parameter β (cf., Eq. (3.9), we define as

$$\beta_{\rm mag} := E_{\rm mag}/(T + |W|), \tag{3.11}$$

where the total magnetic energy is computed as

$$E_{\rm mag} := \int d^3x\, \alpha^2 \sqrt{\gamma}\, T^{00}_{\rm em}\,. \tag{3.12}$$

This magnetization parameter should not be confused with what is usually defined as the β parameter of a plasma, i.e., the ratio of the fluid pressure to the magnetic pressure.

All the magnetized initial configurations we evolved for our main study about the dynamics of bar-stable and bar-unstable models (cf., Chap. 4 and 5) are reported in Fig. 3.3[1], according to the values of β and $\beta_{\rm mag}$. Here we have a clear representation of the parameter space we intend to explore in the present Thesis by means of numerical simulations. The models that are known to be stable against the bar-mode instability in the unmagnetized case are here drawn

[1]Further weakly magnetized models ($B \lesssim 10^{14}$ G, i.e., $\beta_{\rm mag} \lesssim 5 \times 10^{-7}$) will be presented in Chap. 6, when we focus our attention on the evolution of the magnetic field.

in blue (`S1`, `S6`, `S7` and `S8`), while the unstable ones are drawn in red (`U3`, `U11` and `U13`). The different symbols used in this figure will be further discussed in Sect. 5.1 when illustrating the results of our work about the general effects of the magnetic field on the dynamics of the bar-mode instability; it is sufficient to say for now that squares and triangles refer to unstable models with unmodified and modified growth times, respectively. Hereafter we will also extend our notation and denote a particular magnetized model by marking it by the maximum initial value of the z-component of the magnetic field on the (x, y) plane, i.e., $B^z_{\rm max}|_{t,z=0}$, expressed in Gauss. As an example, the bar-mode unstable model with initial $B^z_{\rm max}|_{t,z=0} = 1.0 \times 10^{15}$ G will be indicated as `U11-1.0e15`.

3.3 Methodology of the analysis and diagnostic

A number of different quantities have been computed during the evolution, in order to monitor the dynamics of the instability and to check that the numerical simulations were providing reasonable results.

A first important set of diagnostic quantities focuses on the detection of a bar deformation, which can be quantified in terms of the distortion parameters [110]

$$\eta_+ := \frac{I^{xx} - I^{yy}}{I^{xx} + I^{yy}}\,, \tag{3.13}$$

$$\eta_\times := \frac{2\, I^{xy}}{I^{xx} + I^{yy}}\,, \tag{3.14}$$

$$\eta := \sqrt{\eta_+^2 + \eta_\times^2}\,, \tag{3.15}$$

where the quadrupole moment of the matter distribution can be computed in terms of the conserved density D as in [10, 111]

$$I^{jk} = \int d^3x\, \sqrt{\gamma} D\, x^j x^k\,. \tag{3.16}$$

Note that all quantities in Eqs. (3.13)–(3.15) are expressed in terms of the coordinate time t and do not represent therefore invariant measurements at spatial infinity. However, for the simulations reported here, the length-scale of variation of the lapse function at any given time is always larger than twice the stellar radius at that time, ensuring that the events on the same time-slice are also close in proper time.

In particular, η_+ can be used to quantify both the growth time $\tau_{\rm bar}$ of the instability and the oscillation frequency $f_{\rm bar}$ of the unstable bar once the instability is fully developed. In practice,

we can obtain a measurement of $\tau_{\rm bar}$ and $f_{\rm bar}$ by performing a nonlinear least-square fit of the computed distortion $\eta_+(t)$ with the trial function

$$\eta_+(t) = \eta_0 \, e^{t/\tau_{\rm B}} \cos(2\pi \, f_{\rm B} \, t + \phi_0) \, . \tag{3.17}$$

In addition, as a tool to describe and understand the nonlinear properties of the development and saturation of the instability, we can decompose the rest-mass density into its Fourier modes so that the "power" of the m-th mode is defined as

$$P_m \equiv \int d^3x \, \rho \, e^{{\rm i}m\phi} \, . \tag{3.18}$$

It is worth stressing here that, despite their denomination, the Fourier modes (3.18) do not represent proper eigenmodes of oscillation of the star. While, in fact, the latter are well defined only within a perturbative regime, the former simply represent a tool to quantify, within a fully nonlinear regime, what are the main components of the rest-mass distribution. Stated differently, we do not expect that quasi-normal modes of oscillations are present but in the initial and final stages of the instability, for which a perturbative description is adequate.

In order to better analyze the effects of magnetic fields on the dynamics of the bar-mode instability, we have introduced additional diagnostic variables to quantify and describe the evolution of the magnetic field itself. For axisymmetric configurations one usually decomposes the magnetic field in toroidal and poloidal components, studying their dynamics separately. When axisymmetry is lost, however, this nice decomposition is no longer available. Nevertheless, there exists a decomposition that can be defined even if axisymmetry is not preserved, which is reduced to the usual poloidal-toroidal one in the axisymmetric stationary case. The main idea of this decomposition is to separate the magnetic field in a component in the direction of the fluid motion and hence parallel to the fluid three-velocity and in a component that is orthogonal to it. We therefore split the magnetic field measured by an Eulerian observer as

$$B^i = B_\parallel \frac{v^i}{\sqrt{\gamma_{ij} v^i v^j}} + B^i_\perp \, , \tag{3.19}$$

where we define the "perpendicular" part of the magnetic field from the condition $B^i_\perp v_i = 0$, while the "parallel" part is a scalar and is trivially defined as $B_\parallel := B^j v_j / (v^i v_i)^{1/2}$. Initially, when the flow is essentially azimuthal, $B^i_\perp$ corresponds to the poloidal component of the magnetic field, while $B_\parallel v^i / (v^j v_j)^{1/2}$ to the toroidal component. Hereafter we will refer loosely to these as the "poloidal" and "toroidal" components, respectively. Within this decomposition,

we can then define the electromagnetic energy contributions associated to the "toroidal" and "poloidal" magnetic-field components as

$$E^{\rm tor}_{\rm mag} := \int d^3x\,\sqrt{\gamma}\,\frac{1}{2}B_{\parallel}B_{\parallel}\,, \tag{3.20}$$

$$E^{\rm pol}_{\rm mag} := \int d^3x\,\sqrt{\gamma}\,\frac{1}{2}\gamma_{ij}B^i_{\perp}B^j_{\perp}(1+\gamma_{rs}v^r v^s)\,. \tag{3.21}$$

Note that the total electromagnetic energy satisfies the condition $E_{\rm mag} = E^{\rm tor}_{\rm mag} + E^{\rm pol}_{\rm mag}$, since the electric field E^i provides a contribution to the energy, $E^iE_i = (v^iv_i)(B^iB_i - B^2_{\parallel})$, that is already included in the definitions (3.20) and (3.21).

Unless stated differently, we generally impose "bitant symmetry", i.e., a reflection symmetry with respect to the (x,y) plane. As a result, during the evolution the compact star is constrained to be centered at the origin of the coordinate system in the z direction, while it is allowed to move in the (x,y) plane. In order to monitor the relative motion of the rest-mass density distribution with respect to the coordinate system, we compute the first momentum of the rest-mass density distribution

$$X^i_{CM} = \frac{1}{\widetilde{M}}\int d^3x\;\rho\;x^i\,, \tag{3.22}$$

where $\widetilde{M} \equiv \int d^3x\;\rho$. These quantities are reminiscent of the Newtonian definition of the center of mass of the star but, because they are not gauge-invariant quantities, they are not expected to be constant during the evolution. However, since in a Newtonian framework a time-variation of one of the $X^i_{\rm CM}$ would signal a nonzero momentum in that direction, we monitor these quantities as a measure of the overall accuracy of the simulations. Of course, given the above-mentioned imposed symmetry, $z_{\rm CM}$ is supposed to be zero during the whole evolution.

For each of the simulations we report on this Thesis, we have performed a diagnostic analysis during the evolution, monitoring many of the quantities which we have defined in this Section. This is a fundamental step, which allows us to check for the presence of unexpected features or errors due to computational issues, or to wrong choices in the settings. In Fig. 3.4 an example of diagnostic analysis for one of the evolved magnetized models, namely `U11-1.0e14`, is shown. The three upper panels show the time evolution of the distortion parameters η_+ and η and of the instability parameter β. The red dot-dashed vertical lines mark the interval we selected for computing the growth-time of the instability $\tau_{\rm bar}$ and the frequency of the bar deformation $f_{\rm bar}$ by means of a nonlinear least-square fit, as shown in the two lower panels on the right. The results of this computations are reported in Tab. 5.1. In the other six

lower panels we report the total magnetic energy, the total rest-mass normalized to its initial value, the divergence of the magnetic field, the Hamiltonian constraint and the two components of the first momentum of the rest-mass density distribution on the (x, y) plane.

In the Appendix, we will show many other figures similar to this one, showing the dynamics of almost all `U11` magnetized models we evolved for the present work, both bar-stable and bar-unstable.

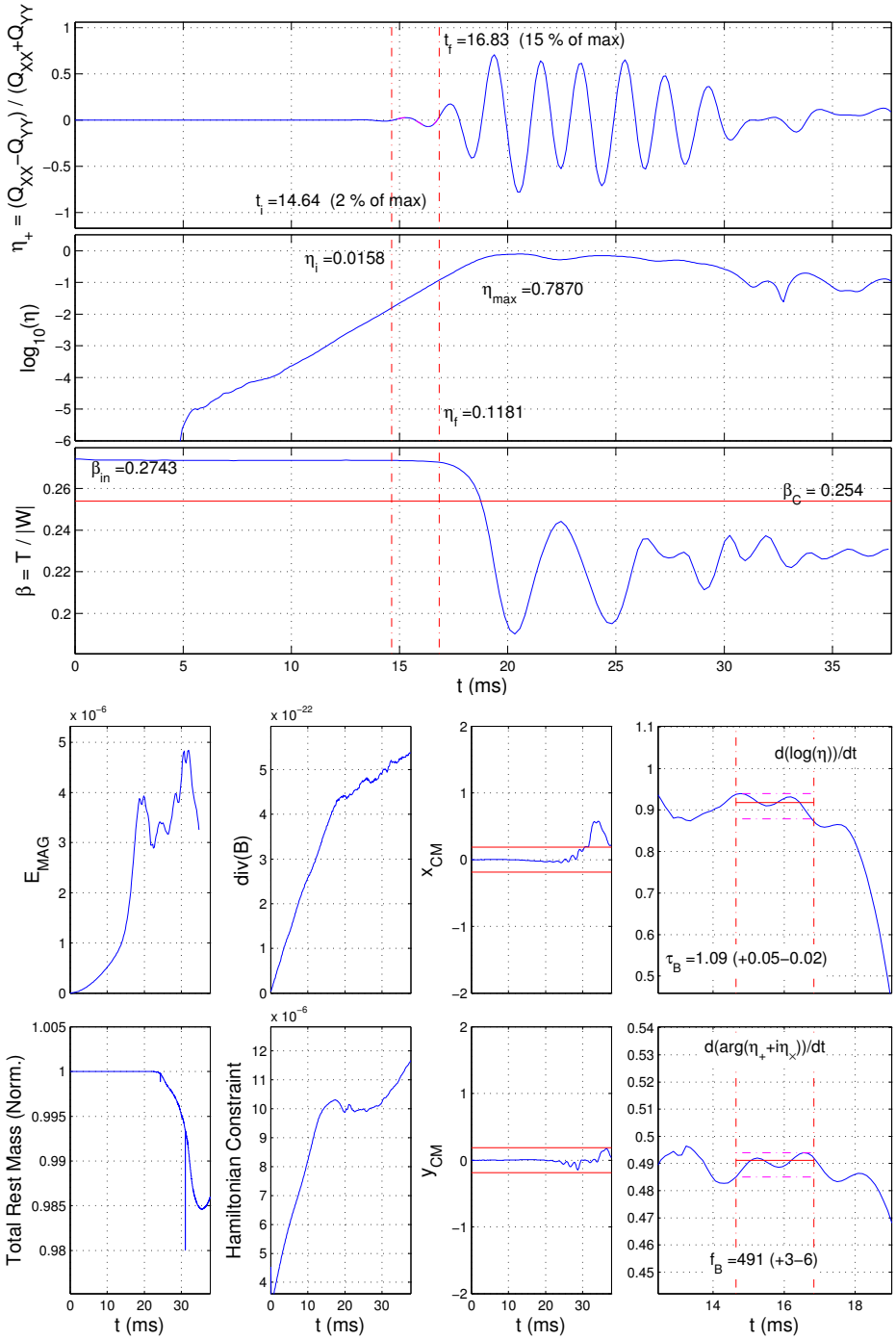

Figure 3.4: Example of diagnostic analysis for one of the evolved magnetized models, namely `U11-1.0e14`. The three upper panels show the time evolution of the distortion parameters η_+ and η and of the instability parameter β. The red dot-dashed vertical lines mark the interval we selected for the fits of the growth-time of the instability $\tau_{\rm bar}$ and of the frequency of the bar deformation $f_{\rm bar}$. In the other six lower panels we report the total magnetic energy, the total rest-mass normalized to its initial value, the divergence of the magnetic field, the Hamiltonian constraint and the two components of the first momentum of the rest-mass density distribution on the (x, y) plane.

Chapter 4

Evolution of bar-mode stable magnetized neutron star models

In this Chapter we will focus on illustrating how magnetic fields affect the dynamics of bar-mode *stable* models. Although these show a comparatively simpler evolution than unstable ones, they provide a number of interesting considerations, as we will see.

We recall that using the same EOS adopted here, Ref. [10] has determined the threshold for the development of a dynamical bar-mode instability to be $\beta_c \simeq 0.255$ (cf., Fig. 3.3). We have therefore considered a number of stable models, namely `S1`, `S6`, `S7` and `S8`, that are increasingly more distant from the threshold. We have then added to each model an initial poloidal magnetic field, all confined inside the star, with two different strengths, namely, $B^z_{\rm max}|_{t,z=0} = 1.0 \times 10^{15}$ G and $B^z_{\rm max}|_{t,z=0} = 1.0 \times 10^{16}$ G, and performed simulations to record the different impact of the magnetic fields on the dynamics.

4.1 General features of the dynamics of stable magnetized models

The above-mentioned models have been proved to be stable in the absence of magnetic fields (cf., [10]), so we expect them to remain stable also with the additional magnetic tension. However, while models with $B^z_{\rm max}|_{t,z=0} = 1.0 \times 10^{15}$ G do not show in their dynamics any significant deviation from a purely hydrodynamical evolution, models with $B^z_{\rm max}|_{t,z=0} = 1.0 \times 10^{16}$ G do quite the opposite. This is shown in Fig. 4.1, which reports the evolution of the rotation parameter β for all these stable models. Solid lines of different color refer to the different models but all having an initial magnetic field $B^z_{\rm max}|_{t,z=0} = 1.0 \times 10^{15}$ G. On the

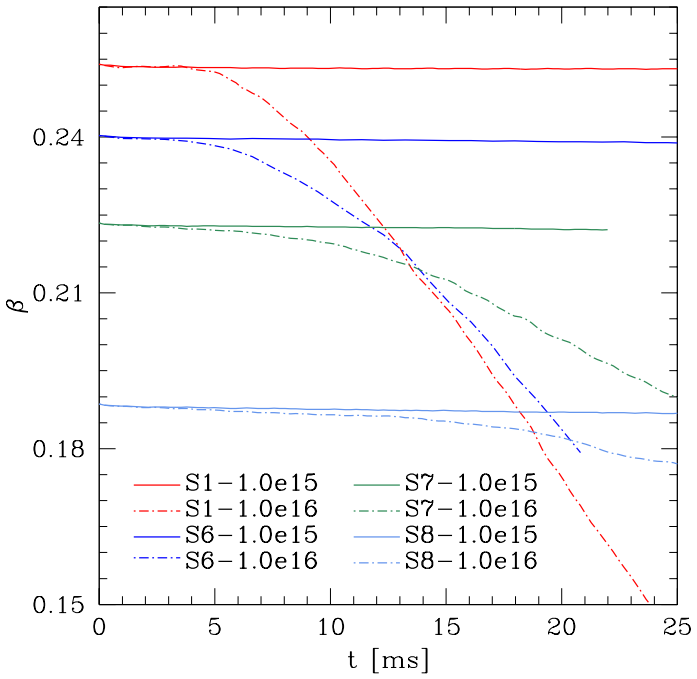

Figure 4.1: Evolution of the rotation parameter $\beta := T/|W|$ for models `S1`, `S6`, `S7` and `S8` which are stable against the bar-mode deformation in the unmagnetized case. The solid lines refer to models with $B^z_{\rm max}|_{t,z=0} = 10^{15}$ G, while the dash-dot lines to models with $B^z_{\rm max}|_{t,z=0} = 10^{16}$ G.

other hand, dot-dashed lines of different color refer to models with $B^z_{\rm max}|_{t,z=0} = 1.0 \times 10^{16}$G. Note that for comparatively "low" magnetic fields, the rotation parameter does not show any significant variation from the initial value over a timescale of around 25 ms, with changes that are $\lesssim 0.4\%$ for model `S1` and $\lesssim 1.0\%$ for model `S8`. On the other hand, for magnetic fields that are one order of magnitude larger, the rotation parameter changes significantly, decaying almost linearly with time. This is obviously due to the combined action of the differential rotation and of the magnetic winding, which increases the magnetic tension and drives the NS towards a configuration that is uniformly rotating. We note that the higher is the initial value of β, the steeper is its decrease during the evolution. A more detailed explanation of the mechanisms behind these changes as well as a more accurate description of the dynamics of the magnetic fields during the evolution will we given in Chap.6. In the next section, we will describe in detail the dynamics of model `S1`, which is the closest stable model to the threshold β_c and then seems to be the most sensitive to the effects of magnetic fields among the stable models we evolved.

4.2 Detailed dynamics of S1 magnetized models

What is discussed in general for all the stable models, can be better analyzed looking in detail at the structural changes for model S1 with the two different values of the initial magnetic field. In Fig. 4.2 we show two snapshots of the rest-mass density on the (x, y) plane for model S1-1.0e15 at the beginning and at the end of the evolution (i.e., 25 ms). Clearly, no major changes in the initial configuration can be appreciated for an initial poloidal magnetic field such as $B^z_{\rm max}|_{t,z=0} = 10^{15}$ G (and, accordingly, for weaker fields). The same conclusion is confirmed if we have a look at Fig. 4.4, showing a spacetime diagrams of the evolution of the rest-mass density (left panel) and of the angular velocity (right panel) along the x-axis for the same model, and Fig. 4.6, directly comparing the initial and final profiles of the same two quantities: the angular velocity and rest-mass density in the stellar core hardly change. The only difference we observe is an increase of about 20% in the rest-mass density in the central region, with the star maintaining a toroidal, albeit only slightly, shape. The envelope surrounding the star in Fig. 4.4 represents and extended, very low-density outer mantle containing only a very small amount of matter, since in that region $\rho \lesssim 10^{-6}\,\rho_c$. This is the reason why such a feature is not visible at all in Fig. 4.2, where the lower limit of the color code has been set at about $\rho \sim 10^{-4}\,\rho_c$, to provide a clear and not misleading qualitative picture of the global evolution.

This is to be contrasted with Fig. 4.3 for model S1-1.0e16, where snapshots of the rest-mass density are shown at regular intervals of 5 milliseconds during the whole evolution (the initial configuration is of course identical to the one of model S1-1.0e15 in Fig. 4.2). Here, after 10 ms of evolution, quite a significant change in the stellar structure is already evident: the rest-mass density in the inner regions of the star has increased while it has correspondingly decreased in the outer ones, which have expanded. At later times, the central rest-mass density keeps growing, with the outer envelope expanding beyond the boundaries of the finest grid. A more detailed description of the structural changes due to the presence of a very strong magnetic field can be achieved by looking at the spacetime diagrams of Fig. 4.5 and the profiles of Fig. 4.7. Regarding the evolution of the rest-mass density, we have a clear confirmation of what has just been described talking about Fig. 4.3 and we can easily quantify the increase in its central value: after 10 ms of evolution the central density is already twice the initial value while at the end of the evolution, meaning after 25 ms, its value is about 2.4 times the initial one. The angular velocity profile, instead, shows a more varied evolution, with changes mainly concerning the central region (the one where the increase of the rest-mass density occurs). In

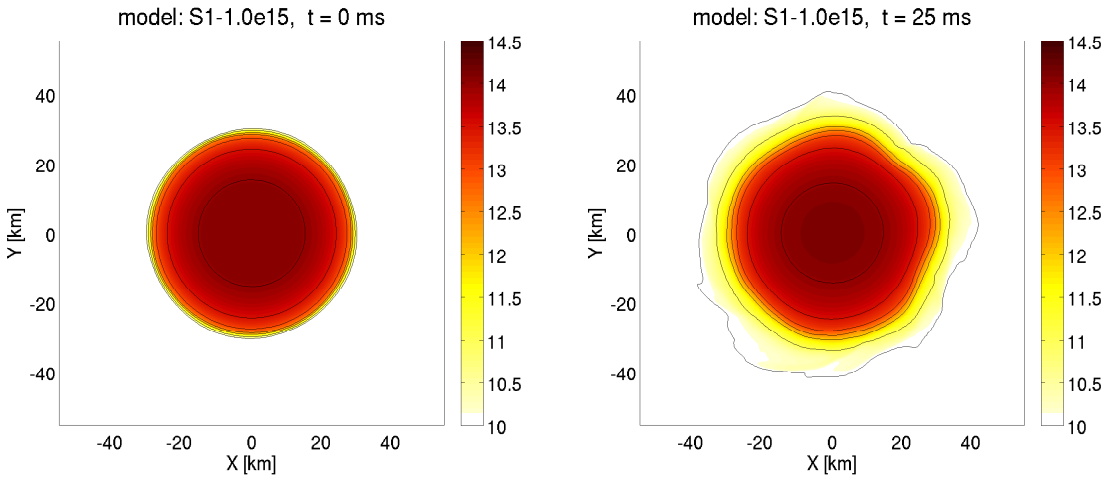

Figure 4.2: Snapshots of the rest-mass density on the (x, y) plane for model `S1-1.0e15` at the beginning and at the end of the evolution, namely $t = 0$ and 25 ms. The color code is defined in terms of $\log_{10}(\rho)$, where ρ is in cgs units (g cm^{-3}). Additionally, isodensity contours are shown for $\rho = 10^{11}$, 10^{12}, 5×10^{12}, 10^{13}, 5×10^{13} and 10^{14} g cm^{-3}.

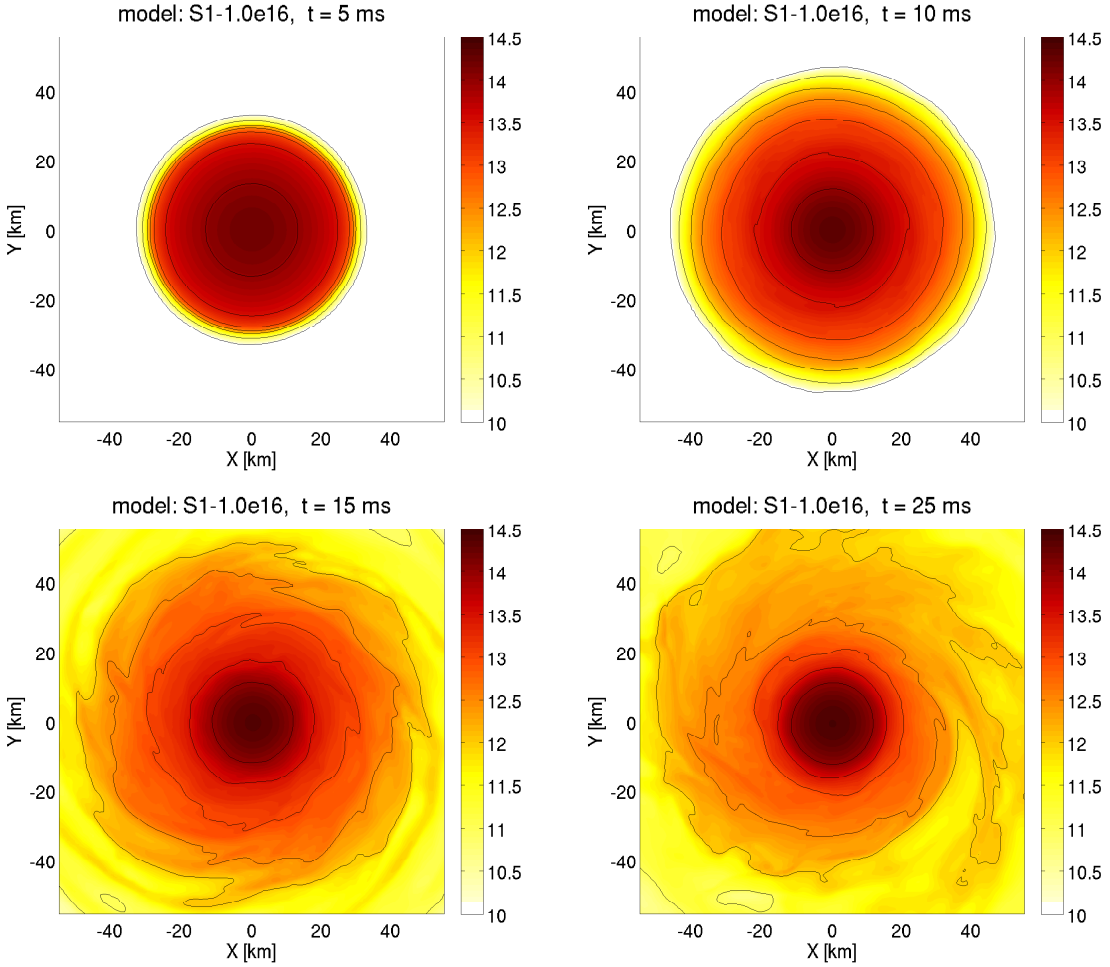

Figure 4.3: Same as Fig. 4.2 but for model `S1-1.0e16` at different times during the evolution, namely $t = 5$, 10, 15 and 25 ms.

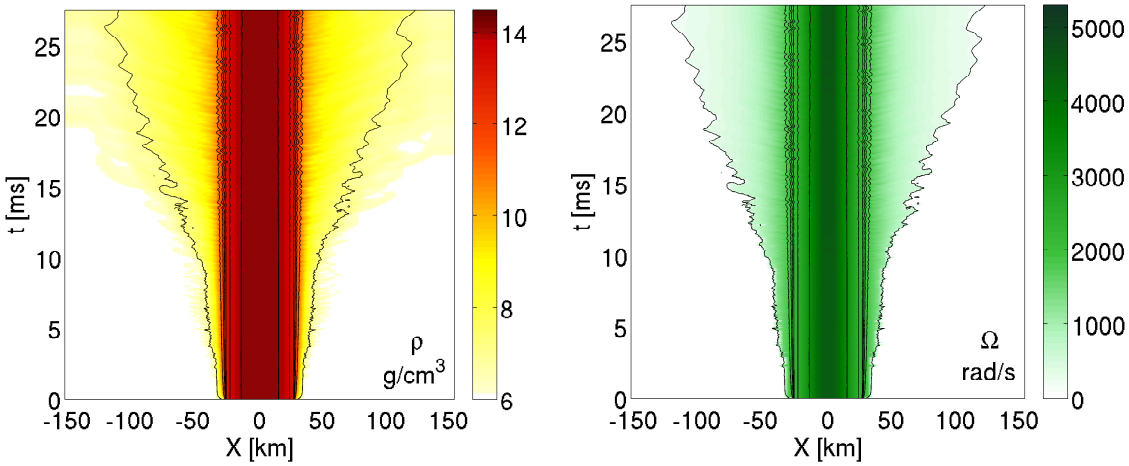

Figure 4.4: Spacetime diagrams of the evolution of the rest-mass density (left panel) and of the angular velocity (right panel) along the x-axis for models `S1-1.0e15`. The color code for the rest-mass density is defined in terms of $\log_{10}(\rho)$, where ρ is in cgs units (g cm^{-3}). In addition, both diagrams also report isodensity contours of the rest-mass density for $\rho = 10^6,\ 10^{11},\ 10^{12},\ 5 \times 10^{12},\ 10^{13},\ 5 \times 10^{13}$ and 10^{14} g cm^{-3}.

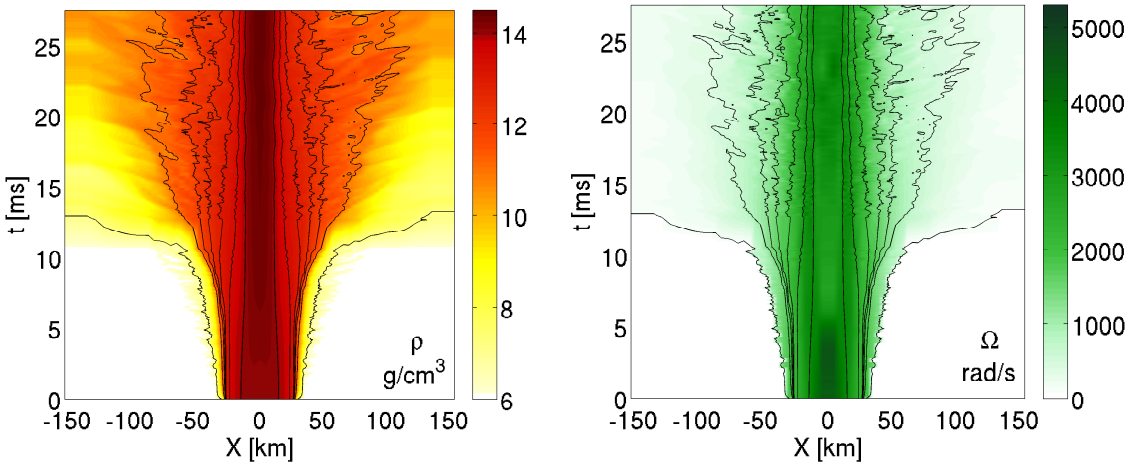

Figure 4.5: Same as Fig. 4.4 but for model `S1-1.0e16`.

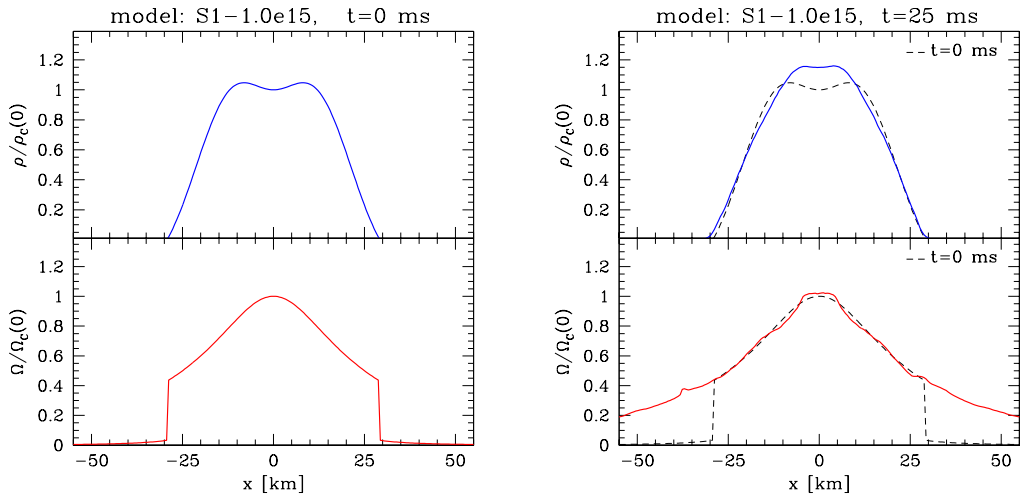

Figure 4.6: Initial ($t = 0$ ms, left panels) and final ($t = 25$ ms, right panels) profiles of the rest-mass density ρ (blue lines) and of the angular velocity Ω (red lines) along the x-direction, normalized to their initial central values, for model `S1-1.0e15`.

the first milliseconds of the evolution the angular velocity increases at the center, so the inner core of the neutron star accelerates its rotation. Then it rapidly decreases, reaching almost zero values, before settling to a constant value. We can briefly summarize the situation by saying that at the end of the evolution the angular velocity profile has flattened considerably and indeed the star has settled into a more compact configuration which is essentially axisymmetric and in uniform rotation within a coordinate radius of $\simeq 15$ km, surrounded by a very-low density envelope.

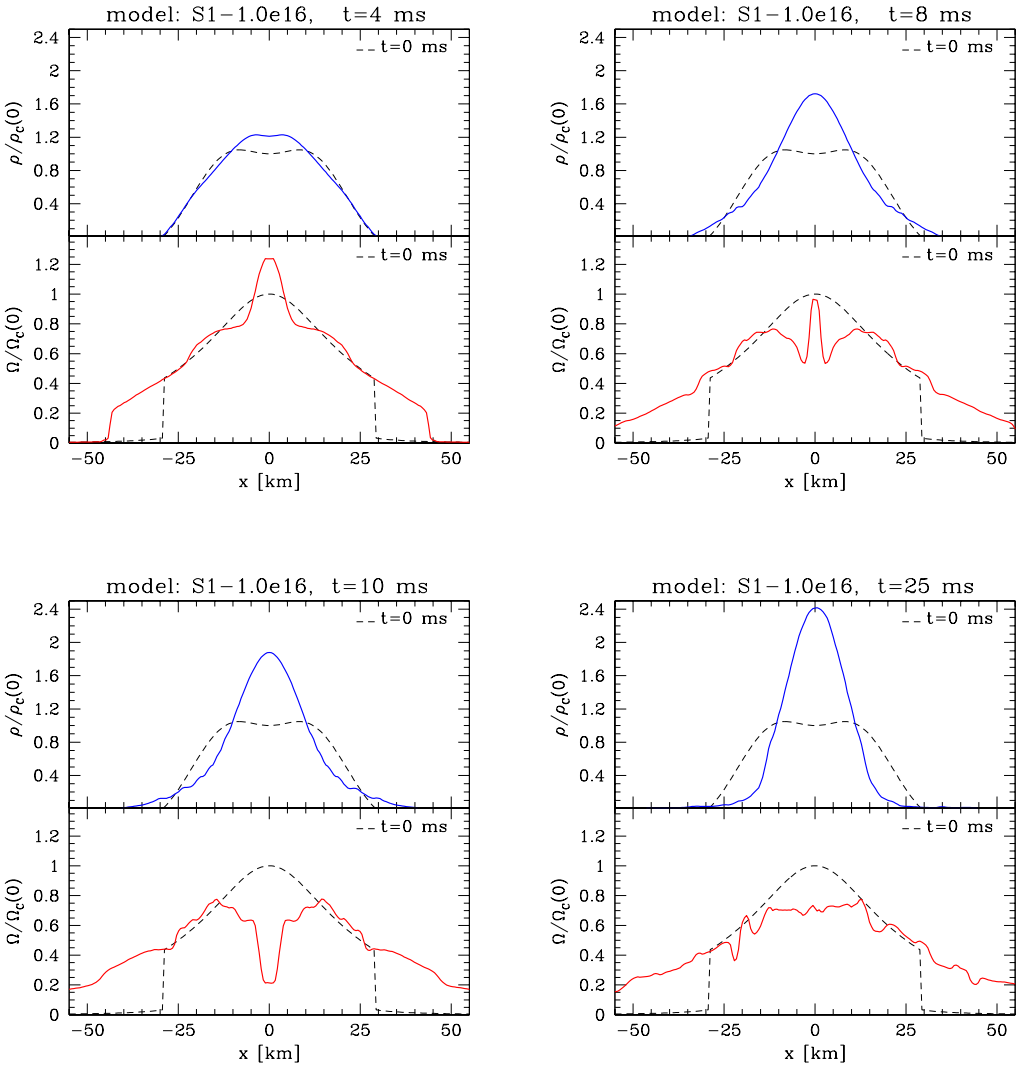

Figure 4.7: Same as Fig.4.6 but for model `S1-1.0e16` at four different times during the evolution, namely $t = 4$, 8, 10 and 25 ms. The initial profiles are also drawn with black dotted lines in the all panels.

4. EVOLUTION OF BAR-MODE STABLE MAGNETIZED NEUTRON STAR MODELS

Chapter 5

Dynamical bar-mode instability in magnetized and rotating relativistic stars

In this Chapter we discuss in detail the results relative to models that are bar-unstable in the unmagnetized case and describe what are the changes in the dynamics when an initial poloidal magnetic field is added as a perturbation to the initial matter equilibrium configuration.

5.1 General features of the dynamics of models that are bar-mode unstable in the unmagnetized case

The main aim of this study is to accurately study and quantify the effects of magnetic field on the onset and development of the bar-mode instability in NSs. In order to obtain an extensive analysis of this subject, we selected three representative classes of initial models, namely `U3`, `U11` and `U13`, all belonging to the same sequence of constant rest-mass $M_0 = 1.5\,M_\odot$ as the stable models already studied in the Chap. 4. These models are all bar-unstable at zero magnetization, having different values of the rotation parameter β that lie above the threshold for the onset of the instability, and cover the whole range of interest. We recall here that, as stated in Sec. 1.2, simulations of magnetized models in the Newtonian case has shown that for very high magnetic field strengths the instability is completely suppressed, and so we expect a similar behavior in full general relativity as well) For each of these models, we ran about ten simulations with different magnetic fields ranging from 1.0×10^{14} to 1.0×10^{16} G, in order

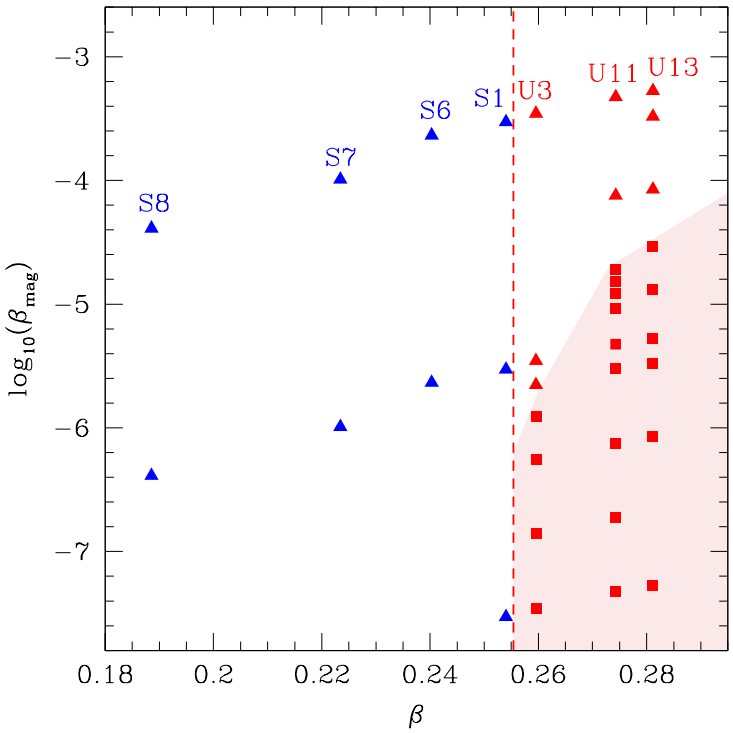

Figure 5.1: Qualitative summary of the results of all our simulations in the $(\beta, \beta_{\rm mag})$ parameter space which was previously shown in Fig. 3.3. The vertical red dashed line marks the stability threshold for zero magnetic fields. The red-shaded area collects models that turned out to be bar-mode unstable: hence, red squares refer to initial models that still develop a bar deformation, while red triangles refer to potentially bar-unstable models that are stabilized by the presence of strong magnetic fields.

to observe the effects of the magnetization on the onset and development of the dynamical bar-mode instability and to determine an approximate threshold for its suppression The reason we chose this range of values for the magnetic field is that magnetic fields below 1.0×10^{14} G, which corresponds to $\beta_{\rm mag} \sim 5 \times 10^{-8}$, are too weak to have detectable effects on the dynamics while fields above 1.0×10^{16} G ($\beta_{\rm mag} \gtrsim 5 \times 10^{-4}$) are too strong to be considered as a perturbation to the initial equilibrium model. Fig. 5.1 shows a qualitative but exhaustive summary of the results of all our simulations in the $(\beta, \beta_{\rm mag})$ diagram, where β is the rotation parameter and $\beta_{\rm mag}$ represents the magnetization. Here, blue and red symbols mark models that are respectively bar-mode stable and bar-mode unstable at zero magnetizations, while the vertical red dashed line marks the stability threshold for zero magnetic fields $\beta_c = 0.2554$. The red-shaded area collects models that the evolutions reveal to be bar-mode unstable: hence, red squares refer to initial models that still develop a bar-mode instability, while red triangles

refer to potentially bar-unstable models that are stabilized by the presence of strong magnetic fields. We can then easily identify an approximate threshold for the complete suppression of the dynamical bar-mode instability due to the magnetization around $2 \times 10^{-6} \lesssim \beta_{\rm mag} \lesssim 8 \times 10^{-5}$, which corresponds to initial magnetic fields strengths in the range $8 \times 10^{14} \lesssim B^z_{\rm max}|_{t,z=0} \lesssim 4 \times 10^{15}$ G and whose exact value is different for the different initial models. These threshold values, as well as a quantitative description of the effects of magnetic fields even for models below this threshold, will be reported in the following Sections of this Chapter.

5.2 Detailed dynamics of U11 magnetized models

A deep and detailed analysis of the dynamics of bar-unstable models have been performed, starting with model U11. For this model the rotation parameter has an initial value $\beta_{\rm U11} = 0.2743$, which is intermediate between the instability threshold $\beta_c \sim 0.255$ and the rotation parameter of the most unstable model $\beta_{\rm U13} = 0.2812$. Since this model is neither slightly nor largely overcritical, its dynamics are very clear and allow us to show a full qualitative and quantitative picture of what happens as the bar-mode instability develops. We will initially focus our attention on models U11-1.0e14, U11-2.0e15, U11-4.0e15 and U11-1.0e16, which, as discussed before, have initial poloidal magnetic field such that $B^z_{\rm max}|_{t,z=0}$ is equal to 1.0×10^{14}, 2.0×10^{15}, 4×10^{15} and 1.0×10^{16} G, respectively.

The different qualitative behavior of these four magnetized models can be described by showing in Fig. 5.2, 5.3, 5.4 and 5.5 a few snapshots of the rest-mass density ρ on the (x, y) plane at different times during the evolution.

In particular, Fig. 5.2 refers to model U11-1.0e14 and show the dynamics of this model at six different times during the evolution, namely $t = 10$, 15, 20, 25, 30 and 35 ms. This model clearly turns out to be still bar-mode unstable, as its unmagnetized counterpart. After 15 ms we can already observe a small deformation with respect to the initial axisymmetric configuration, which is then amplified until a bar is fully formed at 20 milliseconds. Later, we start appreciating the development of spiral arms, which are responsible for ejecting a small amount of matter and for a progressive attenuation of the bar extension until a an almost axisymmetric configuration is reached at the end of the simulation.

A similar evolution is shown in Fig. 5.3, which refers to model U11-2.0e15 at the same times during the evolution. As well as U11-1.0e14, this model is still bar-unstable, but a few differences are evident. The bar deformation starts to develop at a slightly later times and

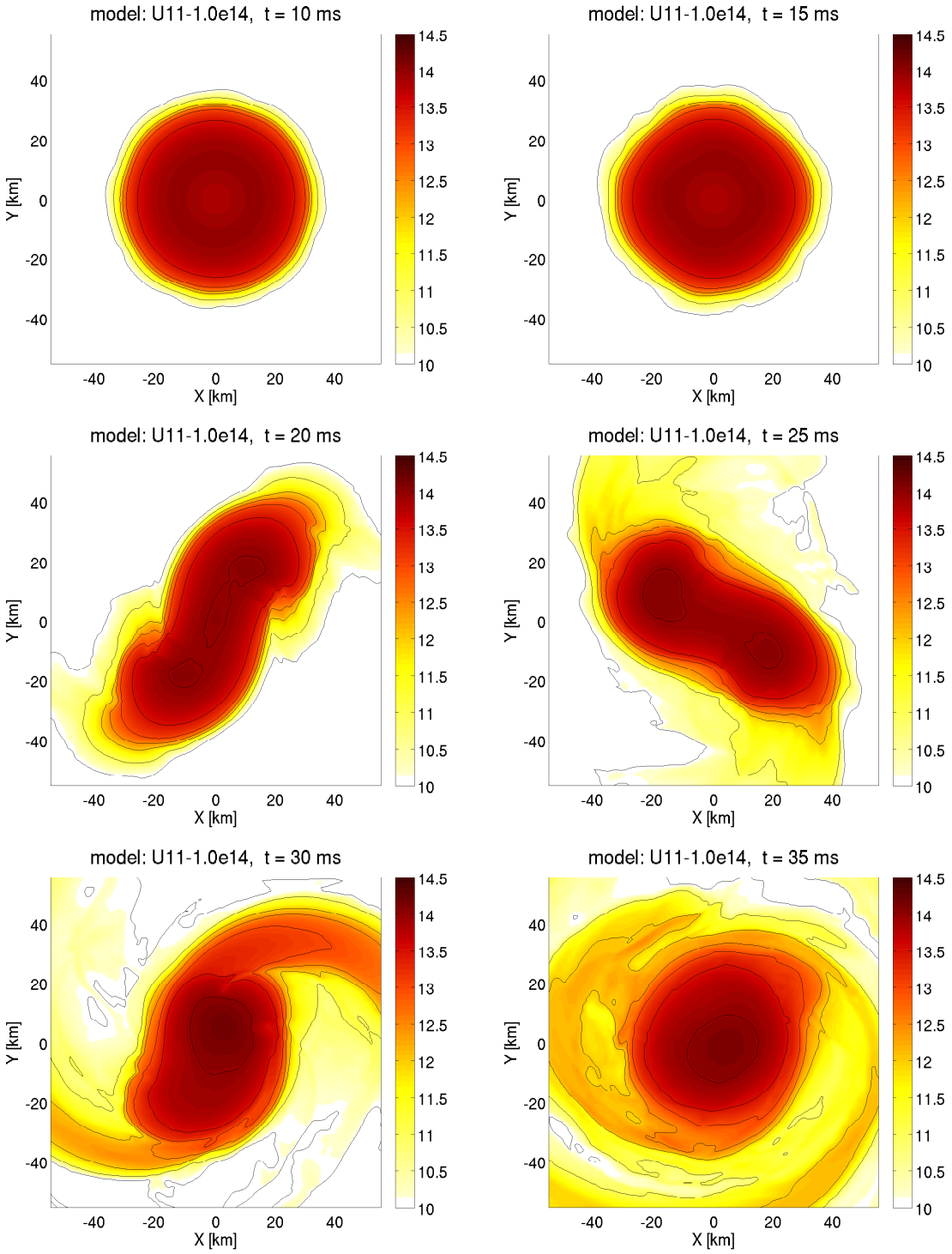

Figure 5.2: Snapshots of the rest-mass density on the (x, y) plane for model `U11-1.0e14` at different times during the evolution, namely, $t = 10$, 15, 20, 25, 30 and 35 ms. The color code is defined in terms of $\log_{10}(\rho)$, where ρ is in cgs units (g cm^{-3}). Additionally, isodensity contours are shown for $\rho = 10^{11}$, 10^{12}, 5×10^{12}, 10^{13}, 5×10^{13} and 10^{14} g cm^{-3}.

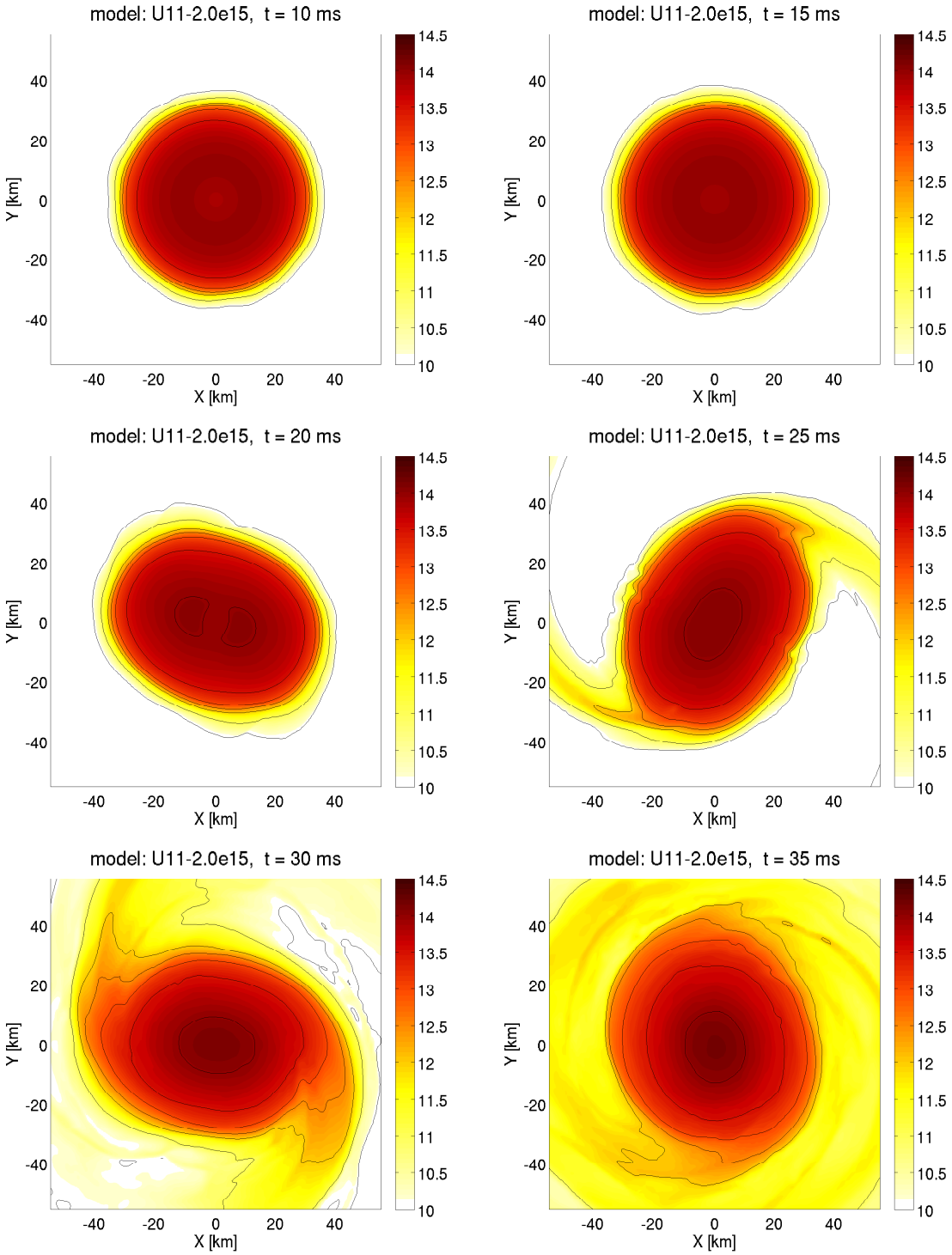

Figure 5.3: Same as Fig. 5.2 but for model `U11-2.0e15` at different times during the evolution, namely, $t = 10$, 15, 20, 25, 30 and 35 ms.

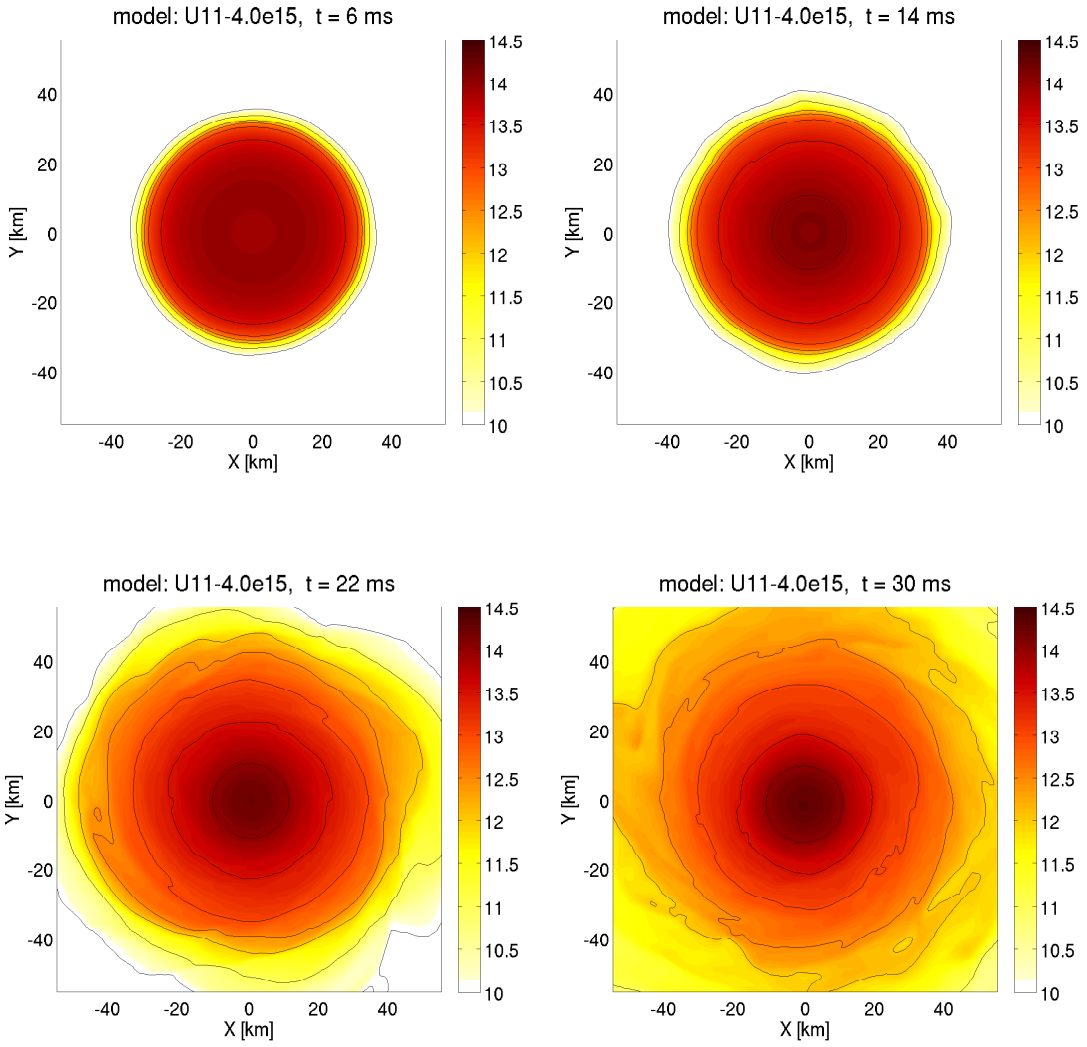

Figure 5.4: Same as Fig. 5.2 but for model `U11-4.0e15` at different times during the evolution, namely, $t = 6$, 14, 22 and 30 ms.

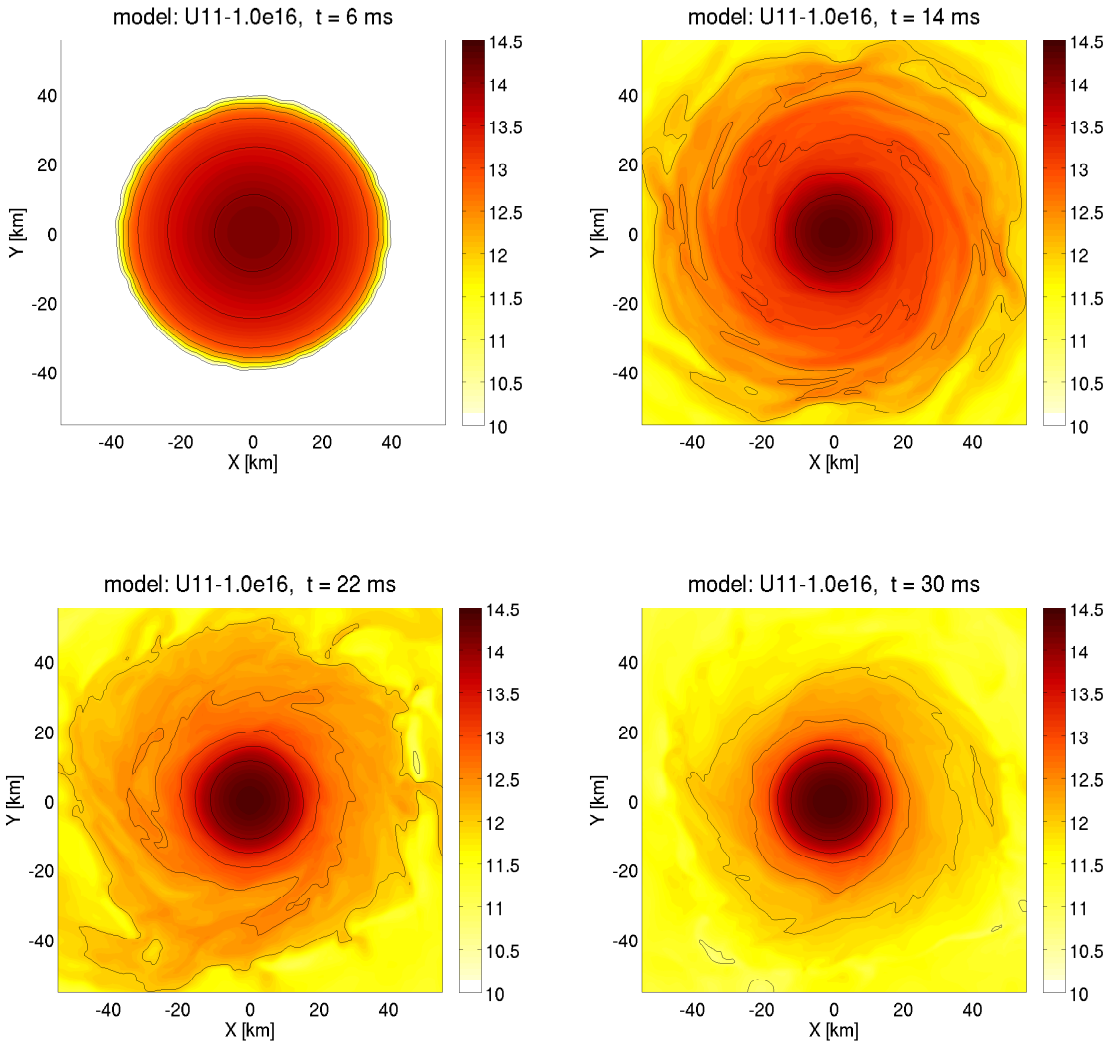

Figure 5.5: Same as Fig. 5.2 but for model `U11-1.0e16` at different times during the evolution, namely, $t = 6$, 14, 22 and 30 ms.

it takes a little more time to grow. Besides, the maximum distortion is clearly smaller and the spiral arms are less pronounced.

A different situation in shown in Fig. 5.4 for the evolution of model `U11-4.0e15`, which appears to be stable against bar-mode deformations due to the presence of the strong magnetic field. In this case, after around 15 ms the density profile has already changed, turning from an initial toroidal profile (cf., Fig. 3.1) to an oblate profile with its maximum residing on the z-axis. Later in the evolution, we observe an increase in the central density and the outer layers expanding well beyond the borders of the finest grid, but always preserving an axisymmetric configuration.

Finally, in Fig. 5.5 we show snapshots of the density for model `U11-1.0e16`, the most magnetized model we evolved. Even this model turn out to be stable and shows a similar behavior to the previous model. The only important difference is the larger increase of the central rest-mass density and the more significant expansion of the outer layers of the star. Indeed, after the first 15 ms of evolution, matter has been shed already beyond the edges of the finest grid.

Even if snapshots are the fastest way to identify the presence of a bar deformation and the development of the bar-mode instability, the distortion parameters (3.15) represent a more useful tool to detect and quantify such deformation, as we mentioned in Sec. 3.3. In Fig. 5.6 we show the evolution of the distortion parameters η_+ (top panel) and η (bottom panel) for these models. In the least magnetized model (i.e., `U11-1.0e14`), η_+ starts oscillating after about 10 ms of evolution with an amplitude that almost reaches unity, and it keeps oscillating for about 20 ms. At the same time, η undergoes an exponential growth, increasing its value by about three orders of magnitude until it reaches a saturation level, which persists for about 10 ms and then decays. This is exactly the behavior we expect from a stellar model which is unstable against the dynamical bar-mode instability, as model `U11` is known to be in the unmagnetized case (cf., Sec. 1.2 and, for further details, Refs. [10, 111]).

However, when the initial poloidal magnetic field is two orders of magnitude stronger (i.e., as for model `U11-1.0e16`), the dynamics shows a very different behavior. The amplitude of the oscillations in η_+ is negligible and η does not grow exponentially, being two orders of magnitude lower than it is for model `U11-1.0e14` during the whole evolution. This indicates that although the model is unstable in the absence of magnetic fields, no bar-mode deformation develops in this case over a timescale of ~ 35 ms of evolution and for this magnetic-field strength.

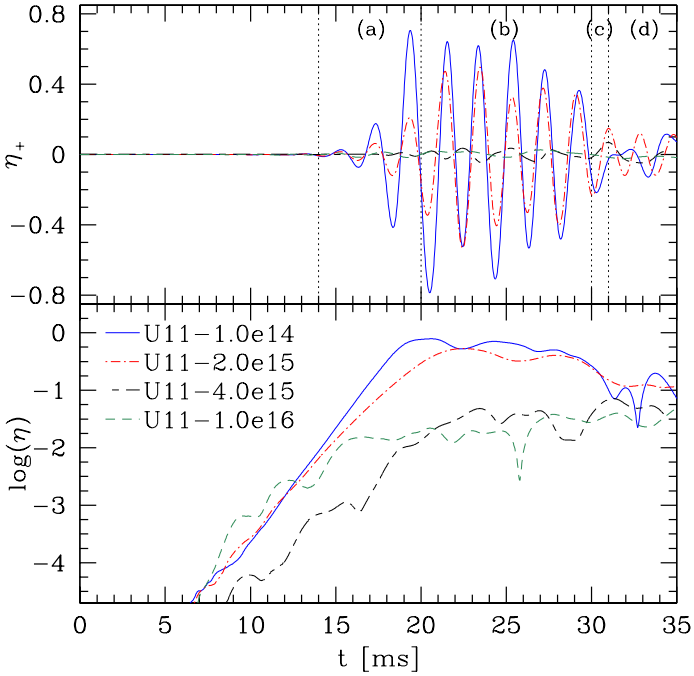

Figure 5.6: Evolution of the distortion parameters η_+ (top panel) and η (bottom panel) for model `U11` with different values of the initial poloidal magnetic field: `U11-1.0e14` (the least magnetized model among the ones we evolved), `U11-2.0e15` (the last bar-unstable model in a scale of increasing magnetization), `U11-4.0e15` (the first stable model) and `U11-1.0e16` (the most magnetized model). The dotted vertical lines in the top panel mark the four main phases of the evolution of the bar-mode instability (cf., Sec. 1.2).

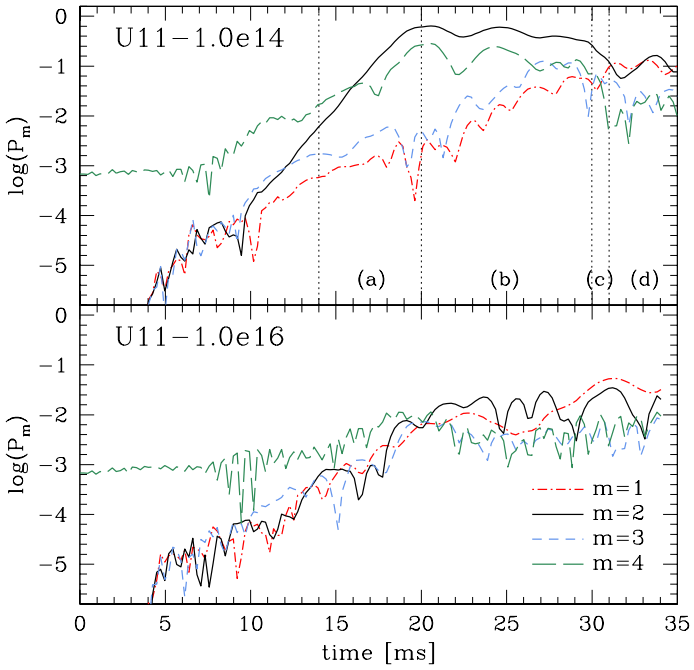

Figure 5.7: Comparison of the power in the Fourier modes $m = 1$, 2, 3 and 4 (cf. Eq. (3.18)) for the bar-unstable model `U11-1.0e14` (top panel) and for the bar-stable model `U11-1.0e16` (bottom panel). The dotted vertical lines in the top panel mark the four main phases of the evolution of the bar-mode instability (cf., Sec. 1.2).

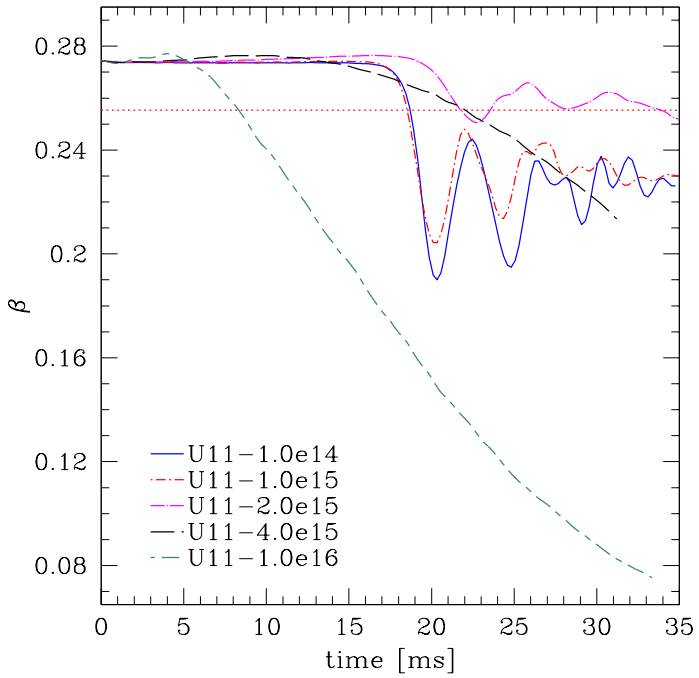

Figure 5.8: Evolution of the rotation parameter $\beta := T/|W|$ for `U11` models with five different values of the initial poloidal magnetic field between 10^{14} and 10^{16} G, three of which are still unstable (`U11-1.0e14`, `U11-1.0e15`, `U11-2.0e15`) while the other are stable due to magnetization (`U11-4.0e15` and `U11-1.0e16`).

For intermediate initial poloidal magnetic fields, we find a significant change in the dynamics by simply varying the field strength by a factor of two, which corresponds to a change of a factor of four in the magnetic energy. Moreover, in model `U11-2.0e15` the bar-mode instability still develops, even though it takes a little longer to grow, while model `U11-4.0e15` is stable and the bar-mode instability is suppressed, since η does not show an exponential growth. As a result, we can bracket the stability threshold for the development of the bar-mode instability between these two models in the presence of strong magnetic fields (cf., Fig. 5.1). An important way to describe the dynamics of the bar-mode instability is represented by the decomposition of the rest-mass density in its Fourier modes (3.18) and their evolution, as discussed in Chap. 3.3. In Fig. 5.7 we report the power P_m in the first four m-modes for model `U11-1.0e14` (top panel) and model `U11-1.0e16` (bottom panel). Relating the evolution of these quantities to the changes in the deformation of the star η_+ allows us to provide a deeper and consistent description of the different stages of the instability. First of all, we have to note that at the beginning of both simulations the $m = 4$ mode has the largest power, as a result of the Cartesian discretization. While this can be reduced by increasing the resolution, the $m = 4$

deformation plays no major role in the development of the instability. The initial phase of the instability [stage (a) in Fig. 5.6 and 5.7] is clearly characterized by the exponential growth of the $m = 2$ mode. At the same time, but to a lesser extent, we also observe a growth of the $m = 3$ mode and of the $m = 1$ mode. A first mode coupling takes place when the $m = 4$ mode reaches the $m = 2$ mode at about 15 ms, which is the time when collective phenomena start to be fully visible and the distortion parameter starts to be appreciably different from zero (cf., Fig. 5.6 and 5.2). Soon after, the $m = 3$ and the $m = 1$ mode stop their growth for a few milliseconds while the $m = 2$ mode reaches its maximum power and the bar reaches its largest extension. During the following phase [stage (b)] the $m = 3$ and the $m = 1$ suddenly return to grow with the same growth rate and the bar-mode instability has reached a nonlinear saturation. Later in the evolution [stage (c)] modes m=1, 3 and 4 reach comparable powers and this marks the time when the bar deformation has a sudden decrease. As a result of this crossing among the three modes, only the m=1 mode will continue to grow, while the m=3 and the m=4 modes are progressively damped. The final phase [stage (d)] starts when the m=1 mode reaches a power amplitude comparable with those of the m=4 mode and the final mode-amplitude crossing takes place. At this point we observe a clear loss of the bar deformation and the emergence of an almost axisymmetric configuration. Another important quantity we can look at to appreciate the changes in the evolution due to different values of the initial magnetization is the the rotation parameter β. Fig. 5.8 shows its time evolution for the same four models we have already mentioned talking about Fig. 5.6 plus model `U11-1.0e15`. We recall here once again that the definitions of quantities such β are meaningful only in the case of stationary axisymmetric configurations and should be treated with care once the rotational symmetry is lost, therefore looking at its evolution during the unstable phase is not so meaningful. Anyway, keeping this in mind, we can still extract a qualitative behavior of the dynamics from this quantity and a clear comparison between differently magnetized models. First of all, we can see that for model `U11-1.0e14` the rotation parameter β is almost constant during the first stage of the evolution (up to $\sim 15 - 17$ ms) during which the model is still axisymmetric. When the bar deformation starts to develop and the distortion parameters reach a greater value than about 1%, it suddenly decreases and then oscillates until it seems to settle to a value below the instability threshold, since a new almost axisymmetric configuration has been reached after the attenuation of the bar deformation. Model `U11-2.0e15`, which is still bar-unstable despite the magnetization, shows a similar behavior, with the oscillations having a much smaller amplitude. Model `U11-4.0e15`, on the contrary, is stabilized by the presence of the magnetic

field and in this case β decreases slowly after the onset of the instability. The most magnetized model, `U11-1.0e16`, shows a quite different behavior since the rotation parameter starts decreasing very early in the evolution (after about 5 ms), falling below the instability threshold before 10 ms and then it keeps decreasing considerably. Finally, we describe the time evolution of β for model `U11-1.0e15`, which has an intermediate magnetization. This case is very similar to model `U11-1.0e14`, even if the differ by an order of magnitude in the magnetic field (and by two orders of magnitude in the magnetization $\beta_{\rm mag}$), showing that the effects of initial magnetic fields up to about 10^{15} G are almost negligible for model `U11`. On the contrary, the time evolution of β for model `U11-1.0e15` is much different from the one for model `U11-2.0e15`, even if their magnetizations differ only by a factor of 2, since the latter is quite close to the threshold for the suppression of the instability due to magnetic fields and their effects on the dynamics are quite strong.

A deeper insight in the matter dynamics of the differently magnetized models discussed above can be obtained by means of the spacetime diagrams shown in Fig. 5.9, 5.10 and 5.11, and that are reminiscent of similar ones first presented in Ref. [28]. In particular, Fig. 5.9 shows the rest-mass density profile along the x-axis for the four `U11` models using both a colormap (see the right-edge of the different panels) and some representative contour lines; note that the colorcode and the color ranges are the same in the four cases. It is worth mentioning that the low-magnetic-field model `U11-1.0e14` (upper-left panel) shows the evolution we expect from a bar-mode unstable model, since the bar deformation is clearly visible after about 20 ms. Model `U11-2.0e15` (upper-right panel) is unstable as well, even though the bar deformation is not as broad as in the previous case. The highly magnetized model `U11-4.0e15` (lower-left panel), on the other hand, shows no bar deformation and exhibits instead a transition from a toroidal configuration to an oblate one as is evident in Fig. 5.4. In addition, a small amount of matter is shed on the equatorial plane after about 15 ms of evolution. Finally, for the very highly magnetized model `U11-1.0e16` (lower-right panel), the expansion of the outer layers is much more rapid and the stellar material reaches a size of about 100 km (not shown in the figure), which is almost twice as large as for model `U11-4.0e15`. The ejected material creates an extended and flattened envelope of high-density matter[1], with rest-mass densities as high as 10^{12} g cm^{-3}.

[1]It is tempting and sometimes encountered in the literature to refer to the envelope as "disk" or "torus"; however, we find this is very misleading as the envelope is not disjoint from the star but rather an integral part of it which should not be discussed separately.

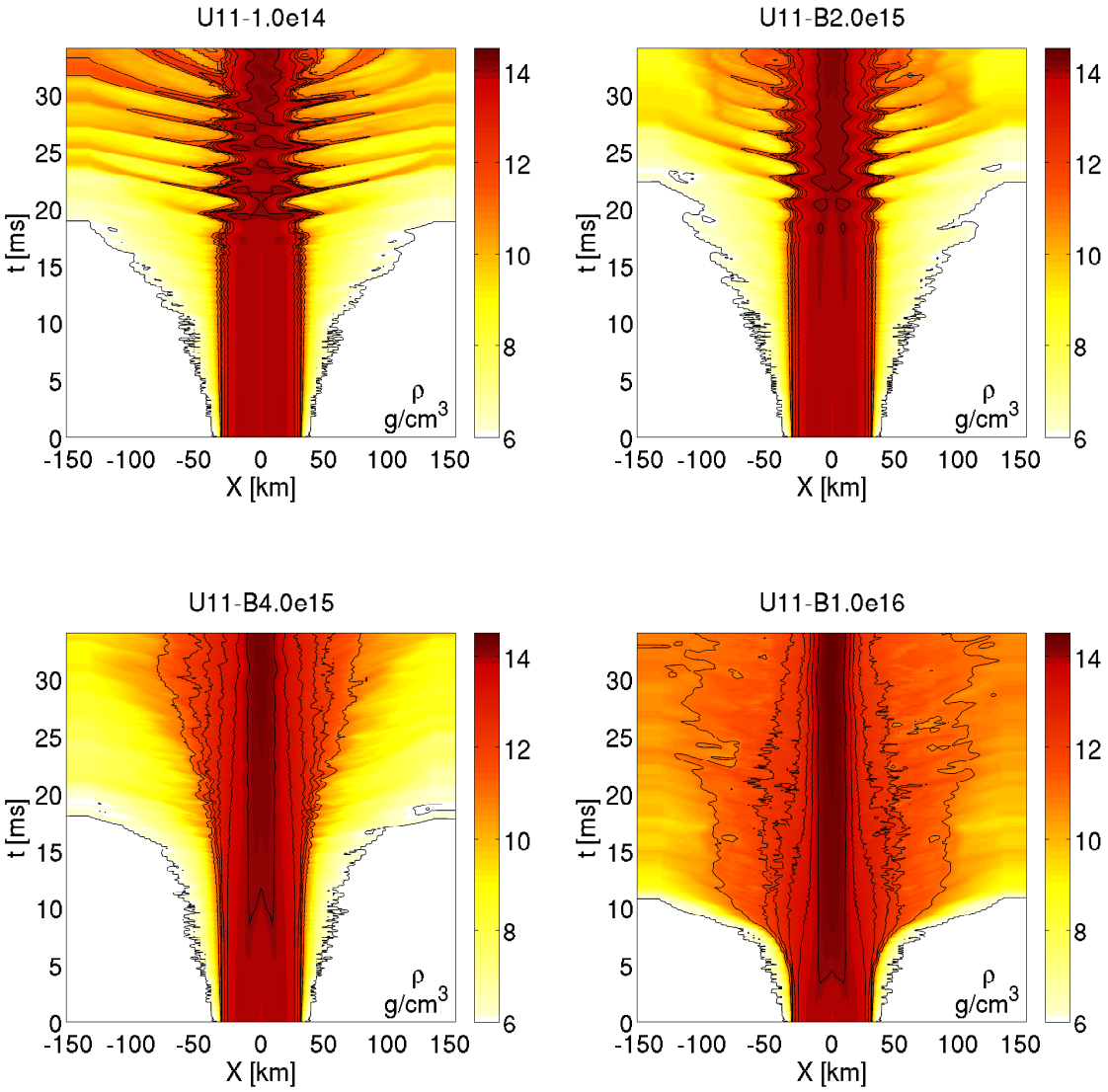

Figure 5.9: Spacetime diagrams of the evolution of the rest-mass density along the x-axis for models `U11-1.0e14` (upper-left panel), `U11-2.0e15` (upper-right panel), `U11-4.0e15` (lower-left panel) and `U11-1.0e16` (lower-right panel). The color code is defined in terms of $\log_{10}(\rho)$, where ρ is in cgs units (g cm^{-3}). In addition, all diagrams also report isodensity contours of the rest-mass density for $\rho = 10^{6},\ 10^{11},\ 10^{12},\ 5\times10^{12},\ 10^{13},\ 5\times10^{13}$ and 10^{14} g cm^{-3}.

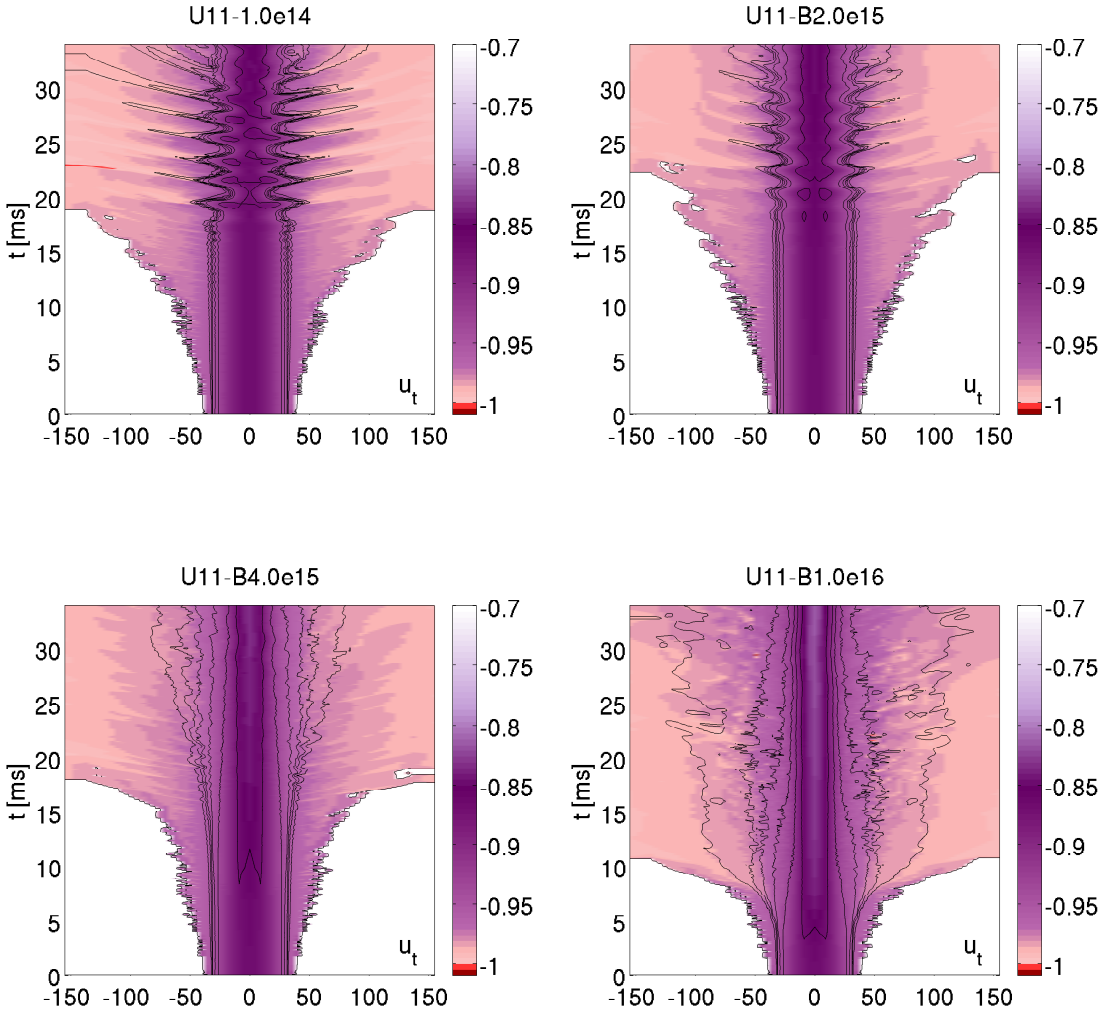

Figure 5.10: Spacetime diagrams of the evolution of the time-component of the fluid four-velocity along the x-axis for models `U11-1.0e14` (upper-left panel), `U11-2.0e15` (upper-right panel), `U11-4.0e15` (lower-left panel) and `U11-1.0e16` (lower-right panel). In addition, all diagrams also report isodensity contours of the rest-mass density for $\rho = 10^6,\ 10^{11},\ 10^{12},\ 5\times 10^{12},\ 10^{13},\ 5\times 10^{13}$ and 10^{14} g cm^{-3}.

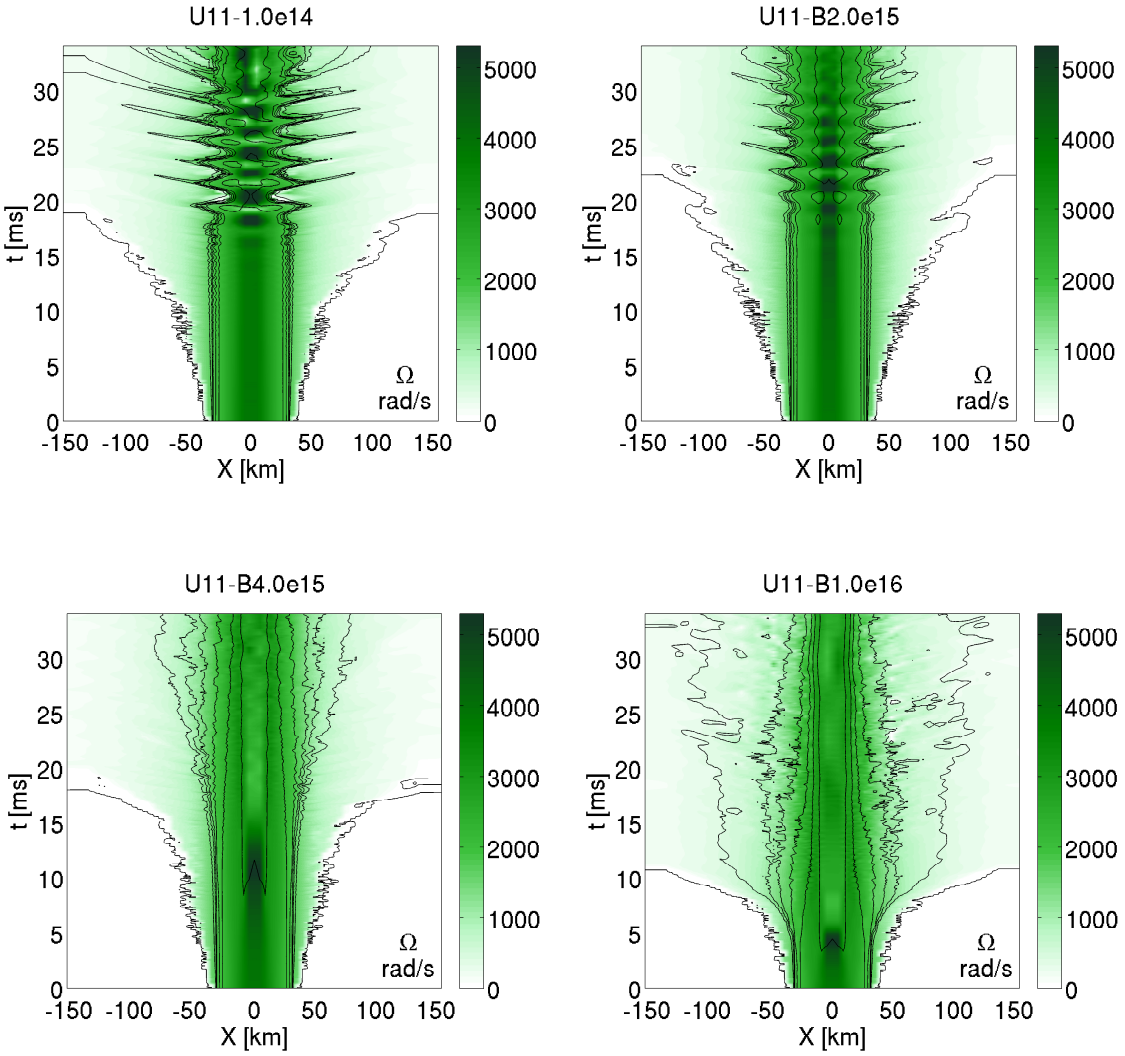

Figure 5.11: Spacetime diagrams of the evolution of the angular velocity along the x-axis for models `U11-1.0e14` (upper-left panel), `U11-2.0e15` (upper-right panel), `U11-4.0e15` (lower-left panel) and `U11-1.0e16` (lower-right panel). In addition, all diagrams also report isodensity contours of the rest-mass density for $\rho = 10^{6},\ 10^{11},\ 10^{12},\ 5\times10^{12},\ 10^{13},\ 5\times10^{13}$ and 10^{14} g cm^{-3}.

To determine whether the ejected matter is gravitationally bound or not, we look at the time component of the fluid four-velocity u_t (Fig. 5.10) since the local condition $u_t > -1$ provides a necessary although not sufficient condition for a fluid element to be unbound [28]. We recall that this condition is exact only in an axisymmetric and stationary spacetime. These requirements are not matched during the matter-unstable phase, but the conditions can be used nevertheless as a first approximation to determine whether part of the material is actually escapes to infinity during the evolution. As is evident from Fig. 5.10, this condition is fulfilled throughout the whole evolution for the highly magnetized models `U11-2.0e15`, `U11-4.0e15` and `U11-1.0e16` not only on the finest refinement level shown in Fig. 5.10, but on the whole computational domain. However, this is not the case for model `U11-1.0e14` at the time the bar-mode instability is fully developed. In fact, in this case we observe that a little amount of unbound matter is shed in correspondence with one of the spiral arms of the bar. The ejection of matter occurs only in a very low-density region around the star, where $\rho \simeq 10^8$ g cm^{-3} $\simeq 10^{-6}\,\rho_c$. Overall, the total amount of matter (both bound and unbound) escaping from the outer grid after 20 ms of evolution is less than 0.2% of the total initial rest mass of the NSs.

The description of the dynamics of these four `U11` models can be further improved by reporting in Fig. 5.11 the spacetime diagram relative to the angular velocity Ω along the x-axis. We recall that all models have the maximum of Ω at the stellar center (cf., Fig. 3.1) and this remains the case also for the low-magnetic-field and bar-mode unstable models `U11-1.0e14` and `U11-2.0e15`, modulo the variations brought in by the development of the instability. On the other hand, for models `U11-4.0e15` and `U11-1.0e16`, the angular velocity at the stellar center first increases, then reaches a maximum and later decreases again; at the same time, the outer layers of the star expand and the maximum of the angular velocity occurs at larger radii. By the time an extended flattened envelope has been produced near the equatorial plane, much of the differential rotation has been washed out and the NS has acquired a central angular velocity that is smaller but mostly uniform.

The main features that have been accurately described in detail for the four magnetized `U11` models can be briefly summarized as follows:

- model `U11-1.0e14` is still bar-mode unstable and no effects are evident on the onset and development of the instability; a very small fraction of the rest-mass is shed at the edges of the bar-deformed object.

- model U11-2.0e15 is still bar-mode unstable but the instability shows a lower growth rate and the maximum distortion is a little lower as well.
- model U11-4.0e15 is bar-mode stable for the timescales considered here and after about 25 ms of evolution it settles into a more compact configuration; the new equilibrium structure has an almost uniform angular velocity and is surrounded by a differentially and flattened envelope.
- model U11-1.0e16 is also bar-mode stable with a dynamics that resembles that of model U11-4.0e15; the main differences are the shorter timescales required to reach equilibrium and the flattened envelope with larger mean rest-mass densities.

The qualitative behavior summarized above is consistent with what we would expect for highly magnetized and differentially rotating fluids. Under these conditions, in fact, magnetic braking transfers angular momentum from the core to the outer layers, changing the rest-mass density and the rotation profiles of the star. Because during this process part of the rotational energy of the star is tapped, the onset of the instability is inhibited. We recall that with the exception of the most-highly magnetized models, the β parameter is always above β_c at the time at which the instability develops in the case of zero magnetization. On the other hand, for the most extreme magnetizations β decreases very rapidly, going below β_c before the time when the instability develops for zero magnetizations. In Chap. 6 we will extensively discuss about the evolution of the magnetic field during the whole evolution. This will allow us to better clarify the mechanisms behind the above-mentioned changes in the dynamics of highly magnetized models.

5.3 Dynamics of U3 and U13 magnetized models

The same analysis we have accurately shown in Sec. 5.2 for U11 magnetized models has then been repeated for other two initial stellar configurations, in order to span the whole range of values of the rotation parameter β (cf., Fig. 5.1). These are model U3, which is only slightly overcritical in the unmagnetized case ($\beta_{\rm U3} = 0.2596 \gtrsim \beta_c$), and model U13, which on the contrary is largely overcritical at zero magnetization ($\beta_{\rm U13} = 0.2812 \gg \beta_c$).

The description of the dynamics for model U3 can be started from Fig. 5.12, where we show the time evolution of the distortion parameters η_+ and η. Looking at these diagnostic quantities, we can easily conclude that models U3-1.0e14 and U3-6.0e14 turn out to be

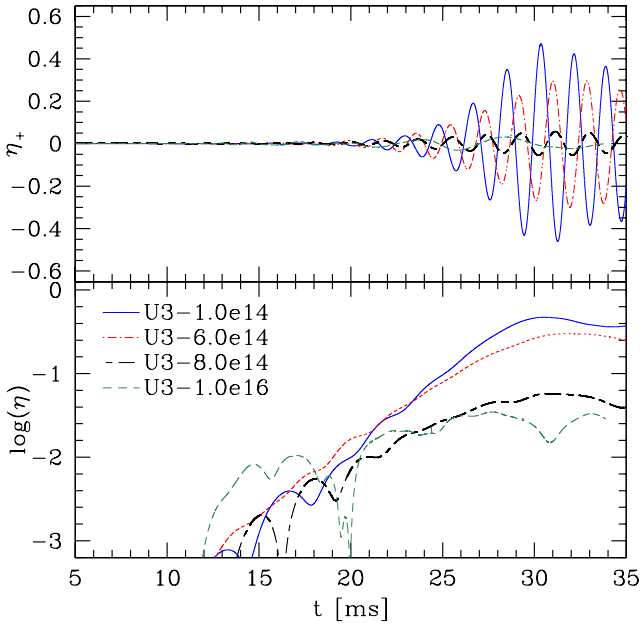

Figure 5.12: Evolution of the distortion parameters η_+ (top panel) and η (bottom panel) for `U3` models with different values of the initial poloidal magnetic field between 10^{14} and 10^{16} G.

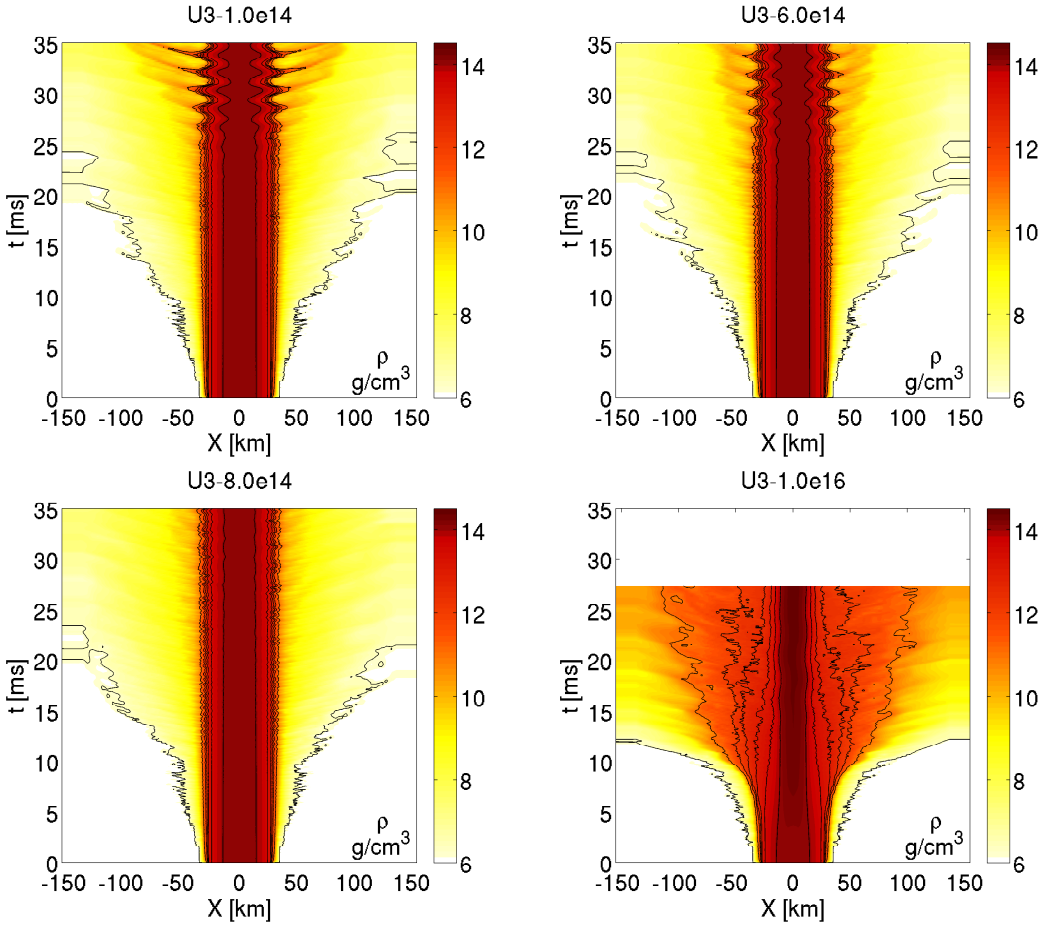

Figure 5.13: Spacetime diagrams of the evolution of the rest-mass density along the x-axis for the same `U3` models as in Fig. 5.12. Color code and isodensity contours are the same as in Fig. 5.9.

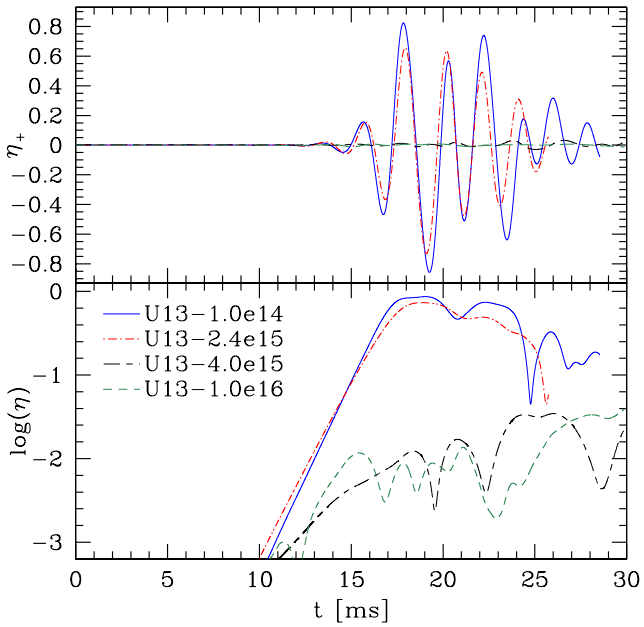

Figure 5.14: Evolution of the distortion parameters η_+ (top panel) and η (bottom panel) for U13 models with different values of the initial poloidal magnetic field between 10^{14} and 10^{16} G.

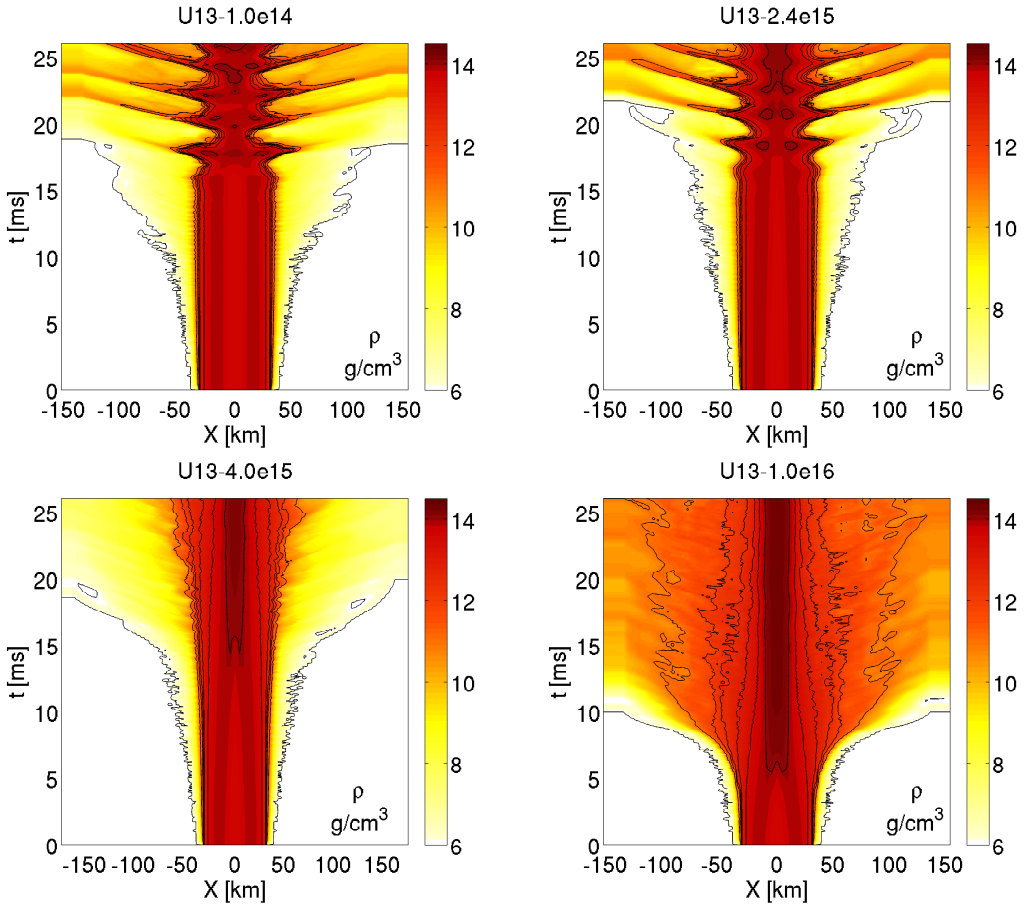

Figure 5.15: Spacetime diagrams of the evolution of the rest-mass density along the x-axis for the same U13 models as in Fig. 5.14. Color code and isodensity contours are the same as in Fig. 5.9.

bar-unstable, while `U3-8.0e14` and `U3-1.0e16` are stabilized by the presence of the strong initial magnetic field, so no bar deformation is observed in these two cases. Clearly, being quite close to the threshold for the onset of the instability at zero magnetization, the instability starts growing at a later time than for model `U11` and the maximum distortion is about half as large. In Fig. 5.13 we also show spacetime diagrams of the evolution of the rest-mass density ρ along the x-axis for these four differently magnetized `U3` models. The qualitative behavior of the two unstable models is almost the same as the one of `U11` models (cf., Fig. 5.9), even though the development of the instability is more moderate. Model `U3-1.0e16` shows no bar deformation and exhibits a transition from a toroidal configuration to an oblate one. In addition, a small amount of matter is shed on the equatorial plane forming a low density envelope around an axisymmetric configuration. Model `U3-8.0e14`, instead, shows neither a bar deformation nor an expansion of the outer layers, except for a very low density envelope with $\rho \lesssim 10^{-6}\,\rho_c$. Its behavior is almost the same as the one of model `S1-1.0e15` (cf., Fig. 4.4), which is just below the instability threshold and whose initial value of the rotation parameter is very similar ($\beta_{\rm S1} = 0.2540$). In this case, in fact, the differences between the initial and final configuration are negligible, at least within 35 ms of evolution, so the magnetic field is just strong enough to cause the suppression of the instability without any other effects on the dynamics.

The general dynamics of `U13` magnetized models is represented by the time evolution of the distortion parameters η_+ and η, which is shown in Fig. 5.14. This reveals that models `U13-1.0e14` and `U13-2.4e15` are still unstable, while `U13-4.0e15` and `U13-1.0e16` show no development of a bar deformation, due to the presence of magnetic fields. Being far from the instability threshold, for the two unstable models the instability shows a steeper growth than the one in `U3` and `U11` unstable models and the maximum distortion is a little higher than for `U11` models with comparable initial magnetic fields. In Fig. 5.15 we show spacetime diagrams of the evolution of the rest-mass density ρ along the x-axis for all the four differently magnetized `U13` models. The qualitative behavior is almost the same as the one of `U11` models (cf., Fig. 5.9), even though the development of the instability is now more violent and the spiral arms have a wider extent.

5.4 Quantitative effects of magnetic fields on the dynamics

A more quantitative assessment of the influence of the magnetic fields on the unstable models has been obtained after performing a number of simulations of models `U3`, `U11` and `U13`, with

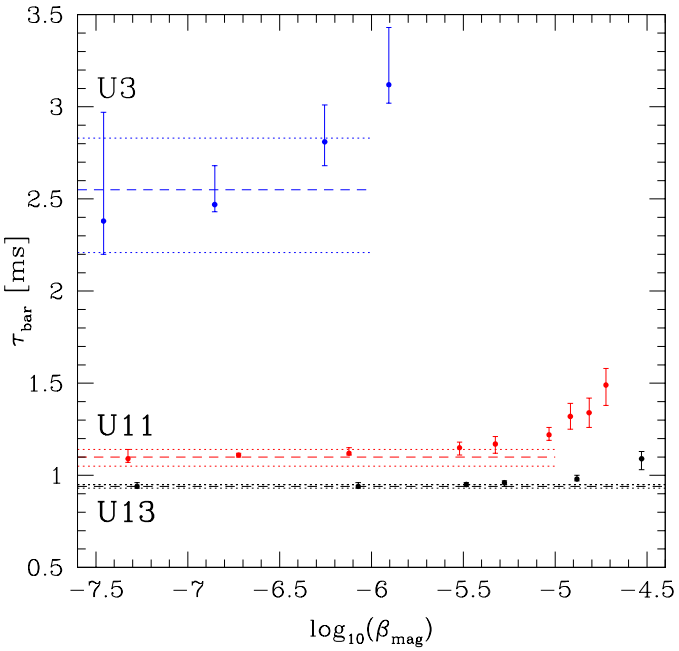

Figure 5.16: Growth time of the bar-mode instability for the three unstable models `U3` (blue), `U11` (red) and `U13` (black), shown as a function of the initial magnetization. The horizontal dashed lines report the growth times in the absence of magnetic fields, while the dotted lines represent the corresponding error bars.

initial poloidal magnetic fields varying in the whole parameter space shown in Figs. 5.1. More specifically, we have performed 27 simulations with initial maximum magnetic fields in the range $B^z_{\rm max}|_{t,z=0} = 1.0 \times 10^{14}$ and 1.0×10^{16} G. All the results of this extensive investigation are collected in Figs. 5.1 and 5.16, as well as in Table 5.1, which reports the measured growth time of the instability $\tau_{\rm bar}$ and its frequency $f_{\rm bar}$. In particular, Fig. 5.1 reports the initial models within a $(\beta,\, \beta_{\rm mag})$ diagram and allows one to easily distinguish the ranges of rotational and magnetic energies that allow for the development of a dynamical bar-mode instability. It is, in fact, easy to distinguish models that are bar-mode stable (blue symbols) from those that are unstable (red symbols) at zero magnetizations; of course, models that are stable at zero magnetizations are also stable at all magnetizations (this is marked with the vertical red dashed line). Equally simple is to distinguish models that, although unstable in the absence of magnetic fields, become stable with sufficient magnetization (red triangles). As an example, for models `U3` the threshold between squares and triangles appears for initial maximum magnetic fields $B^z_{\rm max}|_{t,z=0} > 6.0 \times 10^{14}$ G, while for models `U11` and `U13` the threshold is at about 2.0×10^{15} and 2.4×10^{15} G respectively. As a result, only the light-red shaded area in Fig. 5.1 collects

stellar models that are bar-mode unstable. Outside this region, either the rotational energy is insufficient, or the magnetic tension is too strong to allow for the development of the instability.

Similarly, Fig. 5.16 reports the measured growth time of the bar-mode instability $\tau_{\rm bar}$ (and the corresponding error bars) for the three different classes of unstable models (`U3`, `U11` and `U13`) as a function of the magnetization parameter $\beta_{\rm mag}$. Taking the horizontal dashed lines as references for the unmagnetized models, it is easy to realize that as the magnetization increases, so does the growth time for the instability. This behavior can be physically interpreted as due to the fact that as the magnetic field strength increases, so does the timescale over which the magnetic tension needs to be won to develop a bar deformation[1].

[1]Note that the error bars are larger for model `U3` because this is closer to the stability threshold (cf., Table 3.2).

Model	$\beta_{\rm mag}$	t_1 [ms]	t_2 [ms]	$\eta_{\rm max}$	$\tau_{\rm bar}$ [ms]	$f_{\rm bar}$ [Hz]
U11-0.0e00	0.0	16.2	18.3	0.784	$1.10^{+0.04}_{-0.05}$	490^{+1}_{-4}
U11-1.0e14	4.7×10^{-8}	14.7	16.8	0.787	$1.09^{+0.05}_{-0.02}$	491^{+3}_{-6}
U11-2.0e14	1.9×10^{-7}	15.0	17.0	0.778	$1.11^{+0.02}_{-0.01}$	488^{+1}_{-1}
U11-4.0e14	7.5×10^{-7}	15.1	17.7	0.773	$1.12^{+0.03}_{-0.01}$	488^{+2}_{-2}
U11-8.0e14	3.0×10^{-6}	14.8	18.2	0.754	$1.15^{+0.03}_{-0.04}$	490^{+2}_{-5}
U11-1.0e15	4.7×10^{-6}	14.2	16.8	0.751	$1.17^{+0.04}_{-0.05}$	491^{+2}_{-4}
U11-1.4e15	9.2×10^{-6}	13.9	16.2	0.714	$1.22^{+0.04}_{-0.03}$	491^{+1}_{-2}
U11-1.6e15	1.2×10^{-5}	14.5	17.3	0.681	$1.32^{+0.07}_{-0.07}$	489^{+2}_{-1}
U11-1.8e15	1.5×10^{-5}	13.2	16.7	0.639	$1.34^{+0.08}_{-0.08}$	490^{+2}_{-1}
U11-2.0e15	1.9×10^{-5}	14.8	17.3	0.532	$1.49^{+0.09}_{-0.11}$	489^{+4}_{-2}
U13-0.0e00	0.0	11.6	14.7	0.865	$0.94^{+0.01}_{-0.01}$	449^{+1}_{-3}
U13-1.0e14	5.3×10^{-8}	12.2	15.3	0.866	$0.94^{+0.02}_{-0.01}$	450^{+2}_{-2}
U13-4.0e14	8.5×10^{-7}	12.7	15.8	0.851	$0.94^{+0.02}_{-0.01}$	450^{+2}_{-2}
U13-8.0e14	3.3×10^{-6}	12.7	15.8	0.842	$0.95^{+0.01}_{-0.01}$	451^{+1}_{-2}
U13-1.0e15	5.3×10^{-6}	14.1	16.7	0.833	$0.96^{+0.01}_{-0.02}$	451^{+3}_{-1}
U13-1.6e15	1.3×10^{-5}	11.6	14.8	0.813	$0.98^{+0.02}_{-0.01}$	456^{+1}_{-2}
U13-2.4e15	3.0×10^{-5}	13.0	15.9	0.734	$1.09^{+0.04}_{-0.06}$	461^{+1}_{-1}
U3-0.0e00	0.0	24.8	26.4	0.486	$2.55^{+0.28}_{-0.34}$	540^{+2}_{-2}
U3-1.0e14	3.5×10^{-8}	24.9	27.1	0.472	$2.38^{+0.59}_{-0.18}$	537^{+5}_{-10}
U3-2.0e14	1.4×10^{-7}	26.1	28.0	0.456	$2.47^{+0.21}_{-0.04}$	536^{+5}_{-3}
U3-4.0e14	5.6×10^{-7}	24.0	26.3	0.421	$2.81^{+0.20}_{-0.13}$	537^{+2}_{-3}
U3-6.0e14	1.2×10^{-6}	24.2	25.7	0.300	$3.12^{+0.31}_{-0.10}$	535^{+5}_{-6}

Table 5.1: Main properties of the initial part of the instability for model U11, U13 and U3 for different values of the initial poloidal magnetic field. Here we report the representative times t_1 and t_2 between which the maximum values of the distortion parameter η, the growth times $\tau_{\rm bar}$ and the frequencies $f_{\rm bar}$ are computed.

5. DYNAMICAL BAR-MODE INSTABILITY IN MAGNETIZED AND ROTATING RELATIVISTIC STARS

Chapter 6

Evolution of magnetic fields

This Chapter focuses on the dynamics of magnetic fields, during both the initial phase of the evolution, which is common to stable and unstable models, and after the onset of the bar-mode instability, when the initial axisymmetric is lost.

All the simulations presented in this Thesis have been performed in the ideal-MHD approximation, in which the conductivity is assumed to be infinite. In this limit, the diffusion becomes very slow, so the evolution of the magnetic field is completely determined by the plasma flow (the field is assumed to be "frozen-in" to the plasma). That means that two plasma elements that are on a common field line will remain on the same field line. In this sense we can actually talk about "moving" field lines. There are several processes involving compact objects, such as NSs and BHs, where resistive effects could play an important role. These include the interaction of the magnetospheres of two NSs in a binary system before the merger, the stability of the magnetosphere that may be produced around a HMNS, or the stability of the magnetic field within the torus that will be produced once the HMNS collapses to a black hole. In all of these scenarios, the ideal-MHD limit may not be sufficient to study those physical phenomena which involve reconnection or the presence of anisotropic resistivities. Anyway, when considering the interior dynamics of magnetized stars the electrical conductivity of the plasma is extremely high and the ideal-MHD limit represents a very good approximation, so our choice is justified.

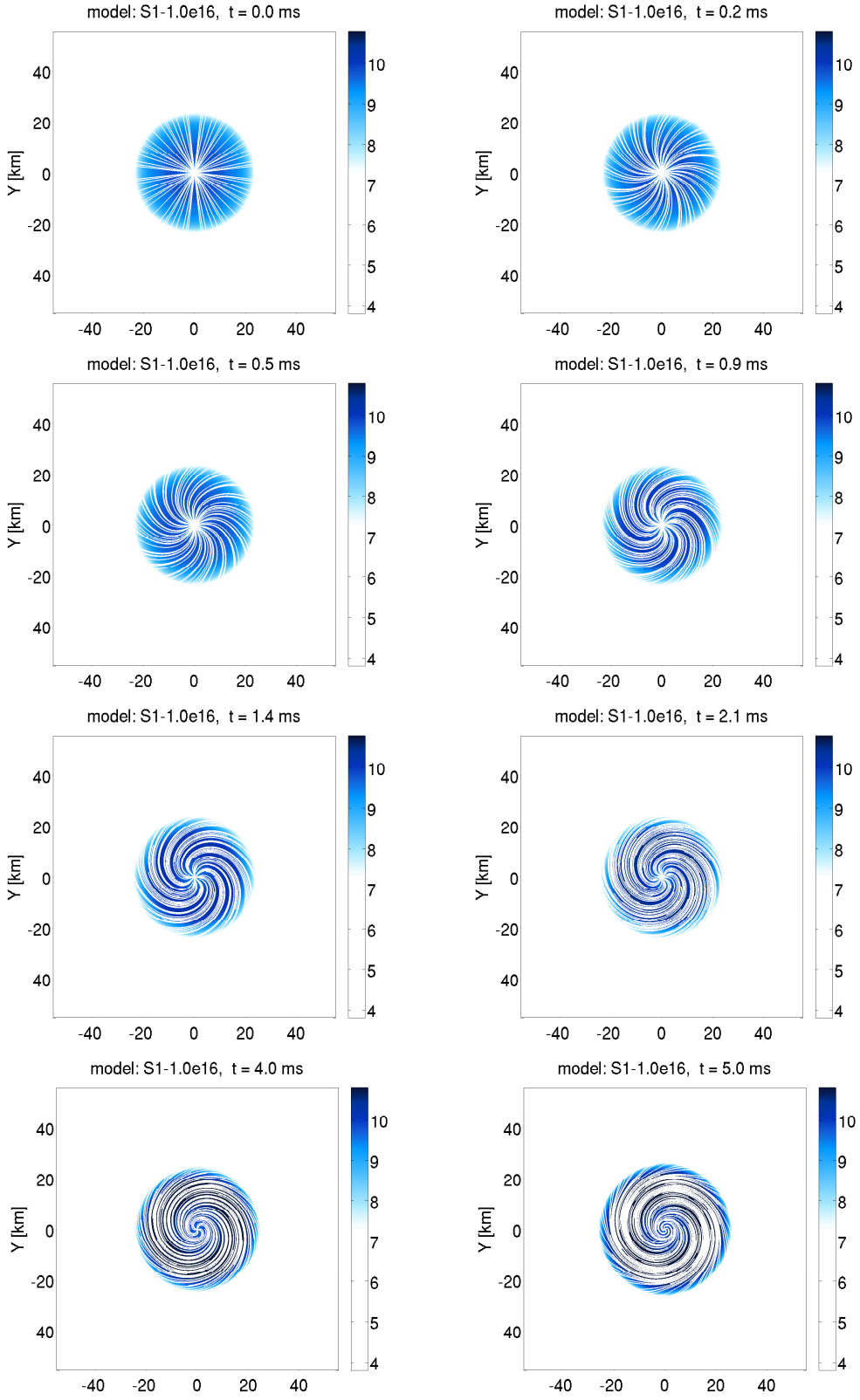

Figure 6.1: Snapshots of the total electromagnetic energy density $T^{00}_{\rm em}$, as measured in the Eulerian frame, on a horizontal plane at $z \simeq 1.5$ km for model `S1-1.0e16` at different times during the first 5 milliseconds of evolution. The color code is defined in terms of $\log_{10}(T^{00}_{\rm em}/c^2)$ where $T^{00}_{\rm em}/c^2$ is in cgs units (g cm^{-3}). Additionally, magnetic field lines are shown with white solid lines.

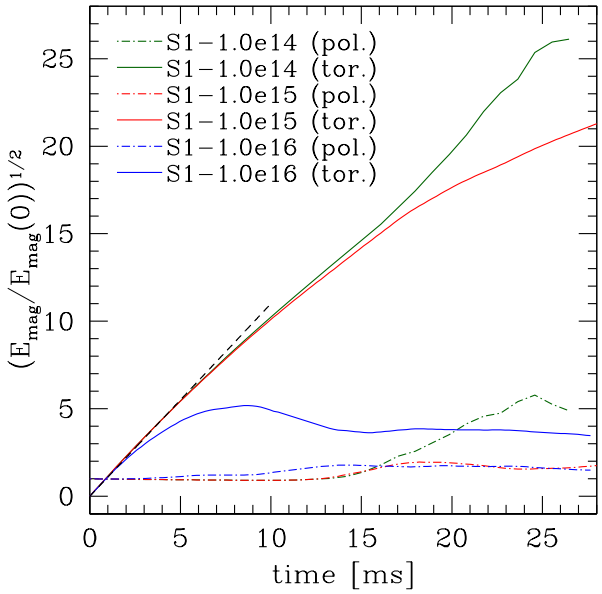

Figure 6.2: Time evolution of the square root of the poloidal component of the magnetic energy $E^{\rm pol}_{\rm mag}$ [cf., Eq. (3.21)] and its toroidal component $E^{\rm tor}_{\rm mag}$ [cf., Eq. (3.21)], both normalized to the initial total magnetic energy, for differently magnetized `S1` models. Dash-dot lines are used for the former, solid lines for the latter. Lines drawn with different colors refer to models with different values of the initial magnetic field strength. The black dashed line is a straight line, providing a comparison with a linear growth.

6.1 Effects of differential rotation

In Fig. 6.1 we show some representative snapshots of the total electromagnetic energy density $T^{00}_{\rm em}$ as measured in the Eulerian frame on a horizontal plane at $z \simeq 1.5$ for bar-stable model `S1-1.0e16`. Note that the color code here is defined in terms of $\log_{10}(T^{00}_{\rm em}/c^2)$, where $T^{00}_{\rm em}/c^2$ is expressed in cgs units (g cm^{-3}). Additionally, magnetic field lines are superimposed to every snapshot, drawn with white solid lines. These are clearly dragged along with the fluid in differential rotation and rapidly wind on a timescale of very few milliseconds, leading to a sudden formation and rapid growth of a toroidal magnetic field component. This can be also observed in Fig. 6.2, where we show the time evolution of the square root of the poloidal component of the magnetic energy $E^{\rm pol}_{\rm mag}$ [cf., Eq. (3.21)] and its toroidal component $E^{\rm tor}_{\rm mag}$ [cf., Eq. (3.21)], both normalized to the initial total magnetic energy, for differently magnetized `S1` models. The first obvious thing to notice is that for all the three magnetizations considered, i.e., $B^z_{\rm max}|_{t,z=0} = 10^{14}$, 10^{15} and 10^{16} G, the growth of the toroidal magnetic field component is linear in time initially. This is not surprising and is indeed the mere manifestation of the "frozen-in" condition of the magnetic field within the ideal-MHD approximation. Using the

induction equation it is, in fact, straightforward to show that in a linear regime the differential rotation will generate toroidal magnetic field at a rate which is linear in time. This is because as long as the stellar configuration remains axisymmetric the poloidal magnetic field is not affected by the newly produced toroidal field, and the total electromagnetic energy can only grow linearly with time tapping part of the rotational energy of the star. A black dashed line is drawn in the figure, in order to offer a sudden comparison with a linear growth. This initial linear phase lasts about 5 ms for models `S1-1.0e14` and `S1-1.0e15`, while it stops only after about 2 ms for model `S1-1.0e16`. As a result of this growth, the toroidal component becomes rapidly larger than the initial poloidal one and an amplification of the toroidal electromagnetic energy takes place for all models. In the case of model `S1-1.0e15`, this reaches a higher value of about two orders of magnitude over a timescale of ~ 10 ms and then it keeps growing at a slower rate, becoming four times higher at the end of the simulation (about 28 ms). In the case with an ultra-strong magnetic field, namely `S1-1.0e16`, a saturation occurs already after very few milliseconds, at a value that is only an order of magnitude higher than the initial one. For both these models, the poloidal component of the magnetic energy shows only very minor changes, increasing only by a factor of 2 during the whole evolution. The least magnetized case, namely `S1-1.0e14`, is quite peculiar. Its behavior is exactly the same as for model `S1-1.0e15` during the first 10 ms of evolution, but then is starts deviating from that. The toroidal component of the magnetic energy shows a much higher and quicker increase, reaching a higher value of about 50%, and even the popoidal one undergoes an amplification, getting about an order of magnetic above the constant value of the other two magnetized models. A possible explanation to this feature will be proposed in Sec. 6.2.

In Fig. 6.3 we show some representative snapshots of the total electromagnetic energy density $T^{00}_{\rm em}$ as measured in the Eulerian frame on a horizontal plane at $z \simeq 1.5$ for the bar-unstable model `U11-1.0e14`. Here, we observe the winding of the magnetic field lines in the early phase just as for the stable model `S1-1.0e16` we have just described (see the first snapshot, corresponding to $t = 5$ ms). Anyway, in this matter-unstable case, later in the evolution the distortion of the magnetic field lines also mimics the bar-mode deformation as the star undergoes the development of the instability. In Fig. 6.4, 6.5 and 6.6 we show some representative snapshots of the total electromagnetic energy density for models `U11-2.0e15`, `U11-4.0e15` and `U11-1.0e16` respectively. Note that all the panels in these three figures have the same color ranges as in Fig. 6.3, but the colormap is different for different initial magnetic field strengths in order to better highlight the internal structure of the electromagnetic field. The

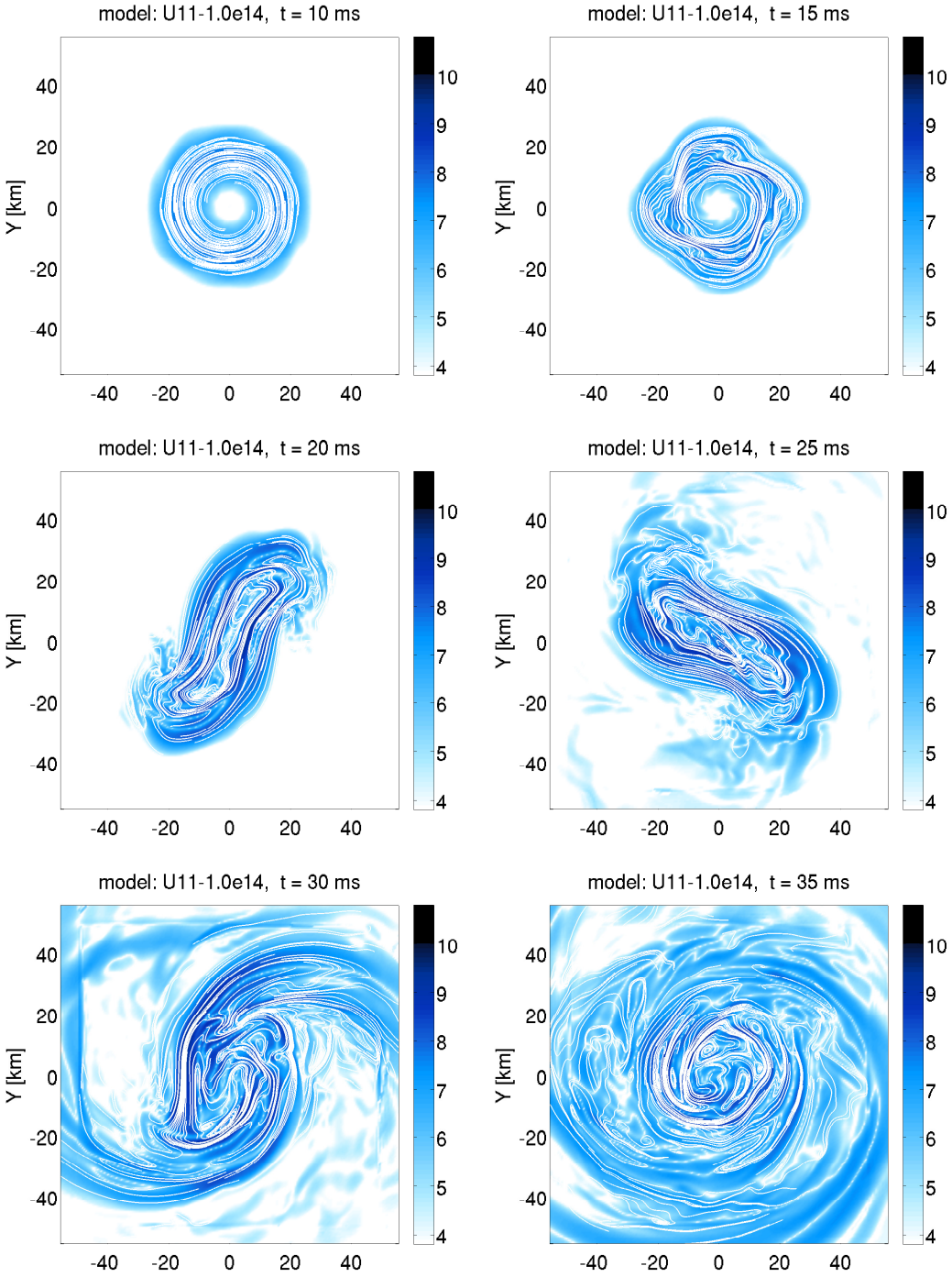

Figure 6.3: Same as Fig. 6.1 but for model `U11-1.0e14` at $t = 10$, 15, 20, 25, 30 and 35 ms.

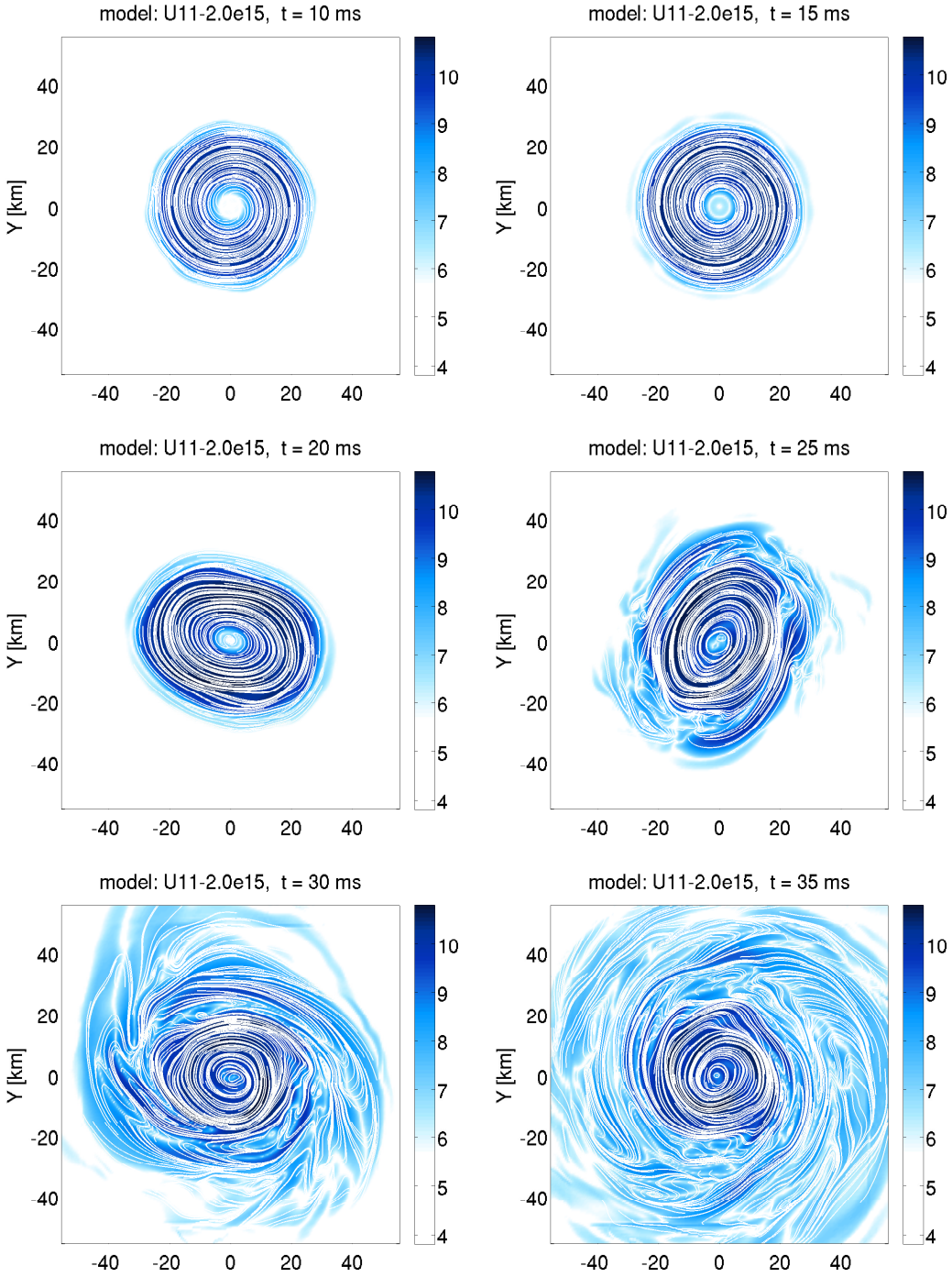

Figure 6.4: Same as Fig. 6.1 but for model `U11-2.0e15` at $t = 10$, 15, 20, 25, 30 and 35 ms.

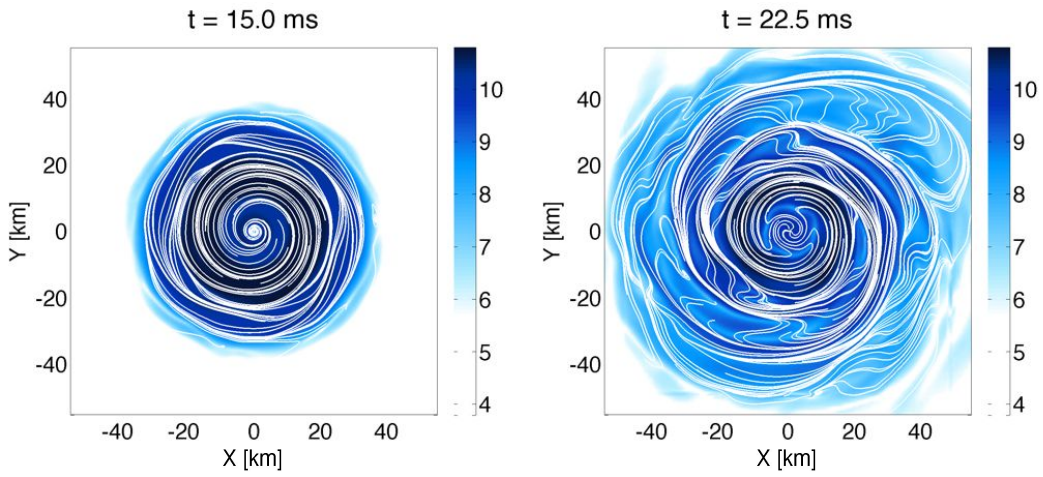

Figure 6.5: Same as Fig. 6.1 but for model `U11-4.0e15` at $t = 15$ and 22.5 ms.

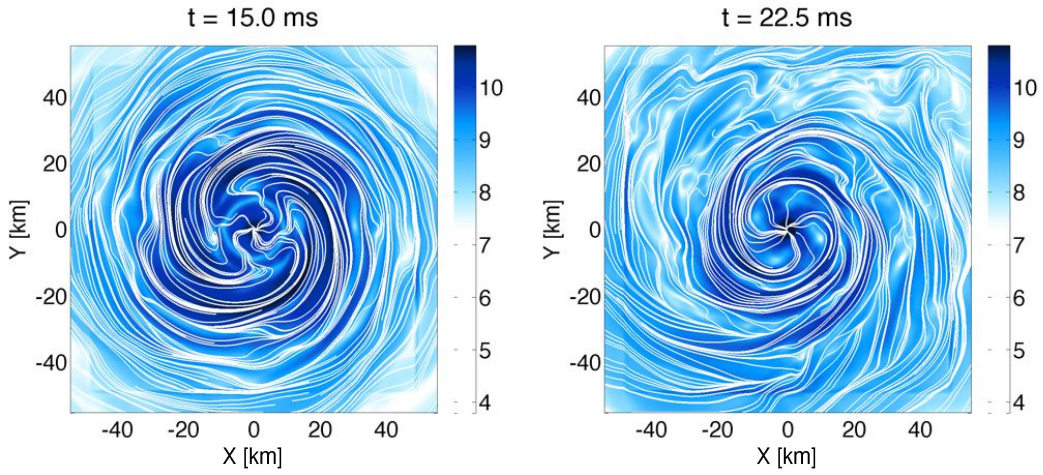

Figure 6.6: Same as Fig. 6.1 but for model `U11-1.0e16` at $t = 15$ and 22.5 ms.

expected winding of the field lines and the consequent linear growth of the toroidal field are clearly present in all three models and are independent of the initial poloidal magnetic field strength. The reason is that they only depend on the angular velocity profile, or equivalently on the differential rotation law, which is the same for all `U11` models in the first part of the evolution.

In Fig. 6.7 we report a full summary of the evolution of the normalized magnetic energy for all the evolved magnetized models: bar-stable models (upper-left panel), `U3` models (upper-right panel), `U11` models (lower-left panel) and `U13` models (lower-right panel) for different initial poloidal magnetic-field strengths. The behavior of the magnetic field is almost the same for all stable models with $B^z_{\rm max}|_{t,z=0} = 10^{15}$ G, while when $B^z_{\rm max}|_{t,z=0} = 10^{16}$ G the maximum value of the total magnetic energy is a little different for the different models, with the value at the end of the evolution being quite similar.

The growth of the magnetic-field strength in bar-mode unstable models offers the opportunity for a number of useful considerations. The first obvious thing to notice for all the considered magnetized models is that the growth of the magnetic energy is linear in time initially. As we already discussed for model `S1-1.0e16`, the toroidal component becomes rapidly larger than the initial poloidal one and an amplification of the total electromagnetic energy takes place, reaching a higher value of about two orders of magnitude over a timescale of ~ 10 ms. After this initial phase, the toroidal field keeps growing at a slower rate, reaching a saturation with the maximum amplification being almost independent of the initial poloidal magnetic field strength and of the rotation of the stellar model. The only exceptions to this behavior appear in models with ultra-strong magnetic fields, in which cases the saturation occurs at values that are about two orders of magnitude smaller (cf., blue solid lines in the different panels of Fig. 6.7). Interestingly, for models `U11` and `U13`, that is for the unstable models with smaller growth rates and far from the threshold of the dynamical bar-mode instability, the linear growth of the magnetic field is followed also by a rather short exponential growth of the magnetic field. We will describe this feature and try to provide a possible explanation in Sec. 6.3.

6.2 An overview on the magnetorotational instability

In the previous Section we hinted at the presence of a short exponential growth in the evolution of the magnetic energy, occurring in many magnetized `U11` and `U13` models after about 15-20 ms of evolution (see Fig. 6.7). This behavior is actually quite similar to the one recently seen

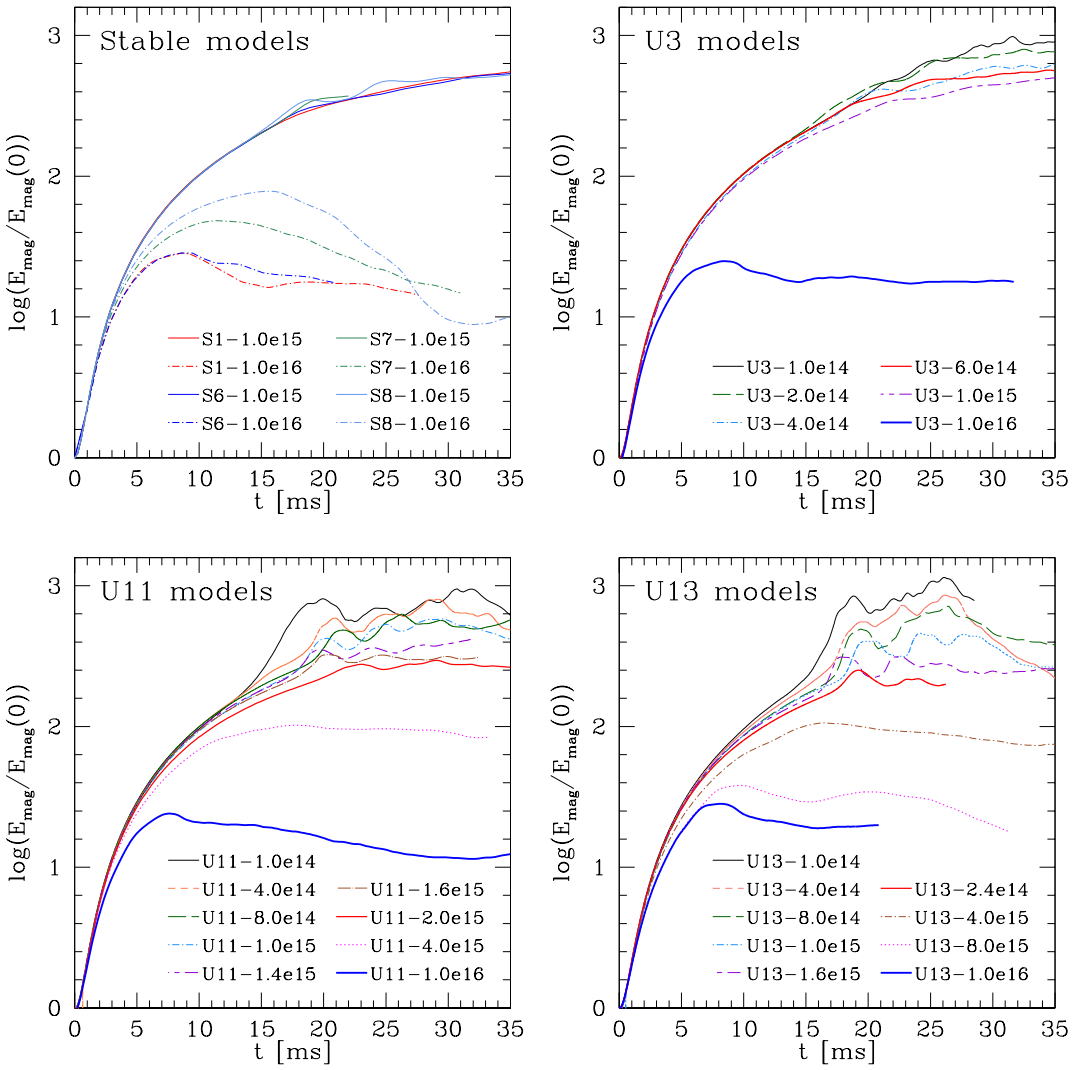

Figure 6.7: Evolution of the total magnetic energy $E_{\rm mag}$, normalized to its initial value, for the different categories of models we evolved, namely all the stable models (upper-left panel), the `U3` sequence with different values of the magnetization (upper-right panel), the `U11` sequence (lower-left panel) and the `U13` sequence (lower-right panel). In the case of stable models, the solid lines refer to models with $B^z_{\rm max}|_{t,z=0} = 10^{15}$ G, while the dash-dot lines to models with $B^z_{\rm max}|_{t,z=0} = 10^{16}$ G. In the case of unstable models, the black solid line refers to the least magnetized case, the blue solid line to the most magnetized case, and the red solid line to the last unstable model before excessive magnetic tension suppresses the instability.

in Ref. [34], where it was attributed to the development of the magnetorotational instability (MRI). Anyway, a similar conclusion cannot be drawn with the same confidence here, the main motivation for this being the lower resolution of our simulations in respect to the one employed in Ref. [34]. Before analyzing in detail all the clues in favor or against this hypothesis, it's useful to recall here the main features of this type of instability and the physical mechanism behind its onset and growth.

The MRI arises from the action of the magnetic field in a differentially rotating system. It is also known as the Balbus-Hawley instability, since they discovered its relevance in accretion disks numerically in 1991, after it was originally studied in the 1950s by Chandrasekhar [112, 113] and independently by Velikhov [114]. Indeed, it is thought to be responsible for turbulence and angular momentum transport in astrophysical disks, being able do lead to large scale mixing and turbulence very quickly. Given that magnetic fields are quite omnipresent in the universe and that differentially rotating disks are commonplace, the MRI can act in a huge number of different astrophysical scenarios (including X-ray binaries, the Galactic disk and protoplanetary disks).

A brief explanation of the nature of the MRI can help us understand its behavior and look for its features in our simulations. In an ideal plasma the action of the magnetic field is to link neighboring fluid elements that lie along a common field line, so they can be thought as connected with elastic bands. If we try to displace such elements perpendicular to a magnetic field line, the magnetic tension behaves as an attractive force that acts to bring them back together, just like in a spring under tension. Normally, such a force is restoring and, hence, it tends to preserve a system's stability. However, if the fluid is differentially rotating, this restoring force can actually be destabilizing. Understanding how this can be possible is straightforward if we just consider two neighboring fluid elements situated along a stellar radius and connected together by a spring representing the magnetic force. Since the star is differentially rotating, the inner element is of course rotating faster than the outer one, so the initial displacement increases and the magnetic tension causes the former to slow down and the latter to speed up. This transfer of angular momentum makes the inner fluid element migrate inwards while the outer one is pushed outwards. Now, this cycle can be repeated from the start, but with a larger displacement than the initial one. However, if the magnetic field is too strong, the tension will cause the displacement between fluid elements to oscillate rather than grow and this feedback cycle won't run. This is why the MRI is usually considered as a weak-field instability.

The necessary conditions for the MRI to develop are the following:

- differential rotation, with the angular velocity decreasing outwards ($d\Omega/dR < 0$);
- presence of a weak poloidal magnetic field (i.e., a magnetic field component which points in a direction normal to the rotation).

Analyzing the role of magnetic fields in a differentially rotating plasma is in general a highly complex nonlinear problem that can only be treated by means of numerical simulations. Anyway, this is usually a very challenging task for numerical MHD as well, due to the very high resolution needed to resolve the MRI-modes which requires the use of massive computational resources. This can be easily understood by having a look at an order-of-magnitude estimate for the typical wavelength of these modes. In Ref. [33], they estimate the characteristic timescale $\tau_{\rm MRI}$ and the wavelength of the fastest growing mode $\lambda_{\rm MRI}$, making use of a simple Newtonian linear analysis [115], to be of the order of:

$$\lambda_{\rm MRI} \sim 3\,{\rm cm}\left(\frac{\Omega}{4000\,{\rm rad\,s^{-1}}}\right)^{-1}\left(\frac{B}{10^{12}\,{\rm G}}\right), \tag{6.1}$$

$$\tau_{\rm MRI} \sim \Omega^{-1} \sim 0.25\,{\rm ms}\left(\frac{\Omega}{4000\,{\rm rad\,s^{-1}}}\right)^{-1}. \tag{6.2}$$

The characteristic timescale $\tau_{\rm MRI}$ is independent of the magnetic field strength and only depends on the angular velocity, so it is supposed to have the same value for all the differently magnetized models sharing the same initial matter configuration. Instead, $\lambda_{\rm MRI}$ is linear in the magnetic field, so larger magnetic fields will result in longer MRI wavelengths. Of course, when $\lambda_{\rm MRI} \gtrsim R_e$, the characteristic length scale of the instability is comparable with the equatorial radius of the star R_e and so the development of the MRI will be inhibited. On the contrary, when $\lambda_{\rm MRI} \ll R_e$, the resolution will not be high enough to resolve it. That means that a clear and definite detection of the effects of the MRI in 3D global numerical simulations is indeed quite a challenging goal, due to the demanding computational requirements.

6.3 Search for non-axisymmetric MRI

It's important to recall here that the estimates (6.1) - (6.2) have been computed from a linear perturbation analysis of the Newtonian MHD equations for axisymmetric perturbations, which can at best hold approximately only in the case of bar-stable models (i.e., `S`-models) or models that are stabilized by the presence of the magnetic field (i.e., only highly magnetized `U`-models). In all other cases, instead, the development of the bar-mode instability leads to a considerable

deformation of the initial configuration, breaking axisymmetry, and so these estimates cannot be fully trusted anymore.

The typical value of the angular velocity Ω appearing in Eq. (6.1) and (6.2) is 4000 rad s^{-1}. This can actually be considered as an approximate average value for the angular velocity of our initial models (cf., Tab. 3.2), so we can expect as an order-of-magnitude estimate for the timescale $\tau_{\rm MRI} \sim 0.25$ ms. Of course, the real value would be a little lower for model `S8`, which is the fastest rotating model, than for model `U13`, which is the slowest rotating one. The estimate of the characteristic wavelength, instead, is also dependent on the initial magnetic field strength and so is different for each magnetized model. The magnetic field being equal, we would expect $\lambda_{\rm MRI}$ to be about an order of magnitude higher than in Ref. [34], since the angular velocity of the model they studied is $\Omega_c = 2\pi \times 7.0 \sim 44000$ rad s^{-1}, which is just an order of magnitude higher than the average value for our models. For example, for one of our stable models with a magnetic field $B \sim 10^{15}$ G we should expect $\lambda_{\rm MRI} \sim 30$ m.

Our analysis of the main points in favor and against the possibility that the MRI could actually develop in our models starts from Fig. 6.7, which suggests that `U13` magnetized models are the ones that show the most pronounced exponential growth of the total magnetic energy. Therefore, we decided to perform many other simulations, in particular:

- seven more simulations of magnetized models, all having `U13` as initial matter configuration but with many different initial magnetic field strengths between 10^{11} and 10^{14} G, at fixed resolution Δx = 0.378 km (which is better than the one employed in all the simulations reported in Chap. 4 and 5);
- five more simulations of model `U13-1.0e14` at different resolutions between Δx = 0.378 km and Δx = 1.180 km;

These additional simulations were chosen with the specific aim of identifying particular features that one would expect to observe if an MRI was acting during the evolution, and they actually allow us to analyzed the evolution of the magnetic field at better resolution and in a more accurate way.

In particular, in the upper-left panel of Fig. 6.8 we show the evolution of the square root of the total magnetic energy $E_{\rm mag}$ for six differently magnetized `U13` models with initial magnetic field strengths between 10^{12} and 10^{14} G at fixed resolution, i.e., Δx = 378 m. Clearly, the initial slope of these curves is different for different values of the seed poloidal magnetic field, being linear in it, as expected from theory. Later in the evolution, a sudden and rapid

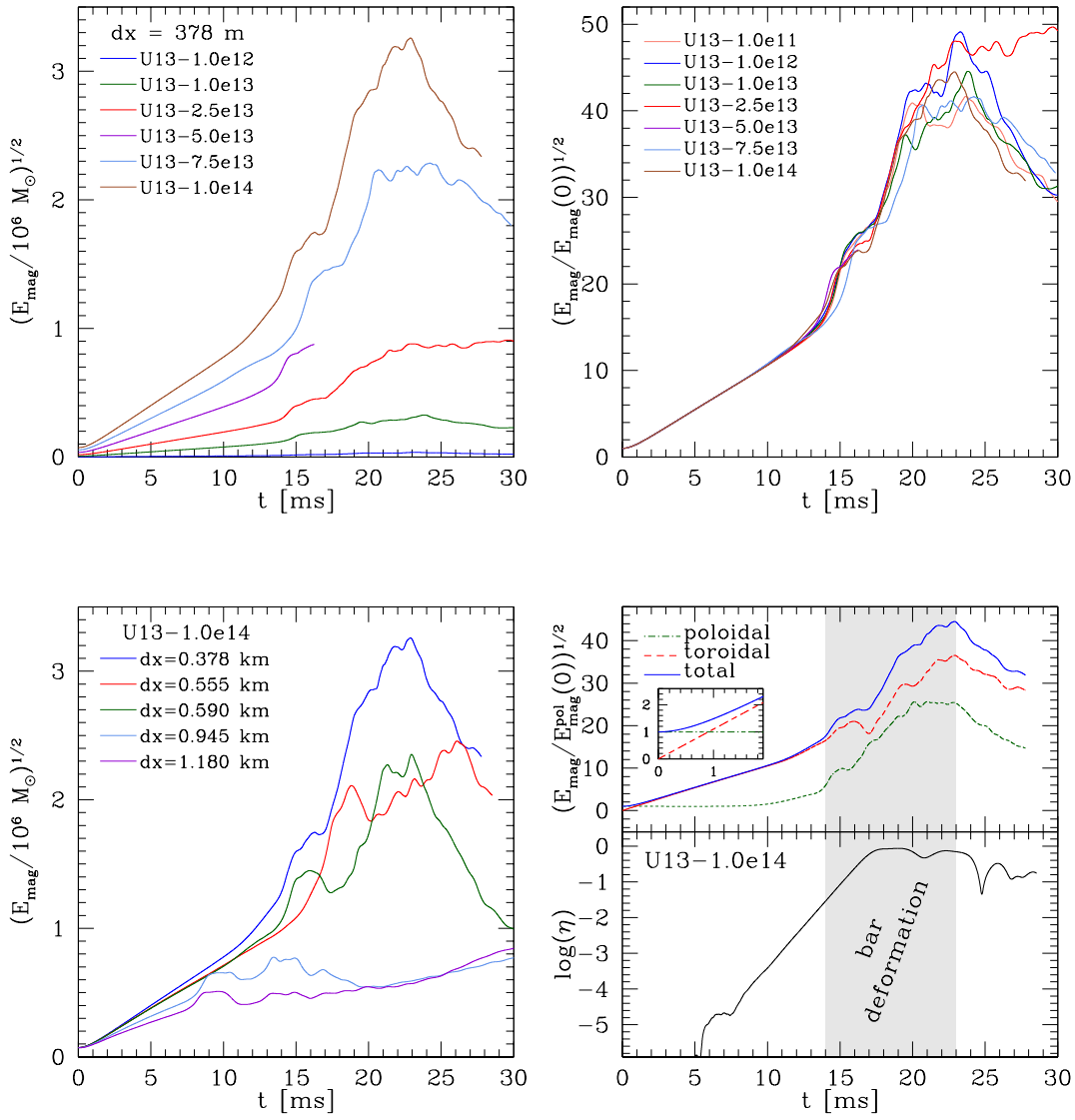

Figure 6.8: *Upper-left panel:* evolution of the square root of the total magnetic energy $E_{\rm mag}$ for six differently magnetized `U13` models with initial magnetic field strengths between 10^{12} and 10^{14} G, at fixed resolution. *Upper-right panel:* evolution of the square root of the total magnetic energy $E_{\rm mag}$, normalized to its initial value, for the same models as in the upper-right panel plus `U13-1.0e11`. *Lower-left panel:* evolution of the square root of the total magnetic energy $E_{\rm mag}$ for model `U13-1.0e14` at five different resolutions. *Lower-right panel:* evolution of the square root of the total magnetic energy $E_{\rm mag}$, of its toroidal component $E^{\rm tor}_{\rm mag}$ [Eq. (3.20)] and its poloidal component $E^{\rm pol}_{\rm mag}$ [Eq. (3.21)], all normalized to the initial value. A sudden increase can be observed in correspondence with the bar-unstable phase, as can infer by looking at the time evolution of the distortion parameter η. A magnification of the first 2 ms of the evolution is shown in the inset, to better appreciate the moment when the toroidal component overcomes the poloidal one.

growth of the magnetic energy is observed, which is is higher for the most magnetized model (i.e., , `U13-1.0e14`), while is barely visible for the least magnetized ones. If this growth was actually due to an MRI, the characteristic wavelength $\lambda_{\rm MRI}$ would be linear in the magnetic field and then modes corresponding to stronger fields would be easier to detect, allowing for a full development of the instability. When weaker fields are acting, instead, $\lambda_{\rm MRI}$ would be too short in respect to the resolution employed and so the effects of the MRI could not be captured, or only partially captured, explaining the minor growth. In the upper-right panel of Fig. 6.8, we show the evolution of the same quantity but normalized to its initial value, for the same models plus `U13-1.0e11`. Clearly, for all these models the magnetic field shows the very same evolution in the first 12 milliseconds, since this is due to the winding up of the magnetic field lines and only depends on the differential rotation profile, which is the same for all models. Later in the evolution, the growth time is clearly independent of the the magnetic field strength, just as we would expect if the characteristic time scale was $\tau_{\rm MRI}$ [cf., Eq.(6.2)]. It's important here to note that after the initial linear growth and just before the sudden exponential growth, the square root of the total magnetic energy has increased between 10 and 20 times above its initial value. This implies that we should take into account this higher value, and not the initial one, in order to get a more accurate estimate for $\lambda_{\rm MRI}$. This is even more true if we think that an MRI would actually act on the toroidal component (even if the presence of a poloidal component is a necessary requirement), which is in fact much higher than the poloidal one at that time. That means that for an initial purely poloidal magnetic field with strength 10^{14} G we would get $\lambda_{\rm MRI} \sim 30-60\,{\rm m}$ instead of 3 m, while for $B \sim 5\times10^{14}$ we would get $\lambda_{\rm MRI} \sim 150-300\,{\rm m}$. In the lower-left panel of Fig. 6.8 we show the evolution of the square root of the total magnetic energy $E_{\rm mag}$ for model `U13-1.0e14`, the one who exhibits the most pronounced exponential growth, at five different resolutions between Δx = 0.378 km and Δx = 1.180 km. It's clearly evident that this growth is resolution dependent, since the simulation performed at the highest resolution shows the highest growth while the ones at much coarser resolutions show almost no growth at all. Again, that would be consistent with the expectation that the higher is the resolution, the more the MRI modes can be fully captured and their effects observed. Lastly, in the lower-right panel of Fig. 6.8 we show the evolution of the square root of the total magnetic energy $E_{\rm mag}$, of its toroidal component $E^{\rm tor}_{\rm mag}$ [cf., Eq. (3.20)] and its poloidal component $E^{\rm pol}_{\rm mag}$ [cf., Eq. (3.21)], all normalized to the initial value, in correspondence with the evolution of the distortion parameter η. We can clearly identify the time interval when the exponential growth occurs with the matter-unstable phase, when the bar deformation starts to be considerable (η

increases above a few percent) until it is suppressed. Here, the two components of the magnetic energy are drawn separately. This let us realize that indeed the total magnetic energy is mainly dominated by the toroidal part already after 1 ms of evolution, since the poloidal component is almost constant until the bar-mode instability sets in. A magnification of the first 2 ms of the evolution is shown in the inset, to better appreciate the moment when the toroidal component overcomes the poloidal one.

The features presented in this Section allow us to make a list of the combined elements that seem to support the suggestion that the exponential growth in the (toroidal) magnetic field could be the result of the development of an MRI:

- the instability disappears with decreasing resolution (the smallest wavelength needs to be properly resolved);
- the growth rate does not depend on the initial poloidal magnetic field (in the simplest description the growth rate depends only on the local angular velocity);
- the exponential growth is followed by a rapid decay possibly caused by reconnection processes (this behavior was also found in Ref. [34]);
- the exponential growth disappears for sufficiently strong magnetic fields (the bar-mode deformation is no longer the lowest energy state energetically because of the large magnetic-field contribution; besides, $\lambda_{\rm MRI}$ could be of the same order of the stellar radius and in this case the development of the MRI will be inhibited).

However, the resolution employed in these finest resolution simulations ($\Delta x \simeq 380$ m) is considerably coarser than those employed in Ref. [34], and even if in our case we expect the characteristic wavelength $\lambda_{\rm MRI}$ to be about an order of magnitude smaller, it is still difficult to see the appearance of channel-flow structures typical of the MRI [116] and hence to make robust measurements of the wavelengths of the fastest-growing modes.

Anyway, one important feature of models `U11` and `U13` is that they develop pronounced bar-mode deformations (they are further away from the stability threshold in Fig. 5.1) and it is therefore possible that these large deviations from axisymmetry act as an additional trigger, favoring the development of the MRI[1]. This could explain why an exponential growth is seen

[1] We recall that the assumption of axisymmetry is a fundamental one in all perturbative calculations on the MRI and that it is exactly the absence of axisymmetry that allows for the development of dynamos against the limitations of the Cowling theorem [117].

in these models despite the coarse resolution. Besides, when the toroidal magnetic component dominates over the poloidal one, non-axisymmetric MRI modes are supposed to grow much faster and with a much longer characteristic length-scale than that of the axisymmetric MRI [118].

The above-mentioned exponential growth does not seem to be so pronounced in the dynamics of model `U3` for all the different magnetizations considered (cf., the upper-right panel of Fig. 6.7). Although the angular frequency of these models is larger than that of `U11` and `U13` and hence the timescale for the development of the MRI $\tau_{\rm MRI}$ would be correspondingly shorter ($\tau_{\rm MRI} \sim \Omega^{-1}$). The evolutions have been carried out on sufficiently long timescales to allow for the potential appearance of the MRI. This behavior is indeed consistent with the conjecture discussed above, since this class of models is very close to the threshold for the development of the bar-mode instability. As a result, these models experience much smaller bar-mode deformations and maintain a configuration which is more axisymmetric than those found in models `U11` and `U13`. Because these conditions are more similar to those assumed by perturbative MRI analysis, the corresponding predictions are expected to be more accurate. Hence, it is not surprising that almost no MRI is observed in this case simply because no MRI can be seen for these quasi-axisymmetric objects at these resolutions.

Unexpectedly, a hinted exponential growth can be observed in the case of stable models `S7` and `S8` (cf., the upper-left panel of Fig. 6.7), which are quite below the threshold for the onset of the dynamical bar-mode instability and then develop no bar deformation, keeping an axisymmetric configuration for the whole evolution. Anyway, a possible explanation to this behavior could be related to the development of a shear-instability, which can be reasonably expected in models with a much lower value of the instability parameter β than the threshold for the onset of the dynamical bar-mode instability. This instability, if present, could maybe act as an additional trigger for MRI modes to develop, even if the connection between this two phenomena is just a working hypothesis, up to now.

That being said, the MRI is not the only process that would lead to an exponential growth of the magnetic field and, indeed, there is a number of instabilities that can develop in magnetized differentially rotating fluids [119]. For example, the exponentially growing bar-mode deformation could cause sharp increases in local shear and hence an exponential amplification in the magnetic energy. Clearly, additional simulations at even higher resolutions are required to further clarify this point. Indeed, this will be the subject of a future work, which is already ongoing.

Conclusions

We have presented an extensive study of the dynamical bar-mode instability in differentially rotating and magnetized NSs in full general relativity and investigated how the presence of magnetic fields affects the onset and the development of the instability. In order to do that, we have performed 3D ideal-MHD simulations of a large number of stellar models that were already studied in the absence of magnetic fields [10, 11, 37], by adding an initial purely poloidal magnetic field with strengths between 10^{11} and 10^{16} G. In this way, we were able to explore quite extensively the parameter space (β, $\beta_{\rm mag}$) from $\beta = 0.1886$ to 0.2812, determining a threshold for the onset of the instability both in terms of the rotation parameter $\beta = T/|W|$ and of the magnetization parameter $\beta_{\rm mag} = E_{\rm mag}/(T+|W|)$ for each initial matter equilibrium configuration.

We have started our investigation by considering initial stellar models that are bar-mode stable in the absence of magnetic fields. While these are comparatively simpler configurations, the magnetic fields can provide structural changes if sufficiently strong. More specifically, for magnetic fields $\gtrsim 10^{16}$ G, the stellar models are braked considerably in their rotation and evolve into configurations that have uniformly rotating extended cores with large rest-mass densities when compared to the initial values. On the contrary, weaker magnetic fields do not show any significant effect on the evolution of stable models.

When considering initial stellar models that are bar-mode unstable in the absence of magnetic fields, no effects are present on the dynamics of the bar-mode deformation for initial poloidal magnetic fields whose strength is $\ll 10^{15}$ G, with the exact threshold depending on the rotational properties and being higher for slower rotating models. This is not particularly surprising given that in these cases the magnetic energy, even the one produced via magnetic-field shearing, is only a small contribution to the total energy of the system. For stronger initial magnetic fields, the corrections introduced by the magnetic tension become quite large. In particular, below a critical $\beta_{\rm mag}$, the development of the instability is modified, showing growth

rates and bar-mode distortions that become smaller with increasing magnetic fields. Above a critical $\beta_{\rm mag}$, on the other hand, the instability is totally suppressed as the enormous magnetic tension cannot be overcome by the differential rotation. Under these conditions, the star sheds its outer layers leading to an extended, axisymmetric object with a high, uniform-density core and a low-density, slowly rotating envelope.

On the basis of the phenomenology discussed above, and after carrying-out a large number of simulations, we were able to locate in the (β, $\beta_{\rm mag}$) diagram the region in which the values of the rotational and magnetic energies are sufficient to give rise to the development a dynamical bar-mode instability. In this sense, our study confirms the Newtonian results of [20] and extends them to a general-relativistic framework and to a more generic range of initial conditions. Moreover, our previous work on the effects of magnetic fields on the dynamical bar-mode instability [38, 39] has been extended, providing a more detailed and accurate description on the different phases of the evolution of both bar-stable and bar-unstable stellar models.

In all cases considered, the differential rotation shears the poloidal magnetic field, generating a toroidal component that grows linearly in time, and which soon provides the largest contribution to the total electromagnetic energy on a timescale of the order of 1 ms. At later times, this growth starts deviating from the linear behavior and the magnetic tension produced by the very large magnetic-field winding alters the angular velocity profile of the star. A sudden exponential growth of the toroidal component of the magnetic field is observed during the matter-unstable phase of the evolution of bar-unstable models, resembling the evolution described in Ref. [34]. This feature in the dynamics was first observed in [38, 39], therefore in the present Thesis we tried to get a deeper insight on the possible development of the MRI in bar-unstable models by performing a number of additional simulations with a finer resolution, focusing our attention on the evolution of the most bar-unstable model, namely `U13`. Actually, we were able to recognize some of the typical features one would expect in the case of an MRI acting on the evolved stellar models. We provided a possible explanation for these observations, involving the growth of non-axisymmetric MRI modes which could be triggered by the deformation due to the onset of the matter instability. Nevertheless, the resolution of these more accurate simulations is still much coarser than the one employed in Ref. [34], and then a deeper and more extended analysis of this topic has not been feasible by the time of the present Thesis, mainly due to computational limitations.

As a final remark we note that although we have restricted our attention to a simplified EOS, our results also point out that it is unlikely that very highly magnetized NSs can develop the dynamical bar-mode instability and hence be considered as strong sources of GWs, and that the magnetic field can undergo an amplification of about an order of magnitude in the initial phase of the evolution due to differential rotation, and of a further factor of 5 due to the onset of the dynamical bar-mode instability.

ACKNOWLEDGEMENTS

Acknowledgments

This research would not have been possible without the support of computational resources provided by the European Union 6th Regular Call of the "Partnership for Advanced computing in Europe" (PRACE) through the grant "3DMagRoI : High-resolution 3D study of MRI in relativistic rotating stars", that provided 25.000.000 core hours of computing time on the CINECA "Fermi" system. Additional high performance computational (HPC) resources were provided by the Louisiana State University (allocations hpc_cactus, hpc_numrel and hpc_hyrel), by the Louisiana Optical Network Initiative (allocations loni_cactus and loni_numrel), by the INFN "Theophys" cluster and through the allocation of CPU time for the INFN "SUMA" project. Moreover, in the initial stage of the project, HPC resources were provided by the Albert-Einstein Institute and through the PRACE allocation "pr32pi" on "SuperMUC" at the "Leibniz-Rechenzentrum".

First of all, I would really like to thank my advisor, Roberto De Pietri, for welcoming me in Parma and providing me all the resources I needed for my PhD. He always pushed me to work harder and better. Besides, he allowed me to travel a lot, all over Europe and beyond, visiting many institutions and attending interesting schools and conferences. I couldn't have asked for more.

I thank Alessandra Feo, the other member of the Parma Gravitational Physics Group, who has always been kind to me and very well-disposed, both professionally and personally. Besides being an excellent physicist and collaborator, she was indeed indispensable in more than one occasion, keeping us on the right track, helping us dealing with deadlines and people and, least but not last, with English!

I owe my sincere gratitude to Enrico Onofri, who supported me since the very first day I came to Parma, and to Pier Paolo Lottici, who really helped me in my time of need.

ACKNOWLEDGEMENTS

During my travels I met a lot of people, estimated colleagues that sometimes also became friends. I'd really like to thank all of them!

I thank Luciano Rezzolla and Kyriaki Dionysopoulou, who were precious collaborators for my PhD project and helped me with many in-person and Skype conversations, suggestions and corrections. Thank you for your kind and generous hospitality every time I came to Potsdam, which I love. I also take the chance to thank all the people from the Max Plank Institute, who always made me feel comfortable during my visits, especially Riccardo Ciolfi and Daniel Siegel who also helped me with enlightening discussions.

I really thank Frank Löffler, qualified and very hard-working collaborator and a very nice person. Thanks for the help with the code and for time allocation on your machines, but thank you even more for the warm welcome in Baton Rouge and for the ride to Mississippi! I'd also like to thank Peter Diener for his suggestions about physics and for keeping us company during that amazing week in Louisiana, for the lunches and dinners in typical Cajun places on the Bayou.

I'm grateful to Sebastiano Bernuzzi, whom I met in many different places, from Parma to Jena, from Amsterdam to Warsaw, and always gave me many and many pieces of advices about physics but also about life choices. I really thank him for asking me to work together and for strongly supporting my application for a long-term visit in Jena. I also thank all the people from the Jena Group, in particular Andreas Weyhausen and Bernd Brügmann, who always showed me a very kind hospitality.

I'd like to thank CINECA, Elda Rossi and all the people from the SCAI Department for letting me attend their interesting courses and schools and for hosting me for a 3-months internship there. Thanks also for your technical support and for your help with our PRACE project. In particular, I'd really like to thank Marzia Rivi for always believing in me and in my skills, for helping me and for not giving up on me every time I disappeared for a while, due to pressing commitments regarding my PhD or to family issues. I also thank Filippo Spiga, who has always been willing to help me with my GPU project.

I really want to thank Luca Del Zanna, the very first person who believed in me as an astrophysicist when I was still an undergraduate student and never stopped doing it. I wouldn't have gone so far if it wasn't for him. I definitely owe him a lot, and I guess I'll never stop owing him! I also thank Niccoló Bucciantini for many interesting discussions and suggestions, hoping that many others will come.

Ringrazio tutti i ragazzi del Dipartimento di Fisica dell'Universitá di Parma, che hanno condiviso con me una parte piú o meno lunga di questi tre anni di dottorato. Sono passato all'Italiano, perchè questo è il suono del tempo trascorso con voi! In particolare, un doveroso, sentito e sincero grazie va al dottorando emerito Alessio Camobreco, il primo che mi ha accolto in ufficio e che col suo pur ben celato accento toscano mi ha fatto sentire come a casa fin dal primo momento. Un grande grazie anche agli altri due folli che hanno condiviso con me l'ufficio dottorandi HARD nel mio primo periodo a Parma, tali Riccardo Campari e Daniele Marmiroli, adesso in giro per il mondo in cerca di quella fortuna che meritano. Un grazie davvero particolare ai loro degni(?) successori, Stefano Mori e Laura Taddei, che mi hanno fatto compagnia in ufficio nel periodo per certi versi piú delicato e difficile, ed hanno sopportato tutte le mie crisi e lamentele porgendo l'altra guancia, da buon cattolico, l'uno e contrattaccando colpo su colpo l'altra! Ricorderó sempre con nostalgia, tra le altre cose, le lunghe, estenuanti ed inconcludenti discussioni sulla religione tra Alessio e Stefano, ed i siparietti stile Casa Vianello tra Alessio e Laura. Una menzione anche per gli ultimi due arrivati, Enrico Ubaldi e Michelangelo Preti, anche se purtroppo non abbiamo passato insieme tutto il tempo che avremmo potuto, ma come si suol dire è stato breve ma intenso. Un saluto affettuoso ed un grazie anche a tutti i colleghi degli altri uffici e laboratori, nonchè compagni di pranzi, cene, partite di pallavolo e di ping pong! Non vi nomino tutti per non rischiare di dimenticare qualcuno, data l'ora tardissima alla quale sto scrivendo, ma non me ne vogliate, vi ho tutti nel cuore. Chiudo la carrellata con un sentito grazie ed un abbraccio a Max Zanichelli, Michele Brambilla e Dirk Hesse. Voi ci siete sempre stati per me nel momento del bisogno, con una parola di conforto, un incoraggiamento, un aiuto, un consiglio. Tante parole non servono, quindi vi dico solo che ve ne saró per sempre grato!

Prima di chiudere, ci tengo a ringraziare di cuore il mio disgraziato coinquilino Roberto Dario, per avermi supportato e soprattutto sopportato negli ultimi due anni. Avere un vero amico a fianco in quest'ultimo, difficile periodo è stato fondamentale e senza di lui sarebbe stato tutto molto piú difficile da affrontare.

Per ultimi, ma primi nei miei pensieri, voglio rigraziare dal piú profondo del cuore i miei genitori, Lucia e Giovanni, per non avermi mai fatto mancare nulla in tutti questi anni, avermi sempre sostenuto, incoraggiato, consolato, consigliato ma lasciato libero di fare le mie scelte. Se sono arrivato a questo punto lo devo soltanto a voi. Non ricambieró mai abbastanza quello che avete fatto per me. Vi voglio bene.

Appendix

The WhyskyMHD code employed in this Thesis has been tested in a number of different scenarios and its accuracy has already been explicitly reported in various works [24, 92, 93]. Nevertheless, we have performed additional tests to check that the specific settings we used are sufficient to capture the main properties of the evolved systems.

The role of symmetries

As discussed in Sect. 3.1, all of the results presented here about the dynamics of the bar-mode instability in magnetized relativistic stars were achieved with a spatial resolution $\Delta x = 0.375\, M_\odot \simeq 0.550$ km on the finest grid and exploiting a "bitant symmetry", i.e., a reflection symmetry with respect to the (x, y) plane. While this choice obviously reduces the computational costs by a factor two, it is important to verify that it does not introduce systematic effects and that all the results would be unchanged if this symmetry was suppressed. For this purpose, we have evolved the bar-mode unstable model U11 when threaded by an initially moderate magnetic field, i.e., model U11-1.0e15, both when imposing the bitant symmetry and when evolving the equations in the full domain. In Fig. 6.9 we report the evolution of the distortion parameters η_+ (top panel) and η (bottom panel) for model U11-1.0e15. In particular, the figure offers a comparison between a simulation using the bitant symmetry (red dot-dashed line) and one using the full domain (black solid line), both performed at the reference resolution of $\Delta x = 0.550$ km on the finest grid. Clearly, no significant differences can be observed between the two cases during the first 25 ms of evolution, and so no spurious or unphysical effects due to the imposed symmetry were introduced. The same conclusion holds for all quantities related to the magnetic field, since they have been also monitored. This result fully justifies our choice to perform all the simulations presented here imposing bitant symmetry.

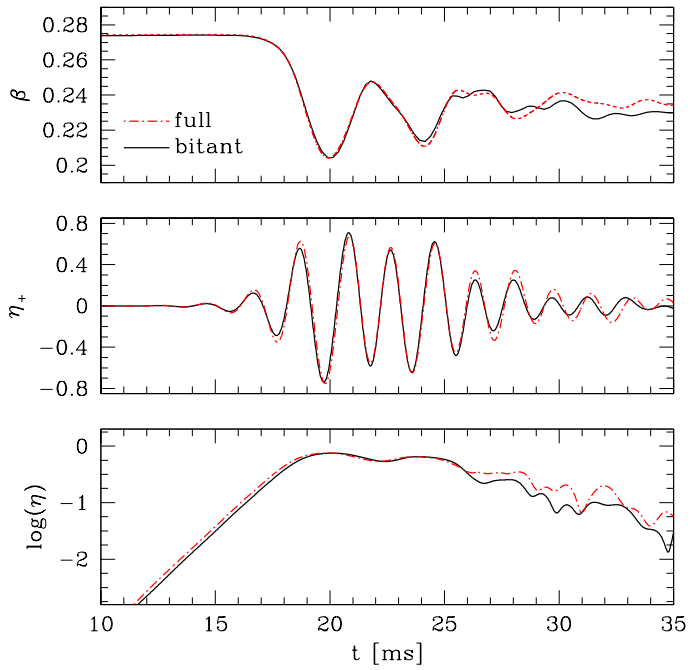

Figure 6.9: Evolution of the rotation parameter β (top panel) and of the distortion parameters η_+ (middle panel) and η (bottom panel) for model `U11-1.0e15` when imposing a bitant symmetry (black solid line) or when using the full domain (red dot-dashed line).

The role of resolution and convergence

Furthermore, we have performed a few simulations of the same model varying the resolution of more than a factor of two, that is, with the finest grid having resolutions between $\Delta x = 0.370$ km and 0.920 km.

For all these runs we computed the growth rate, $\tau_{\rm bar}$, and the frequency, $f_{\rm bar}$, of the bar-mode instability. The results of this extensive series of tests are reported in Table 6.1) and show that these quantities do not depend on resolution within the accuracy of our estimate. Hence, we conclude that all of the results have been achieved at sufficient resolution to extract physically significant information.

Determining the convergence properties of our simulations is of course an essential validation of the results presented and a considerable effort has been put into performing these measures within the numerical setup used here. Lacking an analytic solution that describes the fully nonlinear development of the bar, we can only perform self-convergence tests at this stage. However, there is a regime in our calculations in which we can exploit the knowledge of an analytic solution and this refers to the initial shearing of the poloidal magnetic field by the dif-

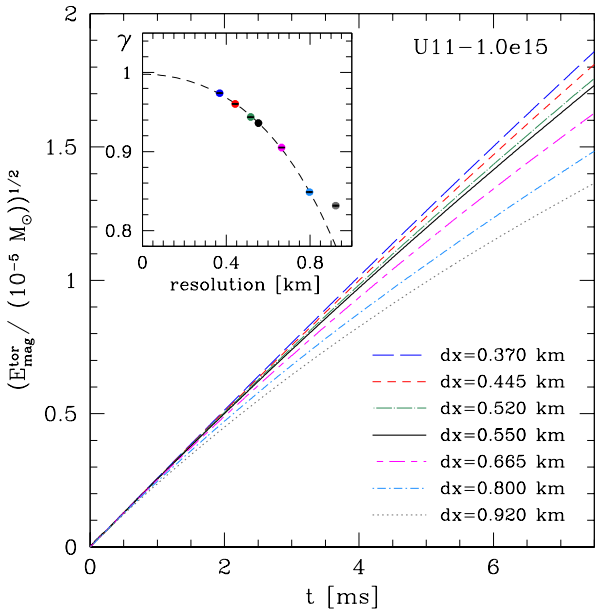

Figure 6.10: Initial growth of the square root of the toroidal component of the magnetic energy $E_{\rm mag}^{\rm tor}$ [Eq. (3.20)] for different resolutions of the finest grid. The reference resolution, $\Delta x \simeq 0.550$ km, is shown with a black solid line. The inset shows instead the growth rate γ as a function of the resolution and its fit with a quadratic function (dashed line). Note that the expected value $\gamma = 1$ is approached in the limit of $\Delta x \to 0$.

Δx $[M_\odot]$	Δx [km]	symmetry symmetry	$\eta_{\rm max}$	$\tau_{\rm bar}$ [ms]	$f_{\rm bar}$ [Hz]
0.250	0.370	bitant	0.743	$1.15^{+0.01}_{-0.01}$	491^{+1}_{-1}
0.350	0.445	bitant	0.746	$1.16^{+0.03}_{-0.03}$	492^{+1}_{-1}
0.375	0.520	bitant	0.751	$1.17^{+0.04}_{-0.05}$	491^{+2}_{-4}
0.375	0.520	full	0.753	$1.14^{+0.01}_{-0.01}$	490^{+3}_{-2}
0.450	0.665	bitant	0.745	$1.18^{+0.03}_{-0.05}$	489^{+2}_{-2}
0.540	0.800	bitant	0.754	$1.19^{+0.05}_{-0.05}$	487^{+3}_{-5}
0.625	0.920	bitant	0.743	$1.20^{+0.11}_{-0.05}$	484^{+2}_{-7}

Table 6.1: Main properties of the bar-mode instability for model `U11-1.0e15` at different resolutions. Here we report the resolution in terms of solar masses and kilometers, the symmetry we imposed to the computational domain, the maximum value of the distortion parameter η, the growth times $\tau_{\rm bar}$ and the frequencies $f_{\rm bar}$ of the bar-mode deformation.

ferentially rotating star. It is in fact not difficult to show that within an ideal-MHD framework the induction equation predicts a growth of the toroidal magnetic field which is linear in time (see, for instance, [120] for a pedagogic presentation of the perturbed induction equation). To explore this regime we have performed a large number of simulations of model `U11-1.0e15` with varying resolution and monitored the growth of the square root of the toroidal magnetic energy $E^{\rm tor}_{\rm mag}$ [cf., Eq. (3.20]; we recall that the poloidal magnetic field is not expected to grow during this stage (cf., Sect. 6).

Figure 6.10 reports the results of these simulations relatively to the first $\sim$ 7 ms, with different curves referring to different resolutions. It is then evident that the curves are getting closer and closer to straight lines as the resolution increases. To measure whether a linear-in-time-growth is actually reached we have actually computed the growth rate "γ" by fitting the square root of the magnetic energy with a trial function which is a power-law in time with undetermined growth rate, i.e., with

$$\sqrt{E^{\rm tor}_{\rm mag}(t)} = y(t) = y_0 + m\, t^{\gamma}\,, \tag{6.3}$$

where the time interval has been selected to be between 0.2 to 5 ms.

Also reported in the inset of Fig. 6.10 are the values of γ (colored symbols) as a function of the resolution Δx, as well as a fit for $\gamma(\Delta x)$ (dashed line) when assuming a second-order convergence with resolution, i.e., assuming $\gamma(\Delta x) = \gamma|_{\Delta x=0} + k\,\Delta x^2$ (the point for $\Delta x = 0.920$ km has been excluded from the fit). Having made this assumption, we do find that the growth rate is in very good agreement with the one expected in this linear regime, with $\gamma|_{\Delta x=0} = 1 \pm 0.005$. Of course this result does not prove directly that we have second-order convergence over this period of time. However, what it does prove is that if a second-order convergence is assumed, then our solution matches the expected perturbative one.

Next we consider a more general calculation of the convergence order by performing again simulations of model `U11-1.0e15` for a range of resolutions. This time our results for the convergence are obtained by taking into account the data corresponding to the whole timescale of the simulations, i.e., $\sim$ 25 ms. Also in this case we monitor the growth of the toroidal magnetic energy $E^{\rm tor}_{\rm mag}$ and report in the top panel of Fig. 6.11 its evolution for three runs at resolutions: $\Delta x = 0.370$, 0.550, and 0.665 km, respectively. The bottom panel of the same figure reports instead the convergence order γ_c, computed via a self-convergence test [105], when shown as a function of time.

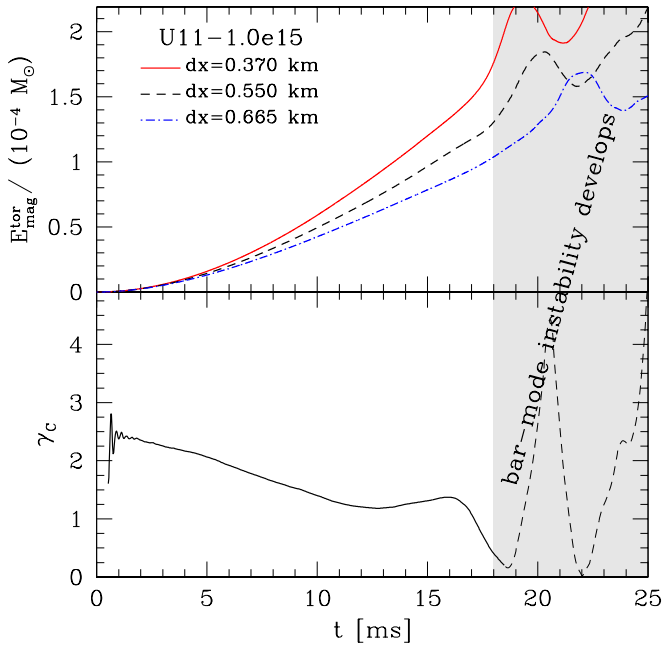

Figure 6.11: *Top panel:* evolution of the toroidal component of the magnetic energy $E^{\rm tor}_{\rm mag}$ for three different resolutions. *Bottom panel:* order of the self-convergence test, γ_c, shown as a function of time. Note that a convergence order around 2 is measured before the bar-mode instability develops and shocks are produced (gray-shaded area).

In this case it is then possible to recognize that the code does indeed converge at around second order during the linear growth stage (i.e., for $t \lesssim 5$ ms), in agreement with the results found in purely hydrodynamical simulations [121], or with the new resistive code [40]. However, as the bar-mode instability develops, the second-order convergence is lost and the convergence order reduces to one. This is not surprising as the development of the bar also leads to the formation of shocks, which necessarily degrade our solution to a first-order convergence. We also note that the large variations in the convergence order shown in the gray-shaded area of Fig. 6.11 (i.e., for $t \gtrsim 18$ ms) are simply the consequence of the fact that the instability starts growing at different times for different resolutions and this inevitably leads to large excursions in γ_c. Because all the major considerations made about the onset and development of the bar deformation, as well as the estimates for the growth rates and frequencies, are obtained after looking at the first 20 ms of the evolution, we conclude that all of our results have been achieved with solutions converging at the expected rates.

An extensive view on the evolution `U11` magnetized models

In the following few pages, we report quite an extensive view on the dynamics of almost all magnetized models of the `U11` sequence, both regarding the evolution of matter and of the magnetic field. In particular, from top to bottom, the four panels show for each model:

- the time evolution of the total magnetic energy $E_{\rm mag}$, of its toroidal component $E^{\rm tor}_{\rm mag}$ [Eq. (3.20)] and its poloidal component $E^{\rm pol}_{\rm mag}$ [Eq. (3.21)], all normalized to the total (i.e., poloidal) initial value;
- the time evolution of the distortion parameter η_+;
- the time evolution of the distortion parameter η;
- the time evolution of the instability parameter β.

Moreover, for all bar-unstable models, two red dot-dashed vertical lines mark the interval in which the distortion η ranges from 1% of the maximum and the maximum itself, i.e., the matter-unstable phase.

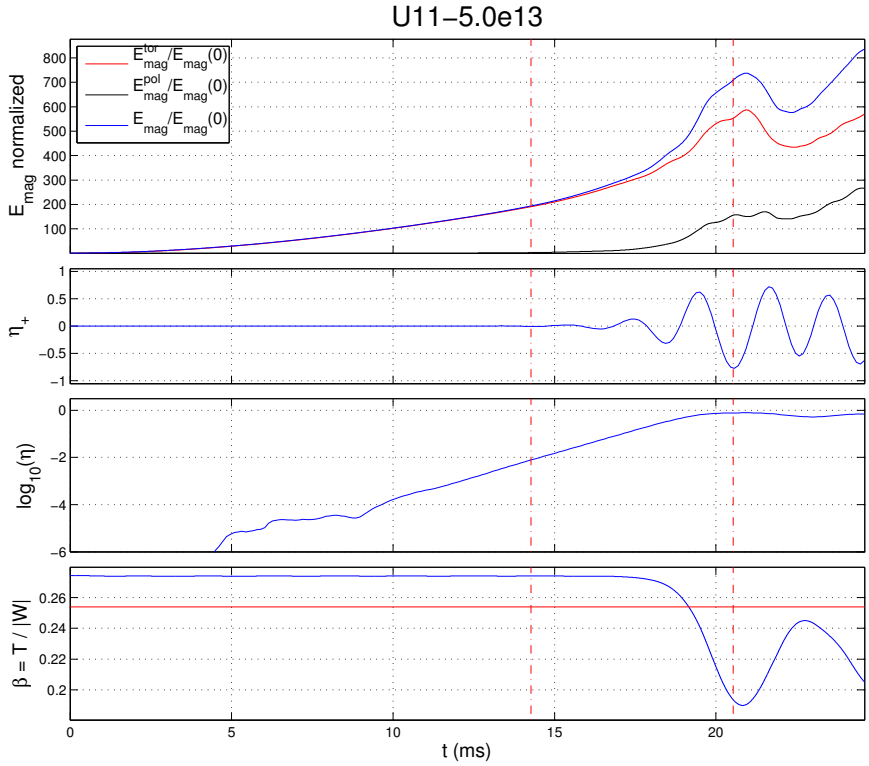

Figure 6.12: Dynamics of model `U11-5.0e13`.

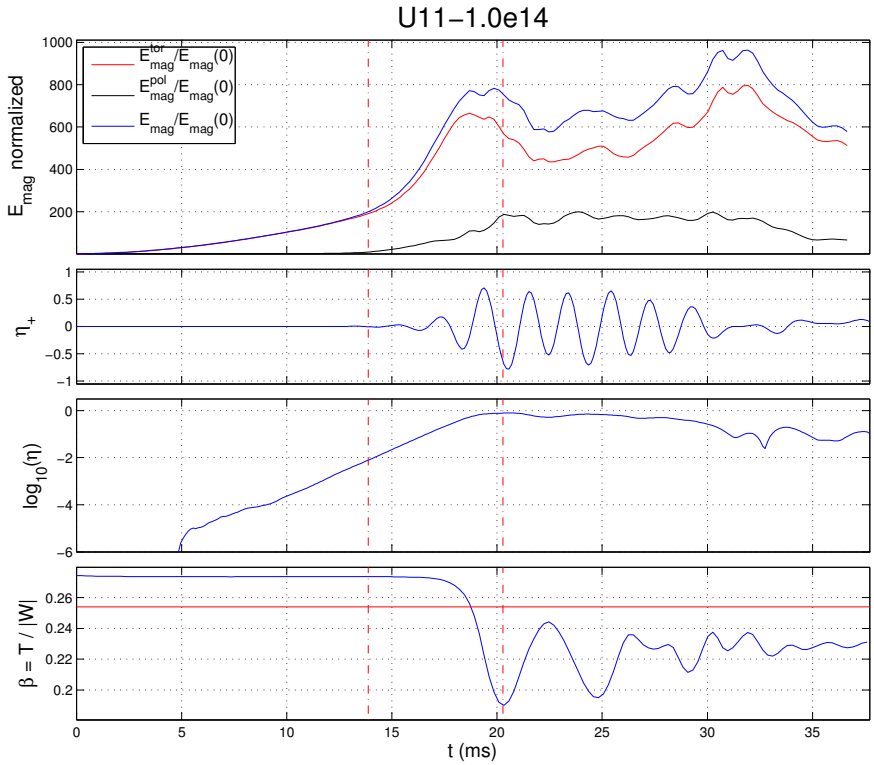

Figure 6.13: Dynamics of model `U11-1.0e14`.

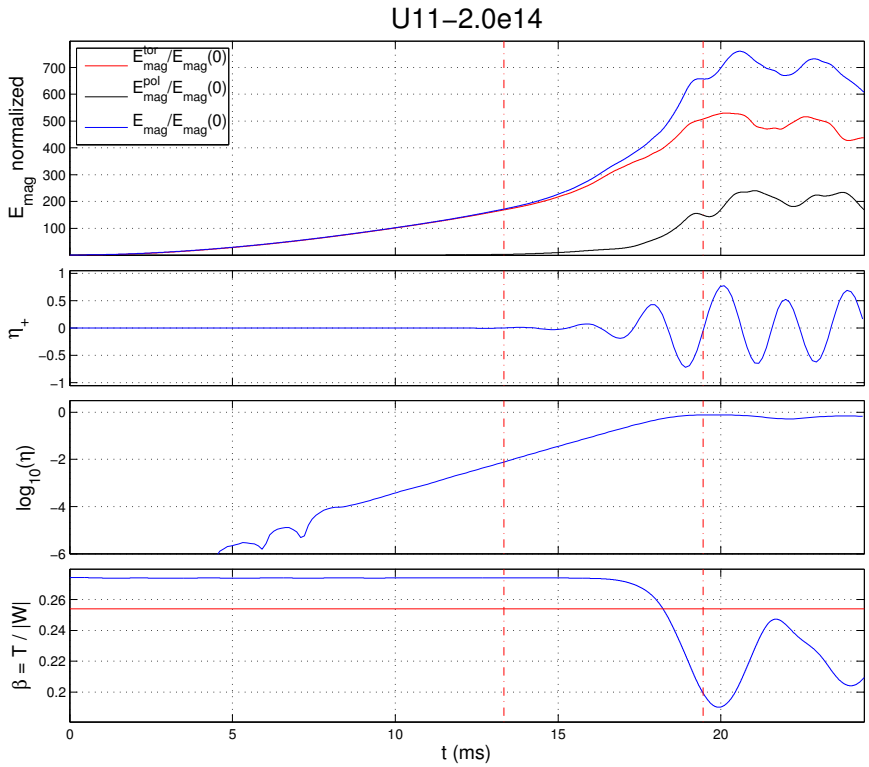

Figure 6.14: Dynamics of model `U11-2.0e14`.

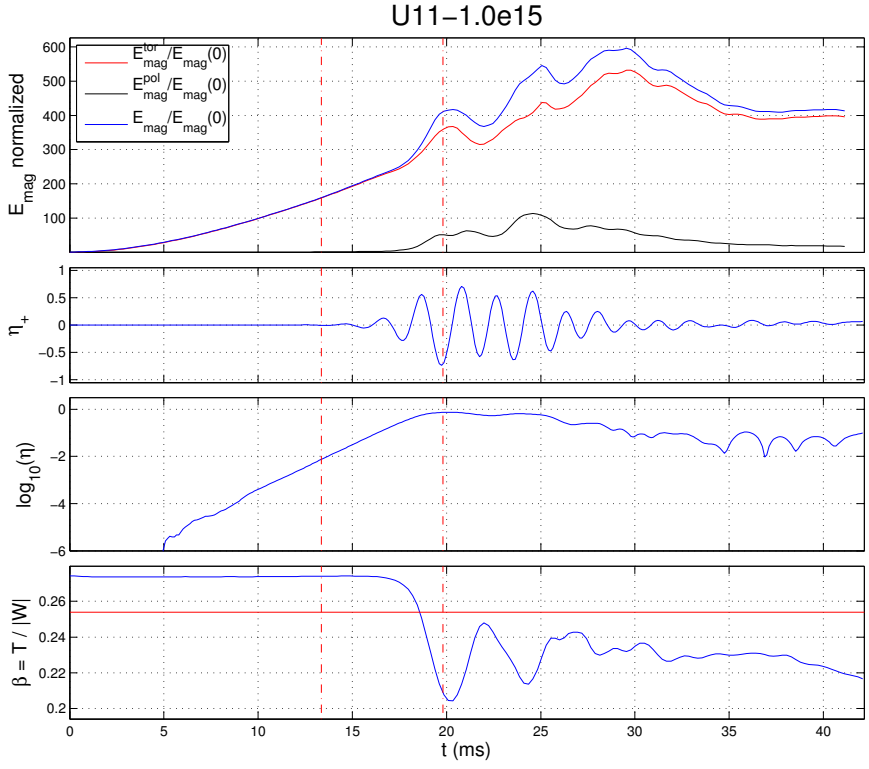

Figure 6.15: Dynamics of model `U11-1.0e15`.

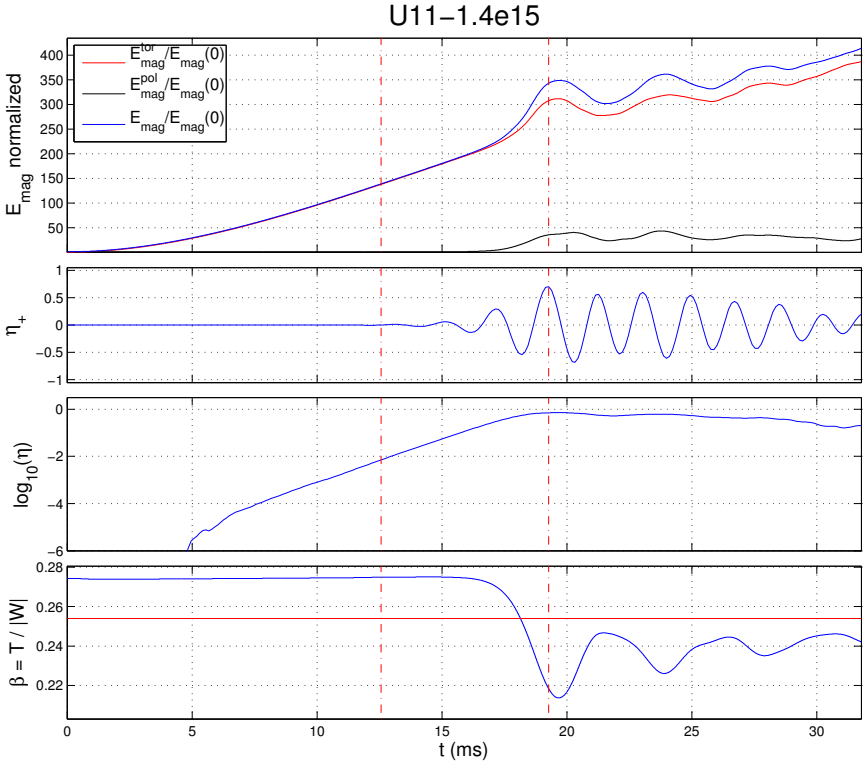

Figure 6.16: Dynamics of model `U11-1.4e15`.

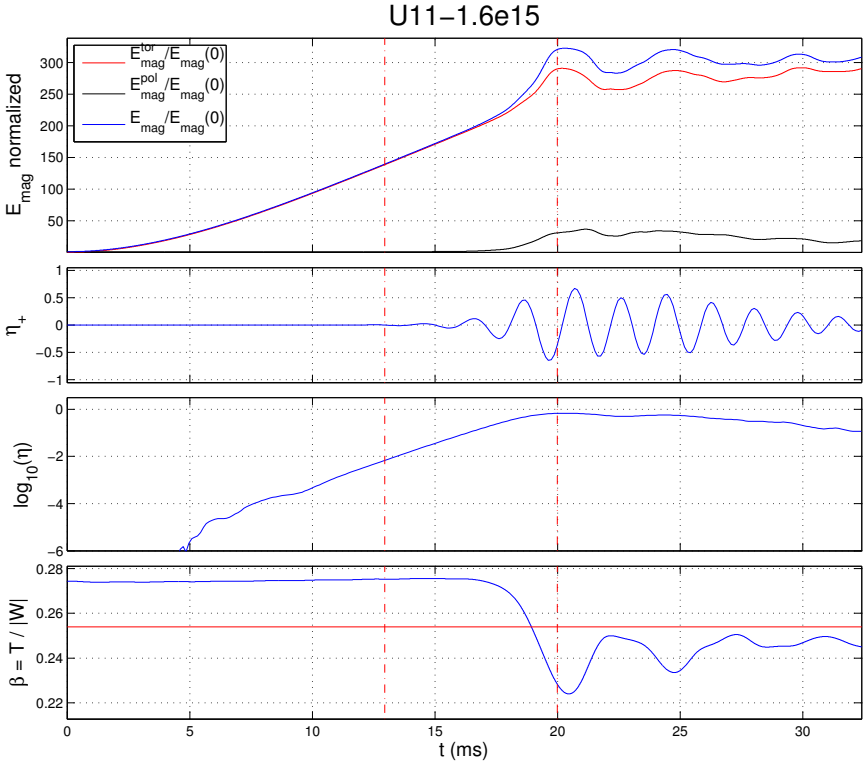

Figure 6.17: Dynamics of model `U11-1.6e15`.

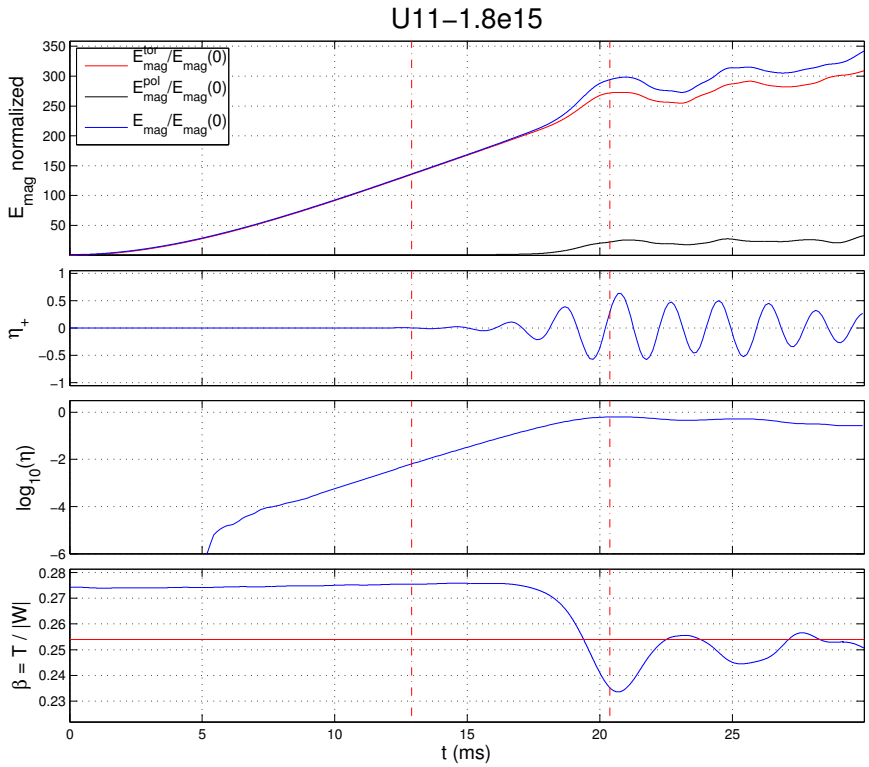

Figure 6.18: Dynamics of model `U11-1.8e15`.

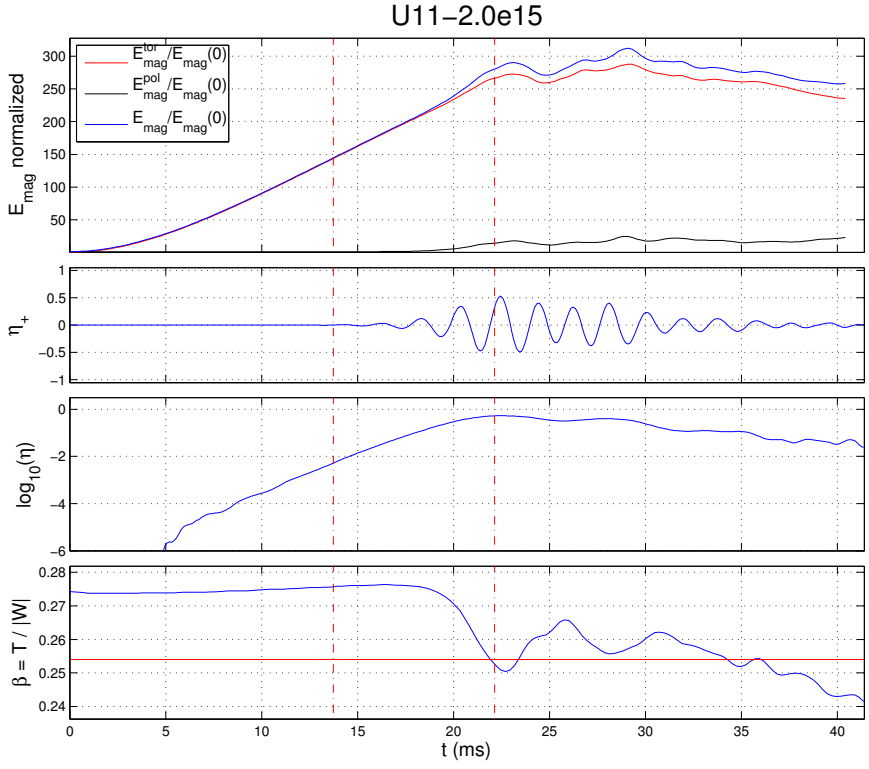

Figure 6.19: Dynamics of model `U11-2.0e15`.

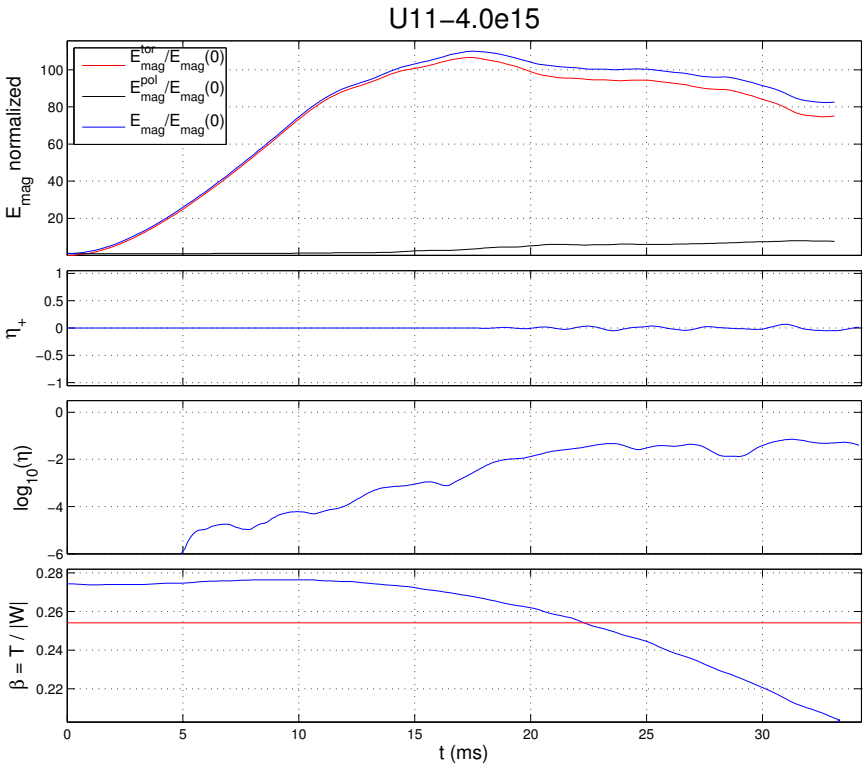

Figure 6.20: Dynamics of model `U11-4.0e15`.

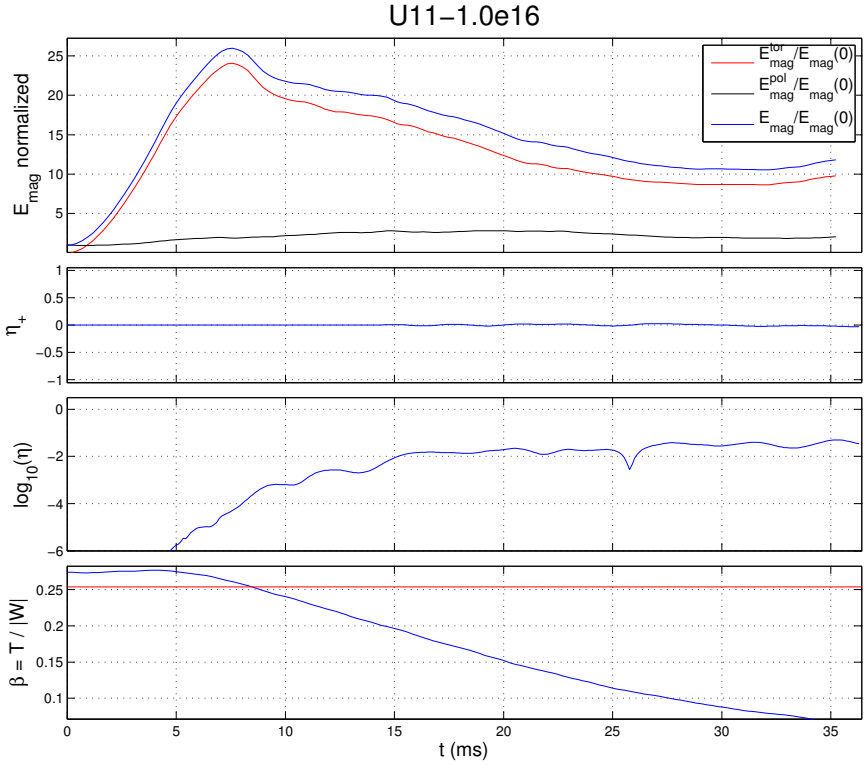

Figure 6.21: Dynamics of model `U11-1.0e16`.

Bibliography

[1] S. E. Woosley, A. Heger, and T. A. Weaver. The evolution and explosion of massive stars. *Rev. Mod. Phys.*, 74:1015, November 2002. v

[2] A. Heger, C. L. Fryer, S. E. Woosley, N. Langer, and D. H. Hartmann. How Massive Single Stars End Their Life. *Astrophys. J.*, 591:288–300, July 2003. v

[3] Y. T. Liu and L. Lindblom. Models of rapidly rotating neutron stars: remnants of accretion-induced collapse. *Mon. Not. R. Astron. Soc.*, 324:1063–1073, July 2001. v

[4] C. Fryer, W. Benz, M. Herant, and S. A. Colgate. What Can the Accretion-induced Collapse of White Dwarfs Really Explain? *Astrophys. J.*, 516:892–899, May 1999. v

[5] Nikolaos Stergioulas. Rotating stars in relativity. *Living Rev. Relativ.*, 6:3, 2003. v

[6] N. Andersson. Topical Review: Gravitational waves from instabilities in relativistic stars. *Classical Quantum Gravity*, 20:105, April 2003. v

[7] S Chandrasekhar. *Ellipsoidal Figures of Equilibrium*. Yale Univ. Press, New Haven, 1969. v

[8] A. L. Watts, Nils Andersson, and D. I. Jones. The nature of low $T/|W|$ dynamical instabilities in differentially rotating stars. *Astrophys. J.*, 618:L37, 2005. v, 8

[9] Masaru Shibata, Thomas W. Baumgarte, and Stuart L. Shapiro. The bar-mode instability in differentially rotating neutron stars: Simulations in full general relativity. *Astrophys. J.*, 542:453–463, 2000. v

[10] Luca Baiotti, Roberto De Pietri, Gian Mario Manca, and Luciano Rezzolla. Accurate simulations of the dynamical bar-mode instability in full general relativity. *Phys. Rev. D.*, 75:044023, 2007. v, vi, vii, 9, 11, 24, 27, 30, 35, 50, 83

[11] Gian Mario Manca, Luca Baiotti, Roberto De Pietri, and Luciano Rezzolla. Dynamical non-axisymmetric instabilities in rotating relativistic stars. *Classical Quantum Gravity*, 24:S171–S186, 2007. v, vii, 27, 83

[12] G. Corvino, L. Rezzolla, S. Bernuzzi, R. De Pietri, and B. Giacomazzo. On the shear instability in relativistic neutron stars. *Classical Quantum Gravity*, 27(11):114104, June 2010. v, 8

[13] M. Saijo and Y. Kojima. Faraday resonance in dynamical bar instability of differentially rotating stars. *Phys. Rev. D*, 77:063002, February 2008. vi, 9

[14] C. Thompson and R. C. Duncan. Neutron star dynamos and the origins of pulsar magnetism. *Astrophys. J.*, 408:194–217, May 1993. vi

[15] Alfio Bonanno, Luciano Rezzolla, and Vadim Urpin. Mean-field dynamo action in protoneutron stars. *Astron. Astrophys.*, 410:L33, 2003. vi

[16] P. D. Lasky, B. Zink, K. D. Kokkotas, and K. Glampedakis. Hydromagnetic Instabilities in Relativistic Neutron Stars. *Astrophys. J.*, 735:L20, July 2011. vi

[17] R. Ciolfi, S. K. Lander, G. M. Manca, and L. Rezzolla. Instability-driven Evolution of Poloidal Magnetic Fields in Relativistic Stars. *Astrophys. J.*, 736:L6, July 2011. vi

[18] R. Ciolfi and L. Rezzolla. Poloidal-field Instability in Magnetized Relativistic Stars. *Astrophys. J.*, 760:1, November 2012. vi

[19] P. D. Lasky, B. Zink, and K. D. Kokkotas. Gravitational Waves and Hydromagnetic Instabilities in Rotating Magnetized Neutron Stars. *arXiv:1203.3590*, March 2012. vi

[20] Karen D. Camarda, Peter Anninos, P. Chris Fragile, and Jose A. Font. Dynamical Bar-Mode Instability in Differentially Rotating Magnetized Neutron Stars. *Astrophys. J.*, 707:1610–1622, 2009. vi, 13, 84

[21] B. Paczynski. Gamma-ray bursters at cosmological distances. *Astrophys. J. Lett.*, 308:L43–L46, September 1986. vi

[22] D. Eichler, M. Livio, T. Piran, and D. N. Schramm. Nucleosynthesis, neutrino bursts and gamma-rays from coalescing neutron stars. *Nature*, 340:126–128, July 1989. vi

[23] R. Narayan, B. Paczynski, and Tsvi Piran. Gamma-ray bursts as the death throes of massive binary stars. *Astrophys. J.*, 395:L83, 1992. vi

[24] L. Rezzolla, B. Giacomazzo, L. Baiotti, J. Granot, C. Kouveliotou, and M. A. Aloy. The missing link: Merging neutron stars naturally produce jet-like structures and can power short Gamma-Ray Bursts. *Astrophys. J.*, 732(11):L6, May 2011. vi, 23, 91

[25] Ehud Nakar. Short-hard gamma-ray bursts. *Phys. Rep.*, 442:166–236, 2007. vi

[26] William H. Lee and Enrico Ramirez-Ruiz. The Progenitors of Short Gamma-Ray Bursts. *New J. Phys.*, 9:17, 2007. vi

[27] L. Baiotti, B. Giacomazzo, and L. Rezzolla. Accurate evolutions of inspiralling neutron-star binaries: Prompt and delayed collapse to a black hole. *Phys. Rev. D*, 78(8):084033, October 2008. vi

[28] L. Rezzolla, L. Baiotti, B. Giacomazzo, D. Link, and J. A. Font. Accurate evolutions of unequal-mass neutron-star binaries: properties of the torus and short GRB engines. *Classical Quantum Gravity*, 27(11):114105, June 2010. vi, 54, 58

[29] N. Bucciantini, B. D. Metzger, T. A. Thompson, and E. Quataert. Short gamma-ray bursts with extended emission from magnetar birth: jet formation and collimation. *Mon. Not. R. Astron. Soc.*, 419:1537–1545, January 2012. vi

[30] B. Zhang. Early X-Ray and Optical Afterglow of Gravitational Wave Bursts from Mergers of Binary Neutron Stars. *Astrophys. J.*, 763:L22, January 2013. vi

[31] M. Shibata, Y. Suwa, K. Kiuchi, and K. Ioka. Afterglow of a Binary Neutron Star Merger. *Astrophys. J.l*, 734:L36, June 2011. vi

[32] K. Kiuchi, K. Kyutoku, and M. Shibata. Three-dimensional evolution of differentially rotating magnetized neutron stars. *Phys. Rev. D*, 86(6):064008, September 2012. vi

[33] Matthew D. Duez, Yuk Tung Liu, Stuart L. Shapiro, Masaru Shibata, and Branson C. Stephens. Evolution of magnetized, differentially rotating neutron stars: Simulations in full general relativity. *Phys. Rev. D*, 73:104015, 2006. vi, 77

[34] D. M. Siegel, R. Ciolfi, A. I. Harte, and L. Rezzolla. Magnetorotational instability in relativistic hypermassive neutron stars. *Phys. Rev. D R*, 87(12):121302, June 2013. vi, viii, 76, 78, 81, 84

[35] V.P. Velikhov. *Sov. Phys. JETP*, 36:995, 1959. vi

[36] S. Chandrasekhar. The Stability of Non-Dissipative Couette Flow in Hydromagnetics. *Proc. Natl. Acad. Sci.*, 46:253–257, February 1960. vi

[37] Roberto De Pietri, Luca Baiotti, Gian Mario Manca, and Luciano Rezzolla. Accurate simulations of the barmode instability in general relativity. In Lysiane Mornas and Joaquin Diaz Alonso, editors, *XXVIII Spanish Relativity Meeting (ERE 2005)*, volume 841, Oviedo, 2007. AIP Conference Proceedings. vii, 83

[38] L. Franci, R. De Pietri, K. Dionysopoulou, and L. Rezzolla. Dynamical bar-mode instability in rotating and magnetized relativistic stars. *Phys. Rev. D*, 88(10):104028, November 2013. vii, viii, 84

[39] L. Franci, R. De Pietri, K. Dionysopoulou, and L. Rezzolla. Bar-mode instability suppression in magnetized relativistic stars. *Journal of Physics Conference Series*, 470(1):012008, December 2013. vii, viii, 84

[40] K. Dionysopoulou, D. Alic, C. Palenzuela, L. Rezzolla, and B. Giacomazzo. General-Relativistic Resistive Magnetohydrodynamics in three dimensions: formulation and tests. *arXiv:1208.3487, in press*, August 2013. vii, 95

[41] J. W. T. Hessels, S. M. Ransom, I. H. Stairs, P. C. C. Freire, V. M. Kaspi, and F. Camilo. A Radio Pulsar Spinning at 716 Hz. *Science*, 311:1901–1904, March 2006. 1

[42] R.N. Manchester and J.H. Taylor. *Pulsars*. W.H. Freeman, San Francisco, 1977. 2

[43] Sandro Mereghetti. X-ray emission from isolated neutron stars. In Diego F. Torres and Nanda Rea, editors, *High-Energy Emission from Pulsars and their Systems*, Astrophysics and Space Science Proceedings, pages 345–363. Springer Berlin Heidelberg, 2011. 2

[44] S. Chandrasekhar. *Ellipsoidal Figures of Equilibrium*. Yale University Press, New Haven, USA, 1969. revised edition 1987. 7, 9

[45] Masaru Shibata, Shigeyuki Karino, and Yoshiharu Eriguchi. Dynamical instability of differentially rotating stars. *Mon. Not. R. Astron. Soc.*, 334:L27, 2002. 8

[46] Masaru Shibata, Shigeyuki Karino, and Yoshiharu Eriguchi. Dynamical bar-mode instability of differentially rotating stars: Effects of equations of state and velocity profiles. *Mon. Not. R. Astron. Soc.*, 343:619, 2003. 8

[47] Christian D. Ott, Shangli Ou, Joel E. Tohline, and Adam Burrows. One-armed spiral instability in a slowly rotating, post- bounce supernova core. *Astrophys. J.*, 625:L119–L122, 2005. 8

[48] S. Ou and J. E. Tohline. Unexpected Dynamical Instabilities in Differentially Rotating Neutron Stars. *Astrophys. J.*, 651:1068, November 2006. 8

[49] P. Cerdá-Durán, V. Quilis, and J. A. Font. AMR simulations of the low T/—W— bar-mode instability of neutron stars. *Computer Physics Communications*, 177:288–297, August 2007. 8

[50] C. D. Ott, H. Dimmelmeier, A. Marek, H.-T. Janka, I. Hawke, B. Zink, and E. Schnetter. 3D Collapse of Rotating Stellar Iron Cores in General Relativity Including Deleptonization and a Nuclear Equation of State. *Phys. Rev. Lett.*, 98(26):261101, June 2007. 8

[51] C. D. Ott, H. Dimmelmeier, A. Marek, H.-T. Janka, B. Zink, I. Hawke, and E. Schnetter. Rotating collapse of stellar iron cores in general relativity. *Classical Quantum Gravity*, 24:139, June 2007. 8

[52] S. Scheidegger, T. Fischer, S. C. Whitehouse, and M. Liebendörfer. Gravitational waves from 3D MHD core collapse simulations. *Astron. Astrophys.*, 490:231–241, October 2008. 8

[53] E. B. Abdikamalov et al. Axisymmetric General Relativistic Simulations of the Accretion-Induced Collapse of White Dwarfs. *arXiv:0910.2703*, 2009. 8

[54] Anna L. Watts, Nils Andersson, Horst Beyer, and Bernard F. Schutz. The oscillation and stability of differentially rotating spherical shells: The normal mode problem. *Mon. Not. R. Astron. Soc.*, 342:1156, 2003. 8

[55] E. Balbinski. A new shear instability in rotating, self-gravitating, perfect fluids. *Mon. Not. R. Astron. Soc.*, 216:897–908, October 1985. 8

[56] P. J. Luyten. The dynamical stability of differentially rotating, self-gravitating cylinders. *Mon. Not. R. Astron. Soc.*, 242:447–456, February 1990. 8

[57] J. C. B. Papaloizou and D. N. C. Lin. Nonaxisymmetric instabilities in thin self-gravitating rings and disks. *Astrophys. J.*, 344:645–668, September 1989. 8

[58] F. Douchin and P. Haensel. A unified equation of state of dense matter and neutron star structure. *Astron. Astrophys.*, 380:151–167, December 2001. 8

[59] S. Chandrasekhar. Solutions of Two Problems in the Theory of Gravitational Radiation. *Phys. Rev. Lett.*, 24:611–615, March 1970. 8

[60] J. L. Friedman and B. F. Schutz. Secular instability of rotating Newtonian stars. *Astrophys. J.*, 222:281–296, May 1978. 8

[61] J. E. Tohline, R. H. Durisen, and M. McCollough. The linear and nonlinear dynamic stability of rotating N = 3/2 polytropes. *Astrophys. J.*, 298:220–234, November 1985. 9

[62] R. H. Durisen, R. A. Gingold, J. E. Tohline, and A. P. Boss. Dynamic fission instabilities in rapidly rotating N = 3/2 polytropes - A comparison of results from finite-difference and smoothed particle hydrodynamics codes. *Astrop. J.*, 305:281–308, 1986. 9

[63] J. David Brown. Gravitational waves from the dynamical bar instability in a rapidly rotating star. *Phys. Rev.*, D62:084024, 2000. 9

[64] J. L. Houser, J. M. Centrella, and S. C. Smith. Gravitational radiation from nonaxisymmetric instability in a rotating star. *Phys. Rev. Lett.*, 72:1314–1317, 1994. 9

[65] Janet L. Houser and Joan M. Centrella. Gravitational radiation from rotational instabilites in compact stellar cores with stiff equations of state. *Phys. Rev.*, 54(206):7278–7297, 1996. 9

[66] Scott C. Smith, Janet L. Houser, and Joan M. Centrella. Simulations of Nonaxisymmetric Instability in a Rotating Star: A Comparison between Eulerian and Smooth Particle Hydrodynamics. *Astrop. J.*, 458:236, 1996. 9

[67] Kimberly C. B. New, Joan M. Centrella, and Joel E. Tohline. Gravitational waves from long-duration simulations of the dynamical bar instability. *Phy. Rev.*, D62:064019, 2000. 9

[68] Kimberly C. B. New and Stuart L Shapiro. Evolution of Differentially Rotating Supermassive Stars to the Onset of Bar Instability. *Astrop. J.*, 548:439–446, 2001. 9

[69] Y. T. Liu. Dynamical instability of new-born neutron stars as sources of gravitational radiation. *Phys. Rev.*, D65(12):124003, 2002. 9

[70] Brian K. Pickett, Richard H. Durisen, and Glen A. Davis. The Dynamic Stability of Rotating Protostars and Protostellar Disks. I. The Effects of the Angular Momentum Distribution. *Astrop. J.*, 458:714, 1996. 9

[71] Joel E. Tohline and Izumi Hachisu. The breakup of self-gravitating rings, tori, and thick accretion disks. *Astrop. J.*, 361:394–407, 1990. 9

[72] Shigeyuki Karino and Yoshiharu Eriguchi. Linear Stability Analysis of Differentially Rotating Polytropes: New Results for the m=2 f-Mode Dynamical Instability. *Astrop. J.*, 592(2):1119–1123, 2003. 9

[73] Masaru Shibata, Shigeyuki Karino, and Yoshiharu Eriguchi. Dynamical instability of differentially rotating stars. *Mon. Not. R. Astron. Soc.*, 334:L27–L31, 2002. 9

[74] Masaru Shibata, Shigeyuki Karino, and Yoshiharu Eriguchi. Dynamical bar-mode instability of differentially rotating stars: effects of equations of state and velocity profiles. *Mon. Not. R. Astron. Soc.*, 342:619–626, 2003. 9

[75] Masaru Shibata, Thomas W. Baumgarte, and Stuart L. Shapiro. The bar-mode instability in differentially rotating neutron stars: Simulations in full general relativity. *Astrophys. J.*, 542:453–463, 2000. 9

[76] M. Saijo, M. Shibata, T. W. Baumgarte, and S. L. Shapiro. Dynamical Bar Instability in Relativistic Rotating Stars. In J. Craig Wheeler and Hugo Martel, editors, *20th Texas Symposium on relativistic astrophysics*, volume 586 of *AIP Conf. Proc.*, page 766, 2001. 9

[77] Motoyuki Saijo, Masaru Shibata, Thomas W. Baumgarte, and Stuart L. Shapiro. Dynamical Bar Instability in Rotating Stars: Effect of General Relativity. *Astrophys. J.*, 548:919–931, 2001. 9

[78] R. Arnowitt, S. Deser, and C. W. Misner. Canonical Variables for General Relativity. *Physical Review*, 117:1595–1602, March 1960. 15

[79] Charles W. Misner, Kip S. Thorne, and John A. Wheeler. *Gravitation*. W. H. Freeman, San Francisco, 1973. 15

[80] R. D. Richtmyer and K.W. Morton. *Difference Methods for Initial Value Problems*. Interscience Publishers, New York, 1967. 16

[81] James W. York. Kinematics and dynamics of general relativity. In Larry L. Smarr, editor, *Sources of gravitational radiation*, pages 83–126. Cambridge University Press, Cambridge, UK, 1979. 17

[82] Takashi Nakamura, Ken-ichi Oohara, and Yasufumi Kojima. General relativistic collapse to black holes and gravitational waves from black holes. *Prog. Theor. Phys. Suppl.*, 90:1–218, 1987. 17, 24

[83] `http://www.cactuscode.org`. 18

[84] C. Bona, Joan Massó, E. Seidel, and J. Stela. New Formalism for Numerical Relativity. *Phys. Rev. Lett.*, 75:600–603, 1995. 18

[85] Miguel Alcubierre. The appearance of coordinate shocks in hyperbolic formulations of general relativity. *Phys. Rev. D*, 55:5981–5991, 1997. 18

[86] Miguel Alcubierre and Joan Massó. Pathologies of hyperbolic gauges in general relativity and other field theories. *Phys. Rev. D*, 57(8):R4511–R4515, 1998. 18

[87] Miguel Alcubierre, Bernd Brügmann, Denis Pollney, Edward Seidel, and Ryoji Takahashi. Black hole excision for dynamic black holes. *Phys. Rev. D*, 64:061501(R), 2001. 18

[88] Larry Smarr and James W. York. Kinematical conditions in the construction of spacetime. *Phys. Rev. D*, 17(10):2529–2552, 15 May 1978. 18

[89] J. A. Font. Numerical hydrodynamics in general relativity. *Living Rev. Relativ.*, 6:4, 2003. 21

[90] Luca Baiotti, Ian Hawke, Pedro Montero, and Luciano Rezzolla. A new three-dimensional general-relativistic hydrodynamics code. In R. Capuzzo-Dolcetta, editor, *Computational Astrophysics in Italy: Methods and Tools*, volume 1, page 210, Trieste, 2003. MSAIt. 23

[91] Luca Baiotti, Ian Hawke, Pedro J. Montero, Frank Löffler, Luciano Rezzolla, Nikolaos Stergioulas, José A. Font, and Ed Seidel. Three-dimensional relativistic simulations of rotating neutron star collapse to a Kerr black hole. *Phys. Rev. D*, 71:024035, 2005. 23

[92] Bruno Giacomazzo and Luciano Rezzolla. WhiskyMHD: a new numerical code for general relativistic magnetohydrodynamics. *Classical Quantum Gravity*, 24:S235, 2007. 23, 24, 91

[93] Bruno Giacomazzo, Luciano Rezzolla, and Luca Baiotti. Accurate evolutions of inspiralling and magnetized neutron stars: Equal-mass binaries. *Phys. Rev. D*, 83(4):044014, Feb 2011. 23, 24, 91

[94] Erik Schnetter, Scott H. Hawley, and Ian Hawke. Evolutions in 3d numerical relativity using fixed mesh refinement. 2003. 23

[95] Erik Schnetter. CARPET: A Mesh Refinement driver for CACTUS. 23

[96] Tom Goodale, Gabrielle Allen, Gerd Lanfermann, Joan Massó, Thomas Radke, Edward Seidel, and John Shalf. The Cactus framework and toolkit: Design and applications. In *Vector and Parallel Processing – VECPAR'2002, 5th International Conference, Lecture Notes in Computer Science*, Berlin, 2003. Springer. 23

[97] Frank Löffler, Joshua Faber, Eloisa Bentivegna, Tanja Bode, Peter Diener, Roland Haas, Ian Hinder, Bruno C. Mundim, Christian D. Ott, Erik Schnetter, Gabrielle Allen, Manuela Campanelli, and Pablo Laguna. The Einstein Toolkit: A Community Computational Infrastructure for Relativistic Astrophysics. *Class. Quantum Grav.*, 29(11):115001, 2012. 23

[98] Phillip Colella and Paul R. Woodward. The piecewise parabolic method (ppm) for gas-dynamical simulations. *Journal of Computational Physics*, 54(1):174–201, 1984. 23

[99] A. Harten, P. D. Lax, and B. van Leer. On upstream differencing and godunov-type schemes for hyperbolic conservation laws. *SIAM Rev.*, 25:35, 1983. 23

[100] Z. B. Etienne, V. Paschalidis, Y. T. Liu, and S. L. Shapiro. Relativistic magnetohydrodynamics in dynamical spacetimes: Improved electromagnetic gauge condition for adaptive mesh refinement grids. *Phys. Rev. D*, 85(2):024013, January 2012. 24

[101] Heinz Otto Kreiss and Joseph Oliger. *Methods for the approximate solution of time dependent problems*. GARP publication series No. 10, Geneva, 1973. 24

[102] Denis Pollney, Christian Reisswig, Luciano Rezzolla, Béla Szilágyi, Marcus Ansorg, Barret Deris, Peter Diener, Ernst Nils Dorband, Michael Koppitz, Alessandro Nagar, and Erik Schnetter. Recoil velocities from equal-mass binary black-hole mergers: a systematic investigation of spin-orbit aligned configurations. *Phys. Rev. D*, 76:124002, 2007. 24

[103] P. Mösta, C. Palenzuela, L. Rezzolla, L. Lehner, S. Yoshida, and D. Pollney. Vacuum Electromagnetic Counterparts of Binary Black-Hole Mergers. *Phys. Rev. D*, 81:064017, 2010. 24

[104] N. Stergioulas and J. L. Friedman. Comparing models of rapidly rotating relativistic stars constructed by two numerical methods. *Astrophys. J.*, 444:306, 1995. 24

[105] L. Rezzolla and O. Zanotti. *Relativistic Hydrodynamics*. Oxford University Press, Oxford UK, 2013. 24, 94

[106] H. Komatsu, Y. Eriguchi, and I. Hachisu. Rapidly rotating general relativistic stars. I – Numerical method and its application to uniformly rotating polytropes. *Mon. Not. R. Astron. Soc.*, 237:355–379, March 1989. 25

[107] J. L. Friedman and N. Stergioulas. *Relativistic Rotating Stars*. Cambridge, UK: Cambridge University Press, 2012. 25

[108] Nikolaos Stergioulas. Rotating stars in relativity. *Living Rev. Relativ.*, 1:8, 1998. 26

[109] B. Giacomazzo, L. Rezzolla, and N. Stergioulas. Collapse of differentially rotating neutron stars and cosmic censorship. *Phys. Rev. D*, 84(2):024022, July 2011. 27

[110] Motoyuki Saijo, Masaru Shibata, Thomas W. Baumgarte, and Stuart L. Shapiro. Dynamical bar instability in rotating stars: Effect of general relativity. *Astrophys. J.*, 548:919–931, 2001. 30

[111] Luca Baiotti, Ian Hawke, and Luciano Rezzolla. On the gravitational radiation from the collapse of neutron stars to rotating black holes. *Classical Quantum Gravity*, 24:S187–S206, 2007. 30, 50

[112] S. Chandrasekhar. The stability of viscous flow between rotating cylinders in the presence of a magnetic field. *Proceedings of the Royal Society of London. Series A. Mathematical and Physical Sciences*, 216(1126):293–309, 1953. 76

[113] S. Chandrasekhar. The Stability of Non-Dissipative Couette Flow in Hydromagnetics. *Proceedings of the National Academy of Science*, 46:253–257, February 1960. 76

[114] E. P. Velikhov. Stability of an ideally conducting liquid flowing between cylinders rotating in a magnetic field. *Sov. Phys. JETP*, 36:1398–1404, 1959. 76

[115] S. A. Balbus and J. F. Hawley. Instability, turbulence, and enhanced transport in accretion disks. *Reviews of Modern Physics*, 70:1–53, January 1998. 77

[116] M. Obergaulinger, P. Cerdá-Durán, E. Müller, and M. A. Aloy. Semi-global simulations of the magneto-rotational instability in core collapse supernovae. *Astron. Astrophys.*, 498:241–271, April 2009. 81

[117] A. R. Choudhuri. *The physics of fluids and plasmas : an introduction for astrophysicists /*. December 1998. 81

[118] Y. Masada, T. Sano, and K. Shibata. The Effect of Neutrino Radiation on Magnetorotational Instability in Proto-Neutron Stars. *Astrop. J.*, 655:447–457, January 2007. 82

[119] E. T. Vishniac and A. Brandenburg. An Incoherent alpha - Omega Dynamo in Accretion Disks. *Astrophys. J.*, 475:263, January 1997. 82

[120] L. Rezzolla, F. K. Lamb, and Stuart L. Shapiro. r-mode oscillations in rotating magnetic neutron stars. *Astrophys. J.*, 531:L139, 2000. 94

[121] Luca Baiotti, Bruno Giacomazzo, and Luciano Rezzolla. Accurate evolutions of inspiralling neutron-star binaries: assessment of the truncation error. *Class. Quantum Grav.*, 26:114005, 2009. 95